

NASA
**Technical
Paper**
3564

W-34

2-1-96

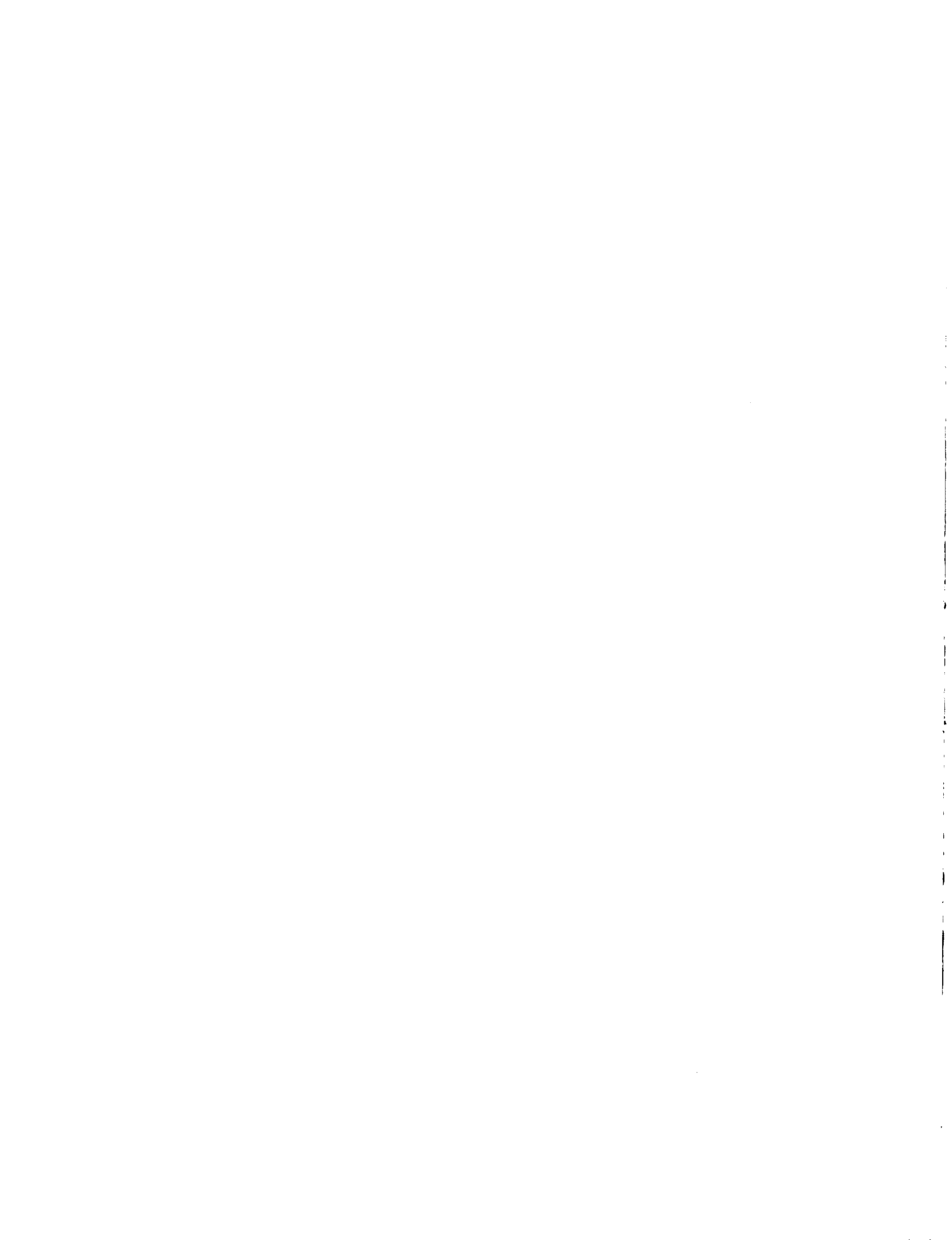
March 1996

**Tank Pressure Control Experiment:
Thermal Phenomena
in Microgravity**

Mohammad M. Hasan, Chin S. Lin,
Richard H. Knoll, and Michael D. Bentz



National Aeronautics and
Space Administration



**NASA
Technical
Paper
3564**

1996

**Tank Pressure Control Experiment:
Thermal Phenomena
in Microgravity**

Mohammad M. Hasan
*Lewis Research Center
Cleveland, Ohio*

Chin S. Lin
*Analex Corporation
Brook Park, Ohio*

Richard H. Knoll
*Lewis Research Center
Cleveland, Ohio*

Michael D. Bentz
*Boeing Defense & Space Group
Seattle, Washington*



National Aeronautics and
Space Administration
Office of Management
Scientific and Technical
Information Program

Tank Pressure Control Experiment: Thermal Phenomena in Microgravity

Mohammad M. Hasan

National Aeronautics and Space Administration

Lewis Research Center

Cleveland, Ohio 44135

Chin S. Lin

Analex Corporation

3001 Aerospace Parkway

Brook Park, Ohio 44142

Richard H. Knoll

National Aeronautics and Space Administration

Lewis Research Center

Cleveland, Ohio 44135

and

Michael D. Bentz

Boeing Defense & Space Group

Seattle, Washington 98124

Summary

The report presents the results of the flight experiment Tank Pressure Control Experiment/Thermal Phenomena (TPCE/TP) performed in the microgravity environment of the space shuttle. TPCE/TP, flown on the Space Transportation System STS-52, was a second flight of the Tank Pressure Control Experiment (TPCE). The experiment used Freon 113 at near saturation conditions. The test tank was filled with liquid to about 83 percent by volume. The experiment consisted of 21 tests. Each test generally started with a heating phase to increase the tank pressure and to develop temperature stratification in the fluid, followed by a fluid mixing phase for the tank pressure reduction and fluid temperature equilibration. The heating phase provided pool boiling data from large (relative to bubble sizes) heating surfaces (0.1046 m by 0.0742 m) at low heat fluxes (0.23 to 1.16 kW/m²). The system pressure and the bulk liquid subcooling varied from 39 to 78 kPa and 1 to 3 deg C, respectively. The boiling process during the entire heating period, as well as the jet-induced mixing process for the first 2 min of the mixing period, was also recorded on video.

The unique features of the experimental results are the sustainability of high liquid superheats for long periods and the occurrence of explosive boiling at low heat fluxes (0.86 to 1.1 kW/m²). For a heat flux of 0.97 kW/m², a wall superheat of 17.9 deg C was attained in 10 min of heating. This superheat was followed by an explosive boiling accompanied by a pressure spike of about 38 percent of the tank pressure at the inception of boiling. However, at this heat flux the vapor

blanketing the heating surface could not be sustained. Steady nucleate boiling continued after the explosive boiling. The jet-induced fluid mixing results were obtained for jet Reynolds numbers of 1900 to 8000 and Weber numbers of 0.2 to 6.5. Analyses of data from the two flight experiments (TPCE and TPCE/TP) and their comparison with the results obtained in drop tower experiments suggest that as Bond number approaches zero the flow pattern produced by an axial jet and the mixing time can be predicted by the Weber number.

Symbols

<i>a</i>	acceleration, m/s ²
Bo	Bond number
<i>D</i>	tank diameter, m
<i>D_j</i>	jet diameter at liquid-vapor interface, m
<i>D_o</i>	jet diameter at nozzle outlet, m
<i>g</i>	gravitational acceleration on Earth's surface, m/s ²
<i>h_b</i>	jet submergence (distance from nozzle outlet to interface), m
<i>P</i>	instantaneous tank pressure, Pa

P_{eq}	equilibrium pressure attained during mixing, Pa
P_i	pressure at initiation of mixing, Pa
P_{nc}	partial pressure of noncondensable gases, Pa
q_w	wall heat flux, kW/m^2
Re_j	jet Reynolds number at nozzle outlet
Ri	Richardson number
T_s	saturation temperature corresponding to tank pressure, °C
T_w	heater surface temperature, °C
T_1, T_2, T_4, T_5	fluid temperatures, °C
T_3, T_6	heater A and heater B surface temperatures, respectively, °C
T_7	liquid jet temperature, °C
ΔT_{sub}	liquid subcooling, $T_s - T_1$
ΔT_{sat}	wall superheat, $T_w - T_s$
t	time, s
t^*	dimensionless mixing time
V_o	jet velocity at nozzle outlet, m/s
We_j	jet Weber number
β	coefficient of thermal expansion
ρ	liquid density, kg/m^3
σ	surface tension, N/m

Introduction

An important issue in microgravity fluid management is controlling pressure in on-orbit storage and resupply systems for cryogenic propellants and life support fluids (i.e., liquid hydrogen, oxygen, and nitrogen). Self-pressurization occurs in closed cryogenic fluid storage tanks when heat leaks through a tank's thermal protection system. The liquid-vapor interface location and configuration are not well defined in microgravity environments; therefore, direct venting of vapor to relieve

excess pressure is precluded in microgravity by the likelihood of venting liquid along with the vapor. Labus et al. (ref. 1) adequately described technical problems associated with direct venting of vapor in microgravity conditions. Realization of these problems has led to the development of the concept of thermodynamic vent systems (refs. 2 and 3) for the pressure control of cryogenic storage tanks. However, the design and performance of a pressure control device are expected to be strongly influenced by acceleration-dependent fluid dynamics and transport phenomena, such as the thermal stratification, fluid mixing, boiling, evaporation, and direct contact condensation of vapor on the agitated liquid surface (refs. 4 to 10).

Recently, Lin and Hasan (ref. 11) analytically investigated the problem of thermal stratification and self-pressurization of a partially filled liquid hydrogen storage tank subjected to a uniform wall heat flux in a microgravity condition. They concluded that the microgravity liquid-vapor configuration may present unique thermal problems for the storage of cryogenic fluids in space environments. In microgravity the liquid-vapor interface configuration is principally determined by the surface tension force and the contact angle. It also depends on tank shape and size and liquid fill level. Usually, the contact angle and Bond number Bo characterize the interface configuration. Figure 1(a) shows an idealized liquid-vapor configuration for a wetting fluid in a spherical tank in a microgravity ($Bo < 1$) environment. The interface configuration on the ground, where $Bo >> 1$, is shown in figure 1(b) for comparison.

The idealized liquid-vapor configuration (fig. 1(a)) shows that for a partially full tank there may not be direct contact between the tank wall and the vapor region. Heat transfer will occur from the tank wall to the liquid and then to the vapor. As a consequence, the entire liquid region may be superheated. The maximum liquid superheat will occur at the tank wall. A superheated liquid represents a metastable condition and may lead to pressure spikes of varying magnitudes in a

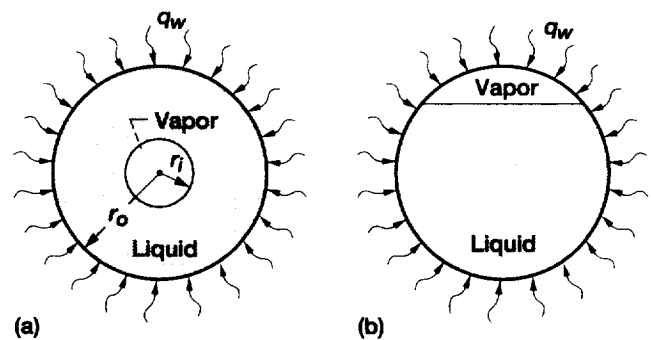


Figure 1.—Liquid-vapor configurations of wetting fluid in spherical tank. (a) Microgravity configuration, $Bo < 1$. (b) Normal-gravity configuration, $Bo >> 1$.

closed system either from boiling or flashing of superheated liquid. Lin and Hasan's (ref. 11) results show that in the absence of convective motion a high liquid superheat can be attained even at very low heat fluxes. Heat fluxes from free convection to the isolated bubble region in normal gravity are referred to as "low heat fluxes." Of course, how high a liquid superheat can be sustained cannot be predicted theoretically. Such information has to come from experiments performed in the relevant acceleration environment with the fluid and surface combination of interest.

The fact that even at very low heat fluxes a high liquid superheat can be sustained for a long duration in microgravity was first demonstrated in a flight experiment titled Tank Pressure Control Experiment (TPCE). The TPCE, designed on the basis of the experimental findings of references 5 and 7, was flown on the Space Transportation System STS-43 in August 1991. Figure 2 is a schematic of the experimental system of the TPCE. The primary objective of the TPCE was to investigate the axial, jet-induced fluid mixing process in a partially filled tank in a long-duration microgravity environment. The experiment and its results are described in detail by Bentz et al. (refs. 12 and 13).

The initial conditions, such as the tank pressure and the liquid temperature stratification for each test of the TPCE, were produced by heating surfaces immersed in nearly saturated Freon 113. The results of the heating phase of this

experiment, reported by Hasan et al. (ref. 14), constitute the first set of pool boiling data obtained in the long-duration microgravity environment of the space shuttle. The experimental data clearly demonstrated that steady nucleate pool boiling can be sustained in a long-duration microgravity environment for very low heat fluxes (0.2 to 1.1 kW/m^2). The data also showed that in microgravity a high liquid superheat can be sustained for long periods (several minutes). The superheating was usually followed by pressure spikes of considerable magnitude, suggesting that explosive boiling or flashing of superheated liquid near the heater wall may have occurred. Figure 3 (reproduced from ref. 14) shows that heater A surface temperature T_3 continued to increase for about 7.5 min with no change in tank pressure. The wall superheat reached 13 deg C and was followed by explosive boiling as evidenced by a pressure spike of about 16 kPa and an abrupt drop in heater wall temperature.

However, video observation of these events was not made during the experiment. Therefore, the flight experiment was reconfigured with the primary objective of obtaining video observation of the thermal and fluid dynamic processes during the heating phase. The second experiment, titled Tank Pressure Control Experiment/Thermal Phenomena (TPCE/TP), was performed in the space shuttle *Columbia*, STS-52. The findings of this experiment on jet-induced fluid mixing and fluid heating were partially reported in references 15 and 16. This report compiles the entire results of this flight experiment. Results presented include experimental data and video observation of the following processes:

1. Liquid superheat and pool boiling of nearly saturated Freon 113 when subjected to low heat fluxes (0.2 to 1.1 kW/m^2)

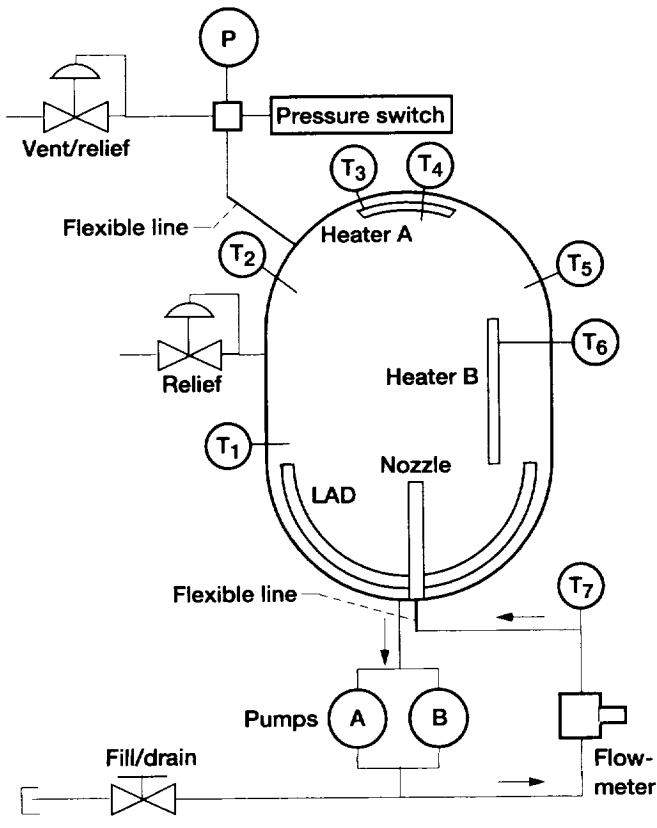


Figure 2.—Schematic of experimental system.

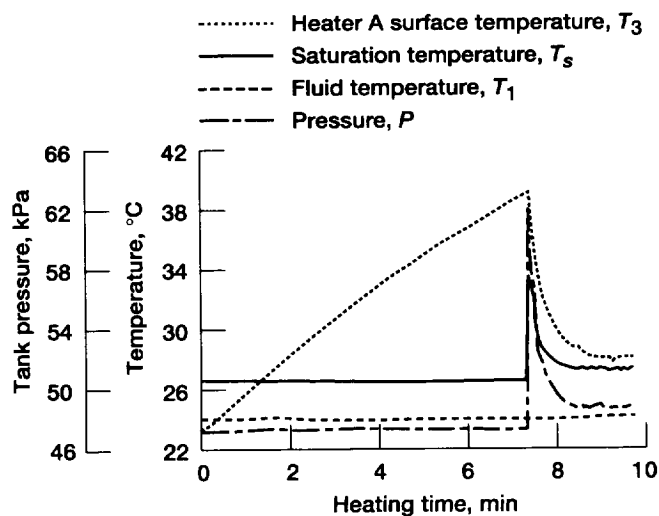


Figure 3.—Results from TPCE (ref. 14) showing pressure spike.

2. Explosive boiling and the subsequent events following this type of boiling in a closed system
3. Pressure decay during low-velocity, axial, jet-induced mixing
4. The flow pattern transition and the response of the liquid-vapor interface configuration to various jet flow rates

Experiment

Experimental System

The experimental system of the TPCE (fig. 2) was used in this experiment without any modification. It consists of a 0.254-m-diameter cylindrical tank with hemispherical domes. The tank volume is 0.0137 m³. The tank geometry and dimensions are shown in figure 4. Bentz (ref. 13) provided the rationale for selecting the tank geometry and dimensions. The tank is filled with Freon 113 to about 83 percent by volume. A jet nozzle is positioned along the tank's major axis near one end of the tank to provide fluid mixing. The jet nozzle is a straight tube with a 0.01-m (0.40-in.) inside diameter. Two pumps located outside the tank are supplied with vapor-free liquid by a liquid acquisition device (LAD). Figure 5 shows the Plexiglass test tank with the heaters, a thermistor, the LAD, and the pumps installed. Two heaters, designated as heater A and heater B, are immersed in the fluid. Heater A is located within 0.005 m of the end of the tank wall opposite the jet nozzle. Heater B is off the tank major axis and approximately 0.025 m away from the tank wall.

Figure 6(a) shows the heater configuration and some details of its assembly. The two heaters are constructed of an etched-foil element encased in silicon rubber insulation and sandwiched between two 304L stainless steel plates. The outside dimensions of the heater assembly are 0.1046 m by

0.0742 m. The total surface area (both sides of the heater) is 0.0155 m². Both heaters are the same size, except that heater A is bent to a 0.121-m radius to follow the curvature of the tank wall. The heater assembly is welded to a standoff tube that supports the assembly and contains the electrical leads. The total mass of each heater, excluding the standoff tube and thermistor, is 0.214 kg, and the thermal capacitance is estimated to be 0.10 kJ/deg C. Power is supplied to the heater by a battery pack consisting of 96 F-size alkaline cells.

The primary measurements during a test include tank pressure, heater power, heater surface temperature, liquid temperatures at various locations, and jet flow rate as functions of time. The temperature probes shown in figure 2 are thermistors encapsulated in stainless steel sheaths. Thermistors T₃ and T₆ measure the surface temperature of heaters A and B, respectively. Other thermistors measure liquid temperature at various locations in the tank. The tip of thermistor T₁ is 0.013 m from the tank wall, and thermistors T₂, T₄, and T₅ reach 0.025 m from the wall. Thermistor T₄ extends through a hole in heater A without touching the heater plate. Thermistor T₇ is located inside the fluid line upstream of the nozzle. The tank pressure transducer is attached to a manifold that also connects a pressure switch and one of the two relief valves to the tank. The flowmeter is located in a common line downstream of the pump.

Three accelerometers are installed on the tank supports such that their axes are aligned with the STS orbiter coordinates. Figure 7 shows the acceleration axes with respect to the fluid tank, to the orbiter, and to the picture visible when viewing the videotapes. Video observations are recorded by two modified 8-mm camcorders. The apparatus and the instrumentation were described in detail by Bentz (ref. 13). The range, resolution, and accuracy of each instrument and the rate at which data are taken during each stage of a test run are listed in table I.

Test Matrix

Twenty-one tests, consisting of various combinations of jet flow rates and heaters, were performed. Each test is designated as a "run number." The test matrix is shown in table II. The heater used and heating time, the camera used (right or left), video "on" time, jet flow rate, mixing time, and settling time for each test run are listed in the table. Video observation was available only for the first 16 runs.

Runs 1, 5, 9, and 14 were designed to observe the response of the liquid-vapor interface when subjected to forced flow. For these tests the heaters were not used and the liquid motion was caused solely by the jet flow. It was planned to increase the jet flow rate in steps of 0.19 liter/min every 30 s beginning at zero flow and ending at 1.9 liters/min in 6.00 min. The last step had a duration of 60 s. The video was then left on for an additional 6 min after the pumps were turned off to record the time required to reestablish a quiescent stable interface.

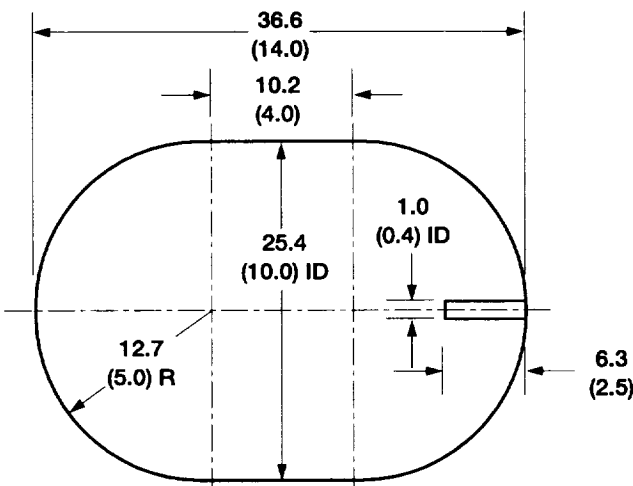


Figure 4.—Test tank dimensions. (Dimensions are in centimeters (inches).)

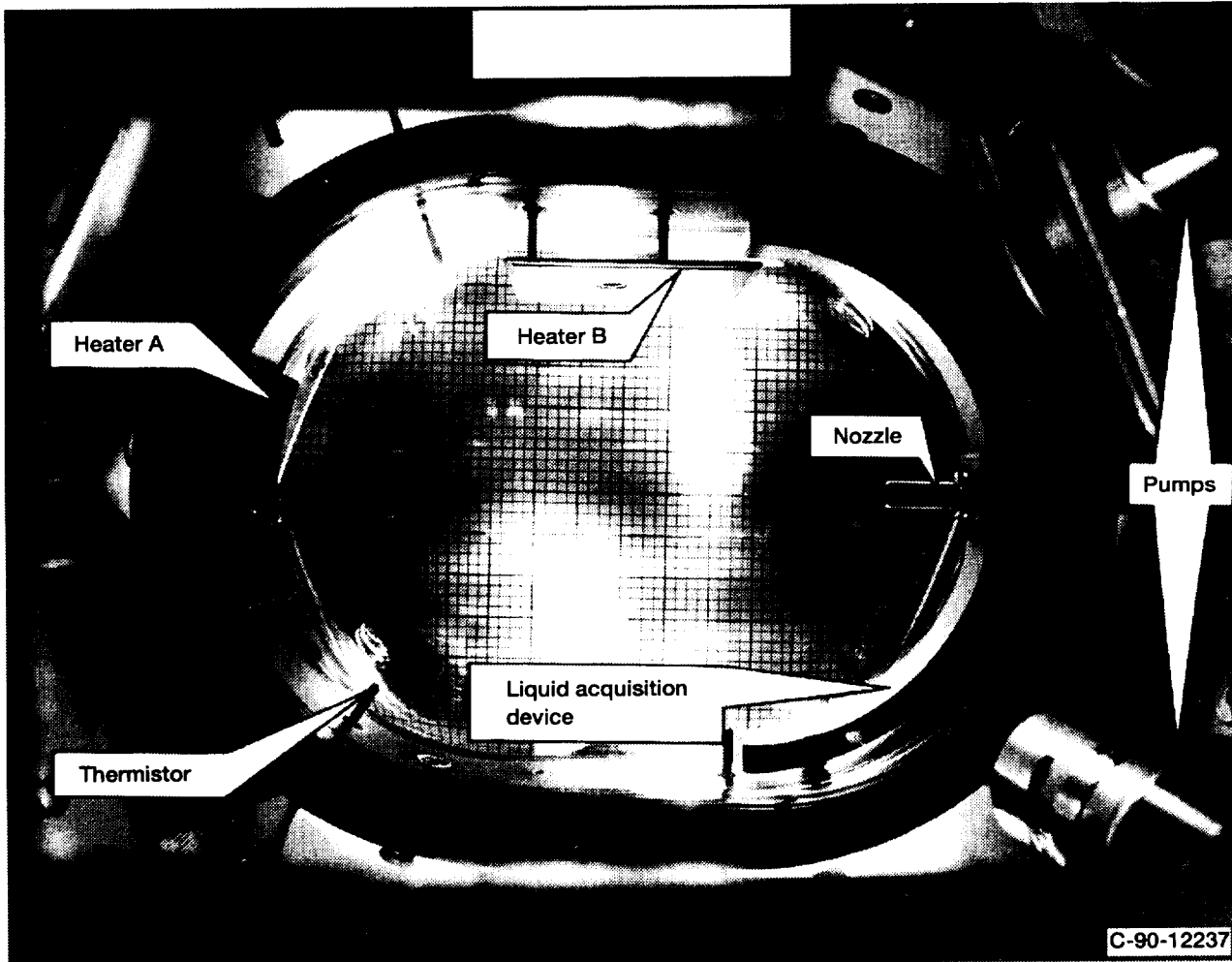


Figure 5.—Plexiglass test tank showing heaters and other accessories.

For the other test runs the initial condition of each test was established by heating the fluid with either heater A, heater B, or both heaters. The heating phase for each of the first 16 tests lasted either 10 or 18 min. Video observation of the entire heating period was recorded. After the heating phase the mixer was turned on at a specified flow rate to begin the fluid mixing test. The heating rate for each test was constant but varied from 7.2 to 18.0 W during the test matrix. The heat flux corresponding to these heating rates ranged from 0.23 to 1.16 kW/m². The fluid mixing continued for 10 min, but the video observation was recorded only for the first 2 min of mixing. The fluid was then allowed to settle for 20 min before beginning the next test. Runs 17 to 21 were performed in the absence of video recording. The heating duration for each of these tests was increased to 40 min.

Timeline for Typical Test

A timeline for a typical test is shown in figure 8. At time zero all digital data recording began and the camera power

was turned on (no lamps). Between 0 and 12 s the camera began recording and recorded a binary code flashed by the light-emitting diodes (LED's) describing the test sequence number. At 12 s the lamps were turned on along with a once-per-second flashing of LED for a timing mark identification on the video. At 13 s heater power was turned on. The heater then remained on for its preprogrammed test time. At the end of the heating stage the lamps blinked to indicate the beginning of the mixing stage. The fluid mixing continued for its specified period and then was terminated to allow the fluid to settle. The lamps and camera remained on through the first 2 min of mixing for each of the first 16 test runs with the exception of runs 1, 5, 9, and 14.

Flight Operation

The experiment operated for 16.4 hr in flight, following activation by a baroswitch, after a 6-hr initial delay to avoid disturbances early in the mission. The overall acceleration environment encountered during the 21-run test matrix is

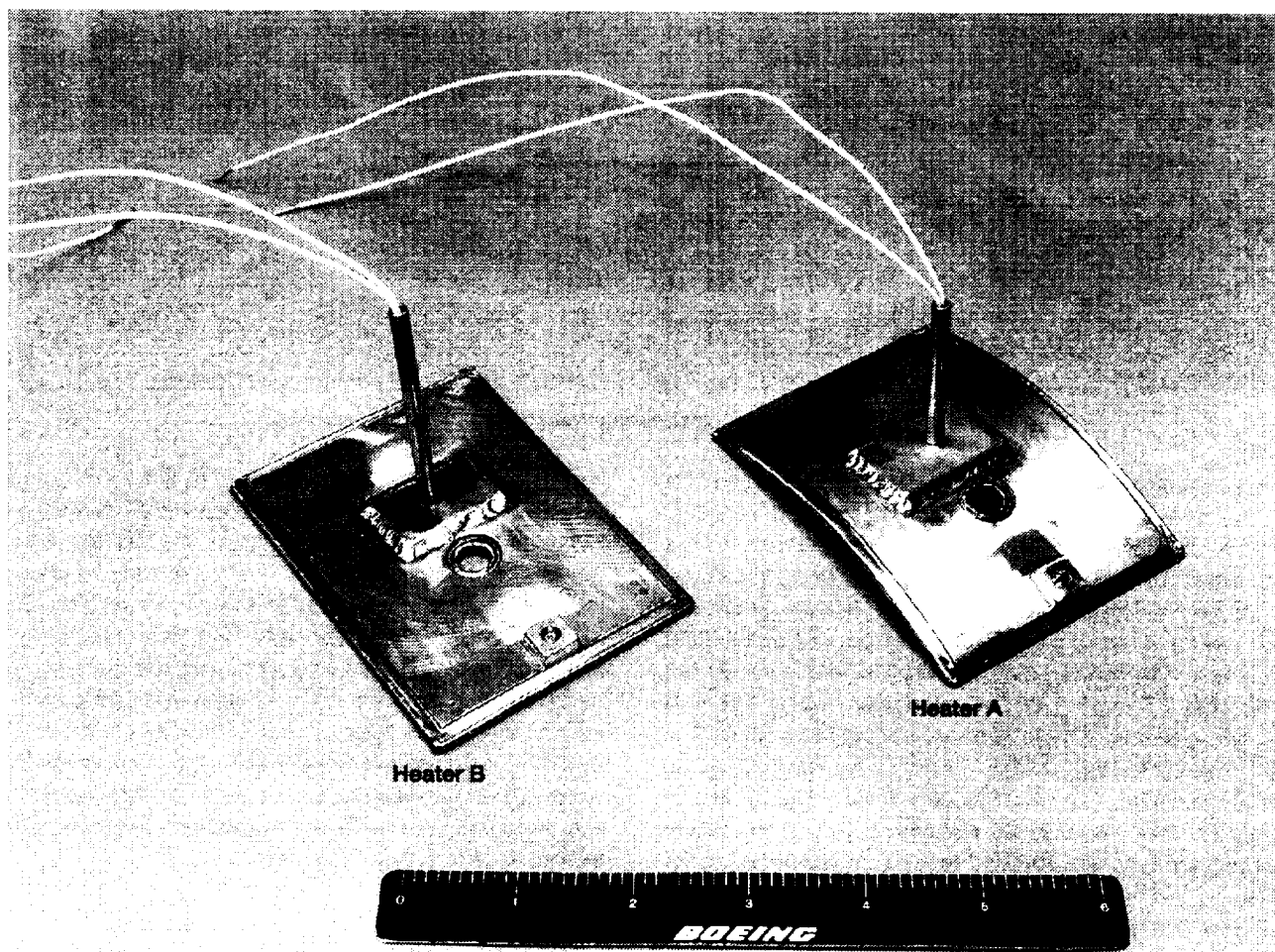
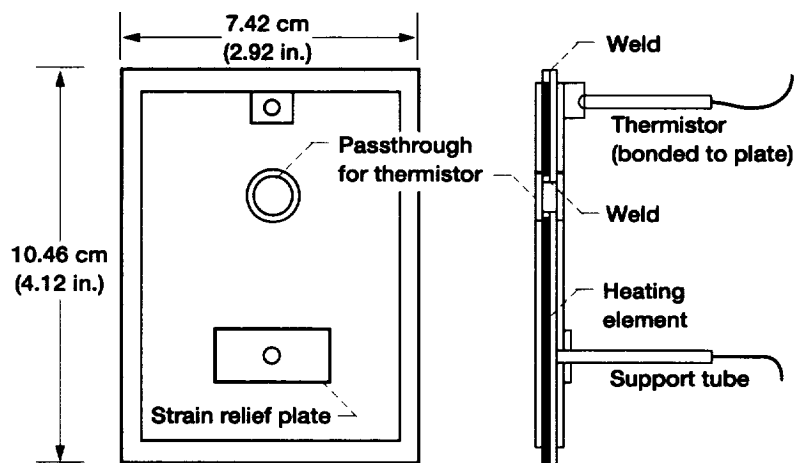


Figure 6.—Heaters A and B and heater configuration and assembly.

C-90-02682

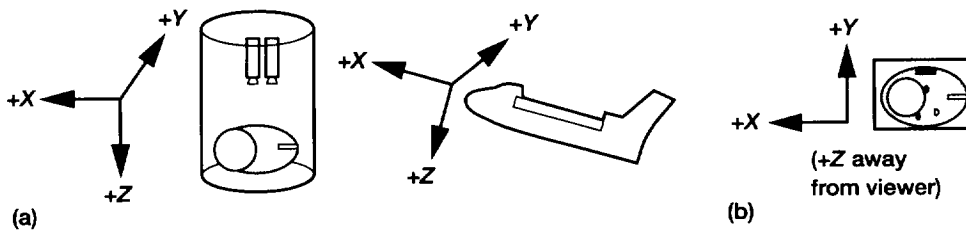


Figure 7.—Accelerometer axes. (a) TPCE coordinates. (b) Relative to video image.

TABLE I.—INSTRUMENTATION

Instrument	Range	Resolution	Accuracy	Sample rate		
				Heating stage	Mixing stage	Settling stage
Pressure transducer (absolute)	0 to 173 kPa (0 to 25 psia)	0.04 kPa (0.006 psi)	0.35 kPa (0.05 psia)	3/s	3/s	1/s
Thermistors (7)	-20 to 70 °C (-4 to 158 °F)	0.02 deg C (0.036 deg F)	0.1 deg C (0.18 deg F)	1/s	1/s	1/min
Flowmeter	0 to 3.8 liters/min (0 to 1.0 gal/min)	0.02 liter/min (0.005 gal/min)	0.04 liter/min (0.01 gal/min)	--	1/s	--
Heater power	0 to 30 W	0.1 W	0.1 W	1/s	--	--
Accelerometers (3)	±0.01 g	2.4×10 ⁻⁶ g's	5×10 ⁻⁴ g's abs (1.2×10 ⁻⁵ g's rel)	3/s	3/s	3/s

shown in figure 9, where the average acceleration values (averaged over 1-min intervals) are plotted versus time. The average accelerometer readings presented in this report do not indicate the background acceleration level but represent residual instrument bias error. Bentz (ref. 13) discussed how the accelerometer readings may be used to provide an indication of the background acceleration level. It is estimated that during the course of this experiment the steady-state component of the background acceleration was 10^{-6} to 10^{-7} g's. Disturbances caused by crew, thrusters, etc., were much higher, up to 10^{-2} g's. Figure 9 also shows that the tail-to-wind orientation of STS-52 began at 57.3 min in the later stages of run 2 and ended at 763.7 min in the later stages of run 18. During this "tail-first" orbiter attitude the liquid tended to settle at the nozzle end of the tank, with the ullage bubble tending to be symmetric opposite the nozzle. An astronaut sleep period scheduled between 174.5 and 654.5 min provided an especially quiescent acceleration environment for runs 6 to 16.

Data Presentation

Experimental results of all 21 test runs are presented in the appendix of this report. Examples of typical data plotted for

each test run are given in figures 10 to 12. The data shown are for run 2. Figure 10 gives pressure, heater power, and jet flow rate as a function of time. For run 2 the experiment began at 26.23 min or 0:26:14 clock time. Heater power was applied at 0:26:27 and mixing began at 0:36:16. Table III gives the timing of all key events for each test run. Figures 11 and 12 show the heater and fluid temperatures and the acceleration environment, respectively, throughout run 2.

Video Data

More than 4 hr of video were obtained for the first 16 test runs. Much of the data returned by this experiment can be best seen in the videotapes. The video supplement of this document consists of two 2-hr tapes and is available through the NASA Center for Aerospace Information (see back cover of the report). Figure 13 gives an example of the video images acquired during the flight experiment from the left and right cameras. It also shows the coordinate system corresponding to accelerometer data. Test time in hours, minutes, and seconds is designated in the lower right corner of all video data. Table IV summarizes key video events for the test runs recorded by each camera. Tables III and IV are provided to aid readers in coordinating the data plots with the video imagery.

TABLE II.—TEST MATRIX
[Numbers in parentheses show actual values obtained during experiment.]

Run	Heater	Heating time, min	Camera	Video time, min	Jet flow rate, liter/min	Mixing time, min	Settling time, min
1	Off	0.0	Right	12.0	0 to 1.893 (1.70)	6	20
2	B	10.0	Right	12.0	0.379 (0.435)	10	20
3	B	10.0	Right	12.0	0.757 (0.835)	10	20
4	B	10.0	Right	12.0	1.136 (1.220)	10	20
5	Off	0.0	Left	12.0	0 to 1.893 (1.71)	6	20
6	A	10.0	Left	12.0	0.379 (0.454)	10	20
7	A	10.0	Left	12.0	0.757 (0.821)	10	20
8	A	10.0	Left	12.0	1.136 (1.283)	10	20
9	Off	0.0	Right	12.0	0 to 1.893 (1.75)	6	20
10	B	18.0	Right	20.0	0.757 (0.875)	10	20
11	B	18.0	Right	20.0	0 (0)	10	20
12	A	18.0	Left	20.0	1.136 (1.278)	10	20
13	A	18.0	Left	20.0	0.379 (0.517)	10	20
14	Off	0.0	Left	12.0	0 to 1.893 (1.80)	6	20
15	A&B	18.0	Right	20.0	1.514 (1.595)	10	20
16	A&B	18.0	Left	20.0	1.514 (1.643)	10	20
17	A	40.0 (20.0)	Off	---	1.514 (1.619)	30	20
18	B	40.0 (20.0)	Off	---	1.514 (1.661)	30	20
19	A&B	40.0	Off	---	1.514 (1.701)	10	20
20	B	40.0	Off	---	0.757 (0.862)	10	20
21	A	40.0	Off	---	1.136 (1.342)	10	20

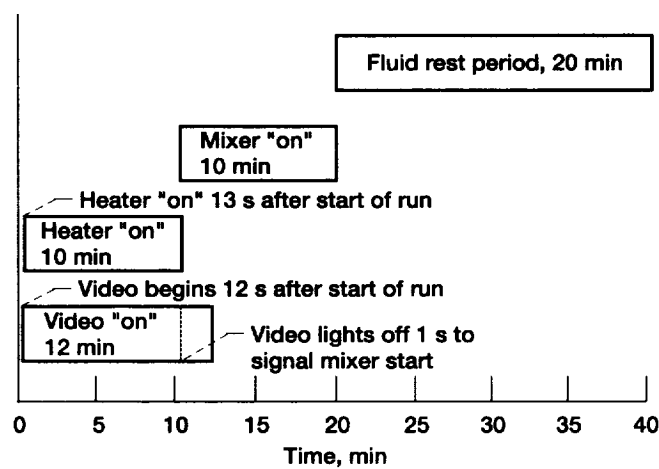


Figure 8.—Typical timeline for test run (runs 2 to 4 and 6 to 8).

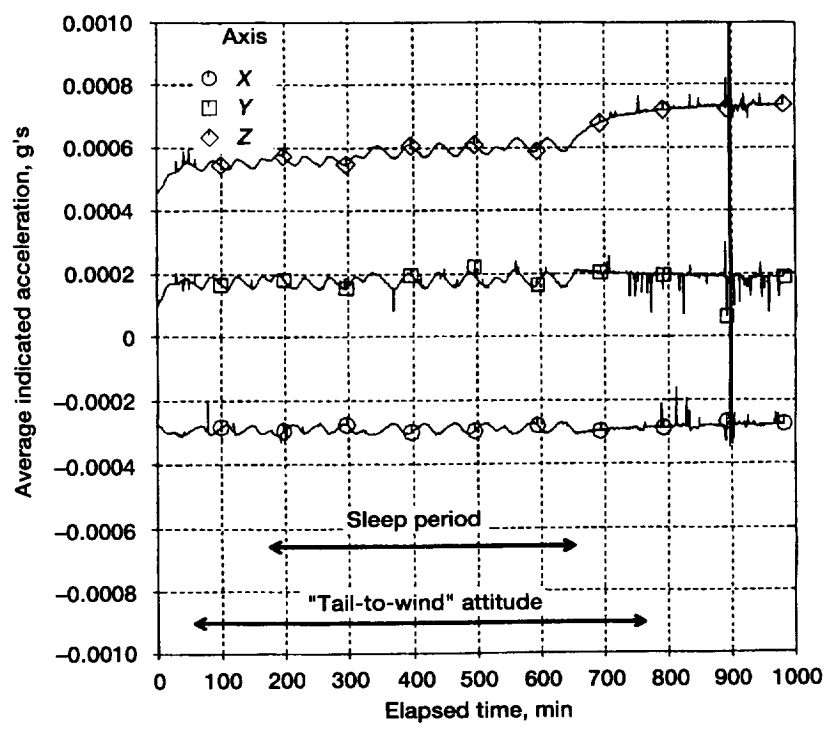


Figure 9.—Average indicated acceleration as function of time.

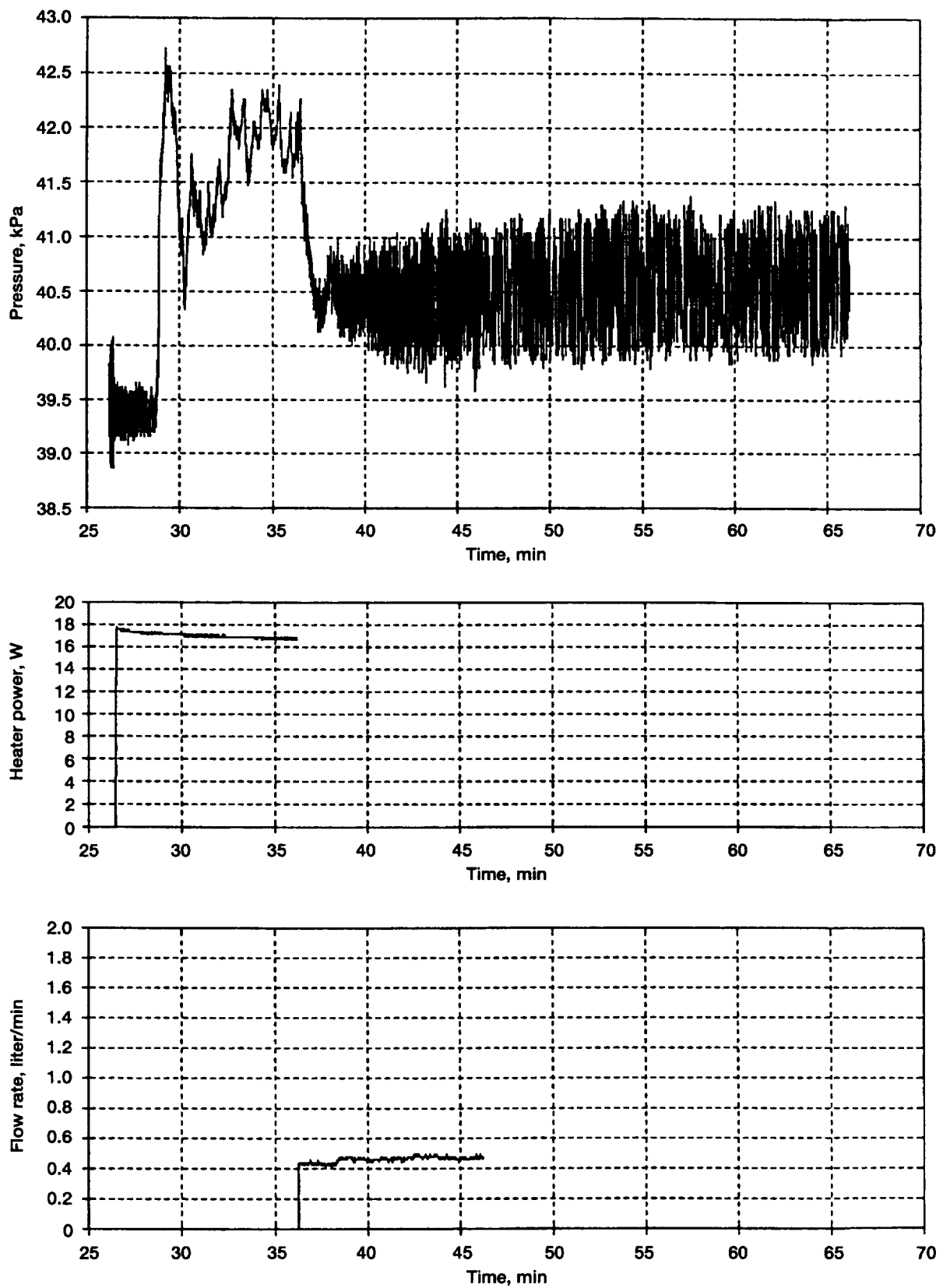


Figure 10.—Tank pressure, heater power, and mixer flow rate histories (run 2).

TABLE III.—TIMING OF KEY EVENTS

Run	Start of run	Start, min	Lights on/ video on	Heater on	Heater off	Mixer on	Lights off/ video off	Mixer off	End of run
1	0:00:00	0	0:00:14	-----	-----	0:00:45	0:12:00	0:06:14	0:26:14
2	0:26:14	26.23	0:26:26	0:26:27	0:36:15	0:36:16	0:38:14	0:46:15	1:06:15
3	1:06:15	66.25	1:06:27	1:06:28	1:16:15	1:16:16	1:18:15	1:26:15	1:46:15
4	1:46:15	106.25	1:46:27	1:46:28	1:56:15	1:56:16	1:58:15	2:06:15	2:26:15
5	2:26:15	146.25	2:26:29	-----	-----	2:27:00	2:38:15	2:32:29	2:52:29
6	2:52:29	172.48	2:52:41	2:52:42	3:02:30	3:02:31	3:04:30	3:12:30	3:32:30
7	3:32:30	212.50	3:32:42	3:32:43	3:42:30	3:42:31	3:44:31	3:52:30	4:12:30
8	4:12:30	252.50	4:12:42	4:12:43	4:22:30	4:22:31	4:24:30	4:32:30	4:52:30
9	4:52:30	292.50	4:52:44	-----	-----	4:53:15	5:04:27	4:58:44	5:18:44
10	5:18:44	318.73	5:18:56	5:18:57	5:36:45	5:36:46	5:38:43	5:46:45	6:06:45
11	6:06:45	366.75	6:06:57	6:06:58	6:24:45	-----	-----	-----	6:54:45
12	6:54:45	414.75	6:54:57	6:54:58	7:12:45	7:12:46	7:14:45	7:22:45	7:42:45
13	7:42:45	462.75	7:42:57	7:42:58	8:00:46	8:00:47	8:02:45	8:10:46	8:30:46
14	8:30:46	510.77	8:31:00	-----	-----	8:31:31	8:42:46	8:37:00	8:57:00
15	8:57:00	537.00	8:57:12	8:57:13	9:15:00	9:15:01	9:17:00	9:25:00	9:45:00
16	9:45:00	585.00	9:45:12	9:45:13	10:03:00	10:03:01	10:05:01	10:13:00	10:33:00
17	10:33:00	633.00	10:33:12	10:33:13	11:13:01	10:53:02	(a)	11:23:01	11:43:01
18	11:43:01	703.02	(a)	11:43:14	12:23:01	12:03:02	(a)	12:33:01	12:53:01
19	12:53:01	773.02	(a)	12:53:14	13:33:02	13:33:03	(a)	13:43:02	14:03:02
20	14:03:02	843.03	(a)	14:03:15	14:43:02	14:43:03	(a)	14:53:02	15:13:02
21	15:13:02	913.03	(a)	15:13:15	15:53:02	15:53:03	(a)	16:03:02	16:22:56

^aCamera lights remained on throughout duration of runs 17, 18, 19, 20, and 21.

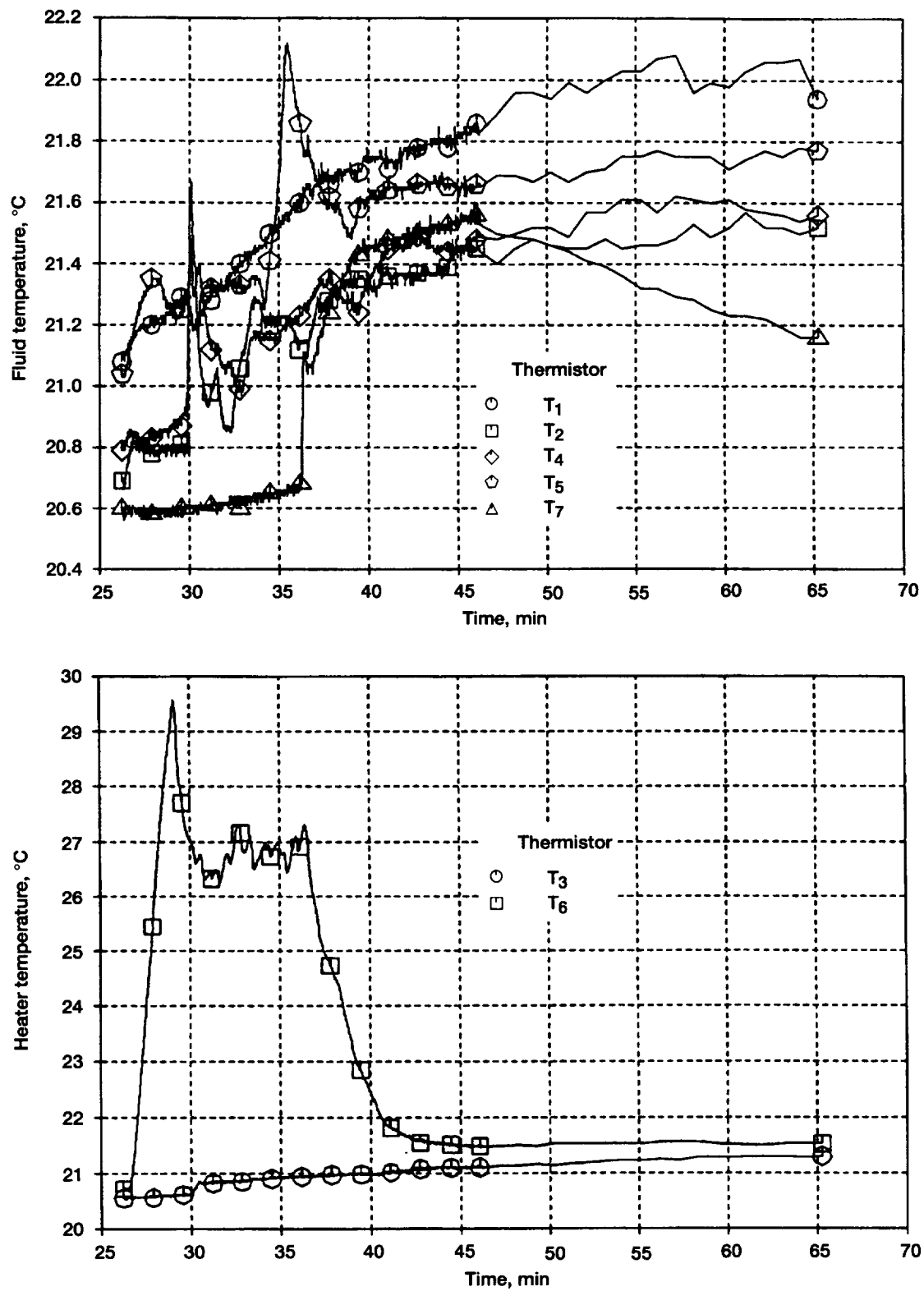


Figure 11.—Fluid and heater temperature histories (run 2).

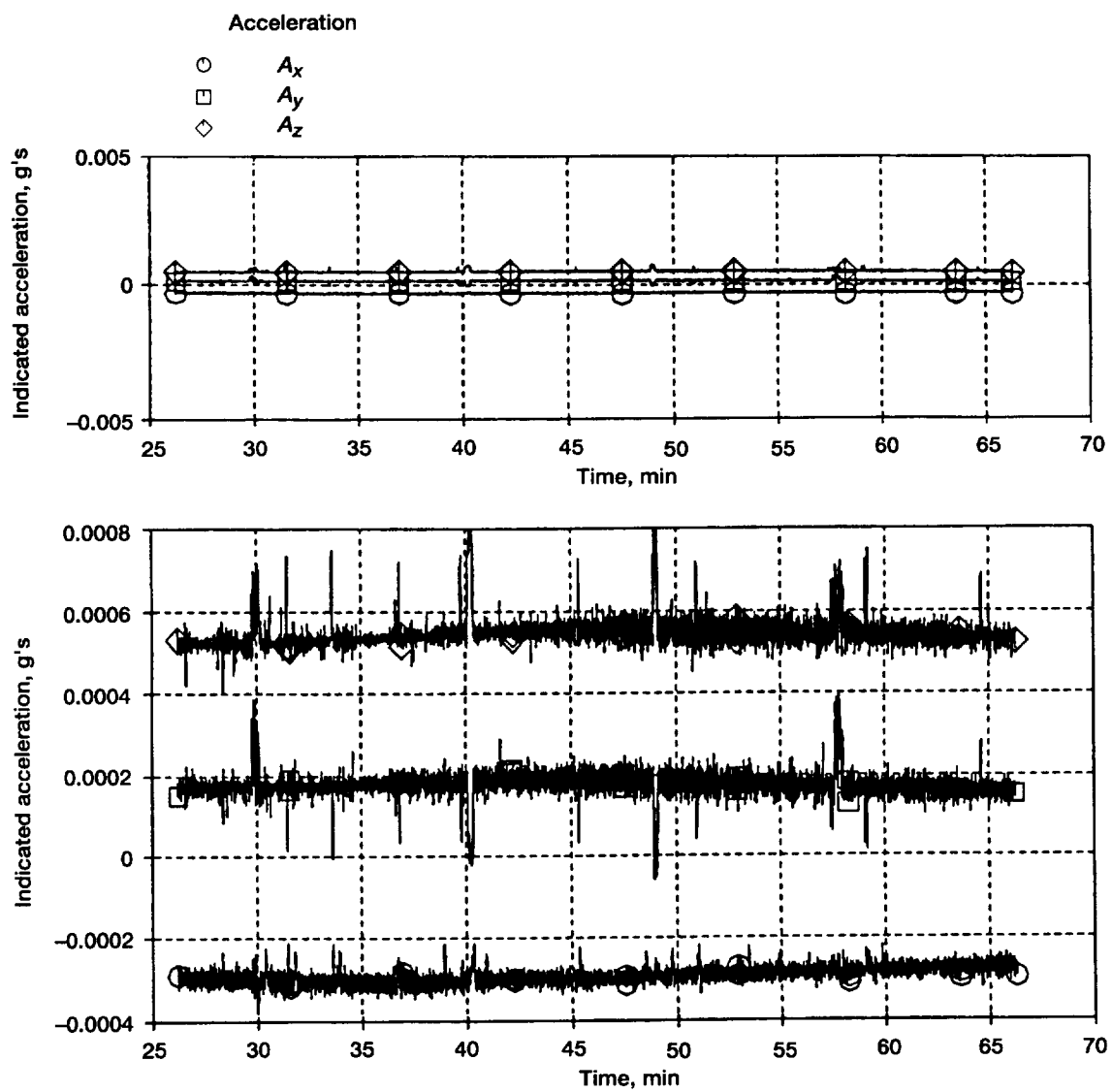


Figure 12.—Indicated acceleration data (run 2). (Lower graph shows expanded scale.)

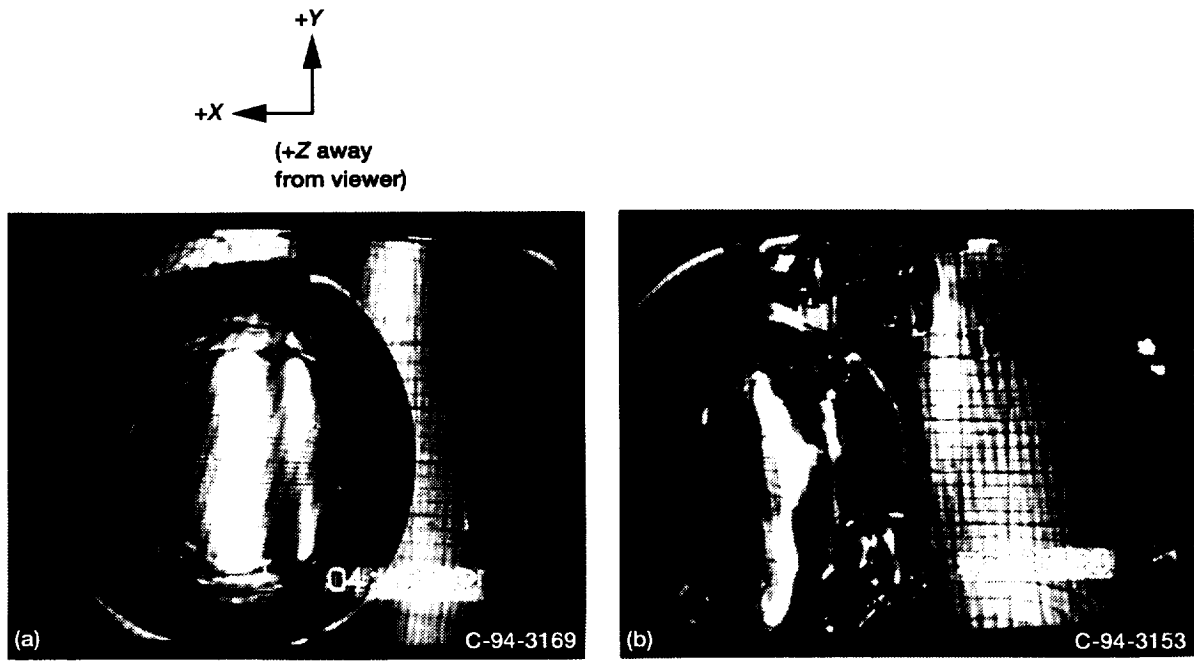


Figure 13.—Views from left and right cameras and acceleration axes with respect to picture when viewing videotapes. (a) Left camera. (b) Right camera.

TABLE IV.—VIDEO SUMMARY OF POOL BOILING AND FLUID MIXING IN LOW GRAVITY (SILENT) 2/9/93 (TOTAL RUN TIME, 1:59:54)

(a) E-9724-V 1A and 1B. Tape 1 of 2; right-side camera; runs 1 to 4, 9 to 11, and 15.

Run	Heater	Flow, liter/min	Video on	Heater on	Heater off	Mixer on	Video off
1	----	0 to 1.7	0:00:14	-----	-----	0:00:45	0:12:00
2	B	.435	0:26:26	0:26:27	0:36:15	0:36:16	0:38:14
3	B	.835	1:06:27	1:06:28	1:16:15	1:16:16	1:18:15
4	B	1.22	1:46:27	1:46:28	1:56:15	1:56:16	1:58:15
9	----	0 to 1.75	4:52:44	-----	-----	4:53:15	5:04:29
10	B	.875	5:18:56	5:18:57	5:36:45	5:36:46	5:38:43
11	B	0	6:06:57	6:06:58	6:24:45	-----	6:26:46
15	A and B	1.595	8:57:12	8:57:13	9:15:00	9:15:01	9:17:00

(b) E-9724-V 2A and 2B. Tape 2 of 2; left-side camera; runs 5 to 8, 12 to 14, and 16.

5	---	0 to 1.71	2:26:29	-----	-----	2:27:00	2:38:15
6	A	.454	2:52:41	2:52:42	3:02:30	3:02:31	3:04:30
7	A	.821	3:32:42	3:32:43	3:42:30	3:42:31	3:44:31
8	A	1.28	4:12:42	4:12:43	4:22:30	4:22:31	4:24:30
12	A	1.28	6:54:57	6:54:58	7:12:45	7:12:46	7:14:45
13	A	.517	7:42:57	7:42:58	8:00:46	8:00:47	8:02:45
14	----	0 to 1.80	8:31:00	-----	-----	8:31:31	8:42:46
16	A and B	1.64	9:45:12	9:45:13	10:03:00	10:03:01	10:05:01

Results and Discussion

The experiment was performed under steady-state thermal conditions. At the start of the heating period the maximum temperature stratification in the liquid was less than 1 deg C. Thermistor T₁ measured the liquid temperature farthest from either heater A or heater B. Therefore, the temperature measured by thermistor T₁, was taken as the bulk liquid temperature. At the start of the heating phase the bulk liquid temperature was generally within 1 deg C of the saturation temperature at the tank pressure. Figure 14, a still photograph taken from the flight videotape, shows an actual liquid-vapor configuration during a typical test run. The tank wall is entirely wetted by the liquid. The nearly spherical vapor bubble (also referred to as "an ullage bubble") surrounded by liquid represents 17-percent vapor volume. The location of the ullage bubble could not be controlled during a test. However, for most of the test runs during tail-first orbiter attitude the ullage bubble remained quiescent and located near heater A.

The following subsections discuss the experimental results of the heating phase of a test run and then the results of the mixing phase. Finally, the results of runs 1, 5, 9, and 14 (performed in the absence of heating) are presented.

Heating Phase

The heating phase for a test run varied from 10 to 40 min. The heating phase for each test run is listed in table II. The heater power was nearly constant during each test. The maximum variation of the heater power during the heating phase of a test was less than 5 percent. The initial tank pressure (i.e., the pressure at the start of heating) during these test runs

ranged from 39.6 to 68.5 kPa. With the exception of runs 11 and 20 the tank pressure up to the point of boiling inception changed only slightly (to within 1 kPa). The results of runs 11 and 20, which show some interesting features, are discussed later in this report.

Experimental data show that the boiling delay time and the incipient boiling wall superheat were affected by the location and movement of the ullage bubble. The elapsed heating time before boiling inception is defined as the boiling delay time. The incipient boiling wall superheat ($T_w - T_s$) is defined as the difference between the heater surface temperature and the saturation temperature corresponding to the tank pressure at the instant of boiling inception. The heater surface temperatures T_w of heaters A and B were measured by thermistors T₃ and T₆, respectively. The spatial variation of the heater surface temperature was not measured.

The boiling delay time and the incipient boiling wall superheat along with other pertinent variables for all test runs with heaters A and B are listed in tables V(a) and (b), respectively. With the exception of runs 7, 8, 12, and 13 the location of the ullage bubble during a test varied significantly between the start of heating and the inception of boiling. Therefore, the location of the ullage bubble during a test is not listed in table V. The video observations show that for runs 2, 3, 4, and 10 the ullage bubble was about 0.04 m away from heater B when the heater was turned on. As heating continued, the ullage bubble moved toward heater B, and boiling started after the ullage bubble touched the heater surface. Figures 15(a) to (e) are still photographs taken from the flight videotape for run 10. The sequence of the photographs shows the location and movement of the ullage bubble and the boiling process on heater B. At the start of heating (fig. 15(a)) the ullage bubble was located approximately 0.04 m away from heater B. After 2 min and 14 s of heating (fig. 15(b)) the ullage bubble had moved to within 0.01 m of heater B. After 2 min and 28 s of heating (fig. 15(c)) the ullage bubble had touched the heater surface. Boiling began after 2 min and 40 s of heating (fig. 15(d)). After 17 min and 24 s of heating (fig. 15(e)) the nucleate boiling process was continuing. Clearly shown are the growth and departure of bubbles from the heater surface and the distortion of the nearly spherical ullage bubble due to liquid motion generated by the bubbles departing from the heater surface. For runs 2, 4, and 10 the boiling delay time varied between 2.15 and 2.45 min. The incipient boiling wall superheat for these test runs varied from 6.0 to 6.6 deg C. For runs 7, 8, and 12 the ullage bubble was located about 0.02 m away from the heater, and it did not touch the heater surface before boiling inception. The ullage bubble was the farthest from the heater for run 13, and it resulted in the highest value of incipient boiling wall superheat.

High liquid superheat and explosive boiling.—The most significant finding of this experiment was that in a process of very slow heating a high liquid superheat can be sustained for a long time under a microgravity condition. In a closed

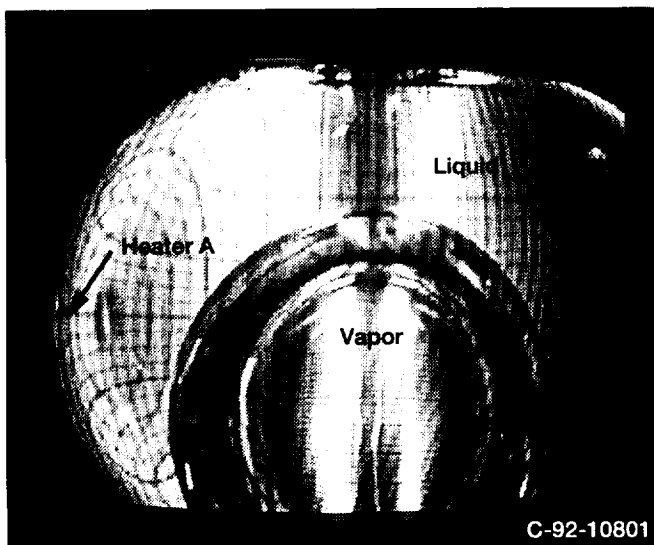


Figure 14.—Actual liquid-vapor configuration during flight experiment.

TABLE V.—BOILING DELAY TIME AND INCIPIENT BOILING
WALL SUPERHEAT
[t_0 (min), heater is turned on; t_1 (min), boiling begins; t_2 (min), tank pressure reaches peak value.]

Run		Fluid temperature, T_1	Saturation temperature, T_s	Heater surface temperature, T_w	$T_w - T_s$	Tank pressure, P , Pa	Wall heat flux, q_w , kW/m ²
6	$t_0 = 0$	23.7	24.4	22.7	---	43.5	1.07
	$t_1 = 2.73$	23.8	24.8	30.1	5.3	44.1	
	$t_2 = 2.82$	23.9	26.3	30.0	---	46.9	
7	$t_0 = 0$	24.2	24.9	23.6	---	44.3	1.04
	$t_1 = 6.21$	24.4	26.2	37.3	11.1	46.7	
	$t_2 = 6.25$	24.5	31.9	36.8	---	58.2	
8	$t_0 = 0$	24.5	25.2	24.0	---	43.0	1.03
	$t_1 = 6.47$	24.8	27.7	38.3	10.6	49.6	
	$t_2 = 6.51$	24.9	33.3	38.2	---	61.4	
12	$t_0 = 0$	26.9	27.8	25.8	---	49.6	0.98
	$t_1 = 8.76$	27.2	30.3	41.2	10.9	54.8	
	$t_2 = 8.79$	27.3	35.8	41.2	---	67.4	
13	$t_0 = 0$	27.7	28.2	26.7	---	50.3	0.97
	$t_1 = 9.77$	27.7	28.3	46.2	17.9	50.7	
	$t_2 = 9.79$	27.7	36.9	46.0	---	70.0	
17	$t_0 = 0$	28.8	29.4	27.9	---	52.9	0.95
	$t_1 = 10.01$	29.1	31.3	43.9	12.6	56.9	
	$t_2 = 10.06$	29.2	37.9	43.7	---	72.7	
21	$t_0 = 0$	36.1	36.3	34.5	---	68.4	0.89
	$t_1 = 2.22$	36.2	36.3	39.1	2.8	68.5	
	$t_2 = 2.38$	36.2	37.1	39.1	---	70.6	

TABLE V.—Concluded.

(b) Heater B						
Run	Fluid temperature, T_1	Saturation temperature, T_s	Heater surface temperature, T_w	$T_w - T_s$	Tank pressure, P , Pa	Wall heat flux, q_w , kW/m ²
2	$t_0 = 0$	21.1	22.1	20.7	---	39.6
	$t_1 = 2.40$	21.5	22.4	29.0	6.6	40.1
	$t_2 = 2.75$	21.3	24.0	29.1	---	42.7
3	$t_0 = 0$	22.0	22.6	21.5	---	40.4
	$t_1 = 3.32$	22.2	22.7	32.3	9.6	40.6
	$t_2 = 3.73$	22.2	26.3	32.7	---	46.9
4	$t_0 = 0$	22.9	23.5	22.3	---	41.9
	$t_1 = 2.15$	22.9	23.6	29.6	6.0	42.1
	$t_2 = 3.17$	23.0	25.8	31.3	---	46.1
10	$t_0 = 0$	25.5	25.9	24.6	---	46.1
	$t_1 = 2.45$	25.4	25.9	32.2	6.3	46.0
	$t_2 = 4.77$	25.4	28.8	33.7	---	51.7
11	$t_0 = 0$	26.2	26.7	25.6	---	47.7
	---	---	---	---	---	---
	---	---	---	---	---	---
18	$t_0 = 0$	31.2	30.8	29.8	---	55.7
	$t_1 = 7.07$	31.4	31.2	47.5	16.3	56.8
	$t_2 = 7.13$	31.4	38.4	47.2	---	73.8
20	$t_0 = 0$	34.4	34.2	33.3	---	63.4
	---	---	---	---	---	---
	---	---	---	---	---	---

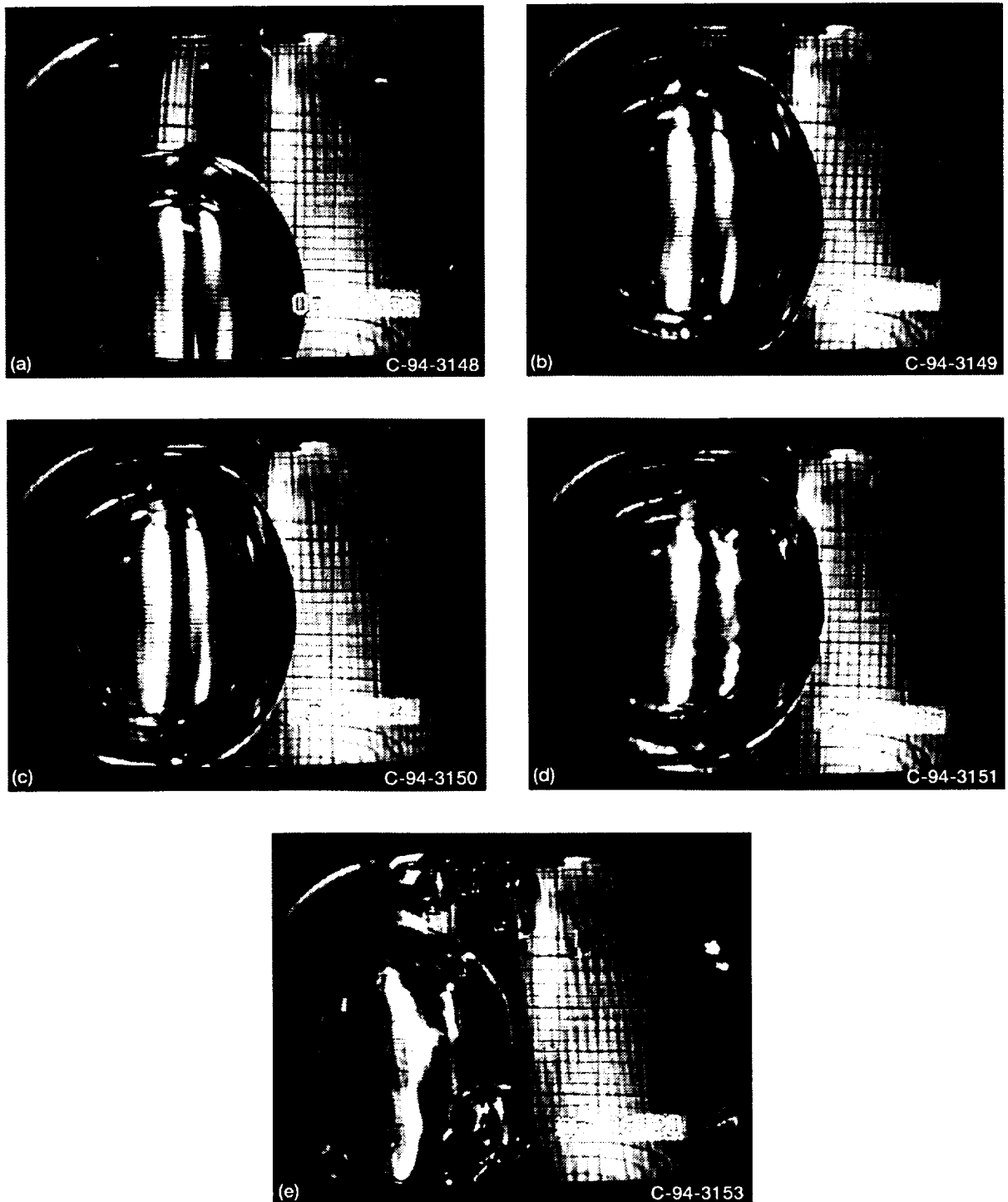


Figure 15.—Still photographs from videotape (run 10) showing location and movement of ullage bubble and boiling on heater B. (a) Initial location of ullage bubble: elapsed heating time, 0 s. (b) Ullage bubble closer to heater surface: elapsed heating, time 2 min and 14 s. (c) Ullage bubble touching heater surface: elapsed heating time, 2 min and 28 s. (d) Inception of boiling on heater B: elapsed heating time, 2 min and 40 s. (e) Steady nucleate boiling on heater B: elapsed heating time, 17 min and 24 s.

system liquid superheating is followed by pressure spikes of varying magnitude due to explosive boiling. From the photographic observation of the boiling process, we qualitatively characterized the explosive boiling as either a rapid growth of vapor mass over the entire heating surface due to flashing of superheated liquid or a violent boiling spread following the appearance of single bubbles on the heating surface. In this work no attempt has been made to quantitatively describe the process of explosive boiling in microgravity.

High liquid superheat and explosive boiling occurred during runs 7, 8, 12, 13, 17, and 18 at heat fluxes from 0.89 to 1.04 kW/m^2 . Except for run 18, only heater A was turned on during these tests. The initial tank pressure ranged from 43 to 56 kPa. The heating period for each run lasted 10 min for runs 7 and 8, 18 min for runs 12 and 13, and 20 min for runs 17 and 18. Experimental data show that a relatively high liquid superheat can be sustained for long periods (several minutes) in microgravity. Figures 16(a) to (f) are still photographs taken from the flight videotape for run 13. The sequence of the photographs clearly shows the occurrence of explosive boiling from heater A and the subsequent liquid motion. When heater A was turned on (fig. 16(a)) the ullage bubble was approximately 0.04 m away from heater A. After 9 min and 46 s of heating (fig. 16(b)) the ullage bubble location remained practically unchanged. Figure 17 shows the heater wall temperature and the tank pressure as functions of time for run 13. During 9 min and 46 s of heating the heater surface temperature T_w (measured by thermistor T_3) increased from 26.7°C to 46.2°C . The tank pressure during this time changed only slightly, from 50.3 to 50.7 kPa. The bulk liquid temperature T_1 remained constant at 27.7°C . The wall superheat at this point was about 17.9°C . Figure 18 shows that the liquid temperature T_4 approximately 1 cm away from heater A was 35°C , representing a superheat of 6.7°C . Figure 16(c) shows the inception of explosive boiling accompanied by a pressure spike as indicated in figure 17. The magnitude of the pressure spike, defined as the peak tank pressure minus the pressure at the inception of explosive boiling, was 19.3 kPa in this case. This pressure spike was about 38 percent of the tank pressure at boiling inception. The rapid growth of vapor mass as indicated in figures 16(d) and (e) was due to rapid evaporation. This sudden increase in vapor mass imparted momentum to the liquid bulk, which then induced violent liquid motion and eventually swept away the vapor mass from the heating surface. The heater temperature dropped from 46.2°C to about 30.8°C and remained steady during the rest of the heating period. The vapor blanketing the heating surface could not be sustained at this low heat flux, 0.97 kW/m^2 . The heater surface temperature profile, shown in figure 18, and the video observation beyond 12 min of heating clearly show that stable nucleate boiling continued after the explosive boiling. The heater wall superheat ΔT_{sat} during nucleate boiling was about 0.6°C (table VI).

For runs 7, 8, and 12 the ullage bubble locations during the heating period were nearly identical. Figures 19 to 21 show the location of the ullage bubble for these runs when heater A was turned on. The video observation shows that during heating the ullage bubble movement was confined to within 0.02 m from heater A. Experimental results from test runs 7, 8, and 12 show remarkable similarity. The incipient boiling wall superheats were nearly the same, for each test varying from 10.6 to 11.1°C (table V). Boiling inception was accompanied by rapid growth of vapor mass and momentary pressure spikes varying in magnitude from 11.5 to 13.0 kPa. For the two remaining tests using heater A, runs 6 and 21, boiling occurred at low incipient wall superheats of 5.3°C and 2.8°C , respectively, probably owing to the location and movement of the ullage bubble during heating. The video observation for run 6 shows that the ullage bubble was nearly touching the heater surface at the start of heating. Run 21 was performed in the absence of video recording, but the heater surface temperature histories (figs. A6(b) and A21(b)) suggest a close similarity between these two runs.

Figures 22(a) to (d) show the events occurring during the heating phase of run 12. The ullage bubble location shown in figure 22(a) corresponds to an elapsed heating time of 6 min and 39 s. The bubble location at the start of the heating phase of this run is shown in figure 21. After 8 min and 47 s (fig. 22(b)) boiling with explosive growth of vapor mass occurred. The associated momentary pressure spike was about 13 kPa, as indicated in figure 23. The rapid growth of vapor mass induced significant surface agitation and liquid motion (fig. 22(c)) and the large vapor bubble nearly touching the heater surface acted as a vapor sink to smaller bubbles (fig. 22(d)). The bubbles formed on the heater surface and merged with the large vapor bubble, thus helping to sustain the nucleate boiling in microgravity. A similar phenomenon in a short-duration, reduced-gravity experiment was observed by Siegel and Keshock (ref. 17).

Runs 17 and 18, which also resulted in pressure spikes, were performed in the absence of video recording. Experimental results from run 17 (figs. A17(a) and (b)) show that the tank pressure, heater surface temperature, and fluid temperature variations during the heating phase of this test were nearly identical to those of run 12. The incipient boiling wall superheat was 12.6°C , and it resulted in a pressure spike of 15.8 kPa. The only test with heater B that resulted in a pressure spike was run 18, for which the incipient boiling wall superheat and the pressure spike were 16.3°C and 17.0 kPa, respectively (table V). Comparing the tank pressure and the heater temperature data (figs. A18(a) and (b)) with figs. A13(a) and (b) of run 13 suggests that for run 18 the ullage bubble may have been located far from heater B. Also, the acceleration data (fig. A18(c)) show a spike in the y-component of acceleration in the positive y-direction, which would tend to keep the ullage bubble away from heater B.

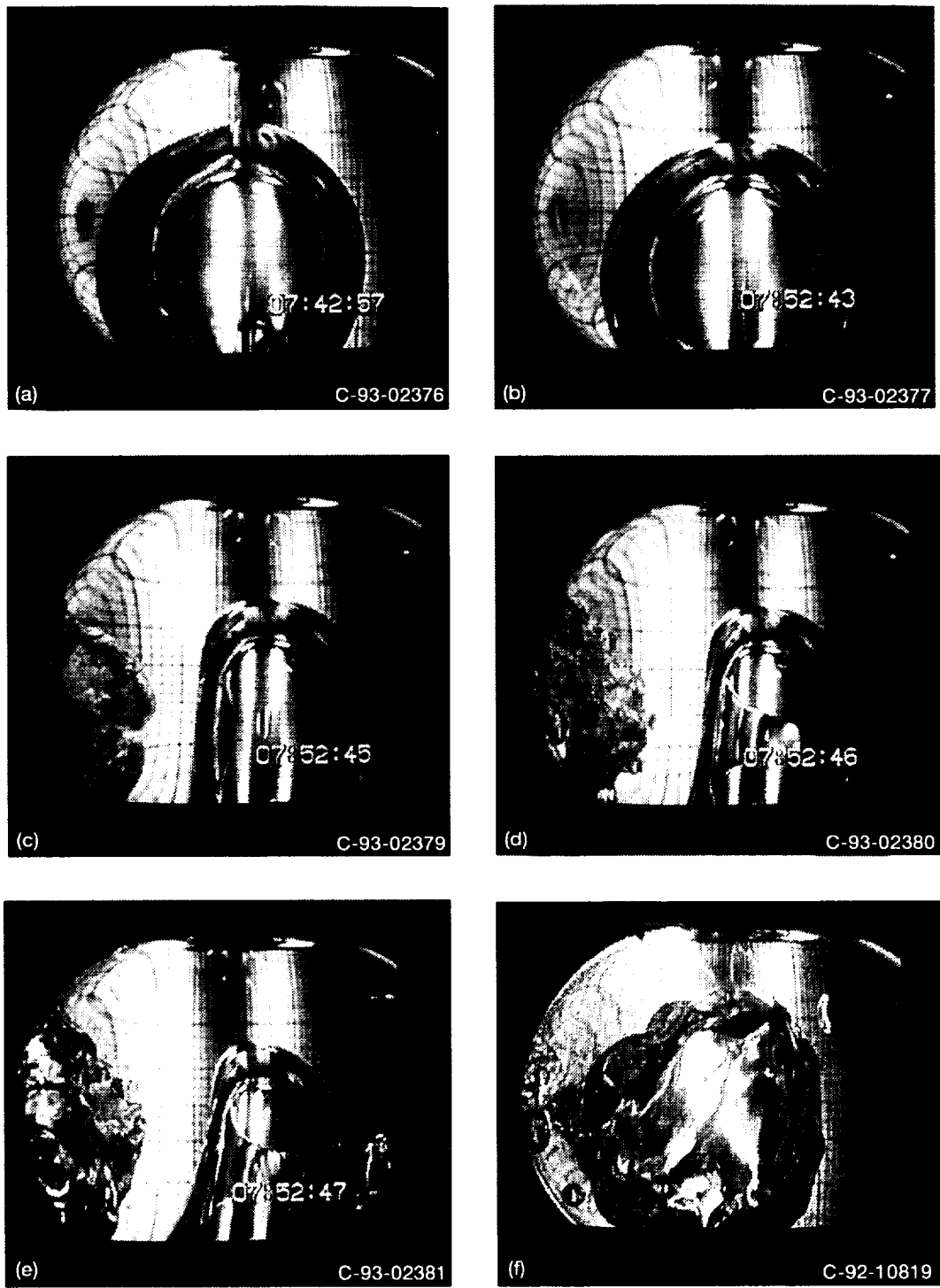


Figure 16.—Explosive boiling from heater A and subsequent events (run 13). (a) Initial liquid-vapor configuration: elapsed heating time, 0 s. (b) Liquid-vapor configuration: elapsed heating time, 9 min and 46 s. (c) Initiation of explosive boiling: elapsed heating time, 9 min and 48 s; wall superheat, 17.9 deg C. (d) Growth of vapor mass and violent bulk liquid motion: elapsed heating time, 9 min and 49 s. (e) Same as (d): elapsed heating time, 9 min and 50 s. (f) Stable nucleate boiling: elapsed heating time, > 12 min.

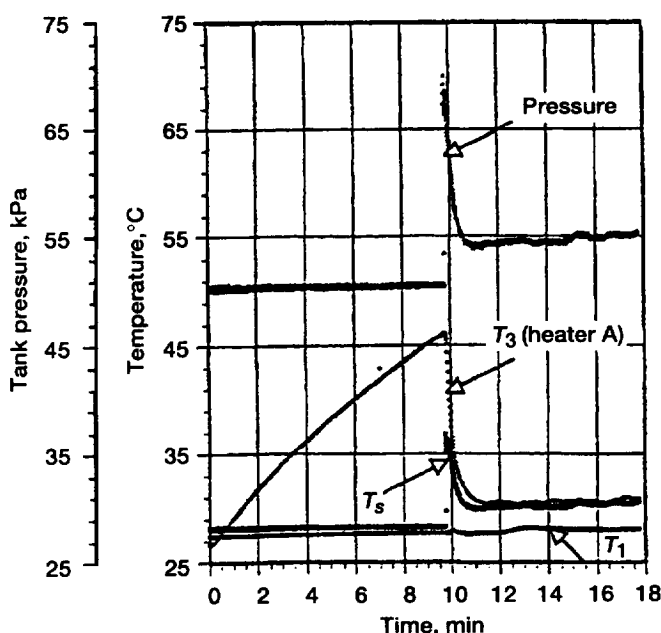


Figure 17.—Heater A and liquid temperatures (T_3 and T_1) and tank pressure as functions of time (run 13).

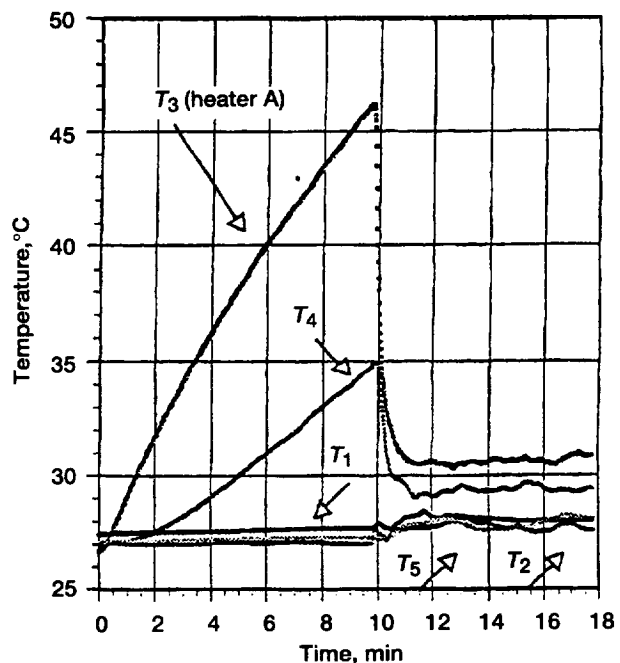


Figure 18.—Heater A and liquid temperatures as functions of time (run 13).

TABLE VI.—WALL SUPERHEAT DURING NUCLEATE BOILING

(a) Heater A

Run	Liquid subcooling, ΔT_{sub} , deg C	Wall superheat, ΔT_{sat} , deg C	Wall heat flux, q_w , kW/m ²
6	2.1	1.1	1.07
7	2.2	.7	1.04
8	2.7	.8	1.03
12	1.0	.4	.98
13	2.0	.6	.97
17	1.9	.6	.95
21	1.0	.8	.89

(b) Heater B

2	2.3	3.3	1.10
3	2.1	4.2	1.07
4	1.7	3.9	1.06
10	1.7	3.4	.98
11	1.5	3.6	.95
18	1.1	2.5	.89
20	1.1	3.0	.86

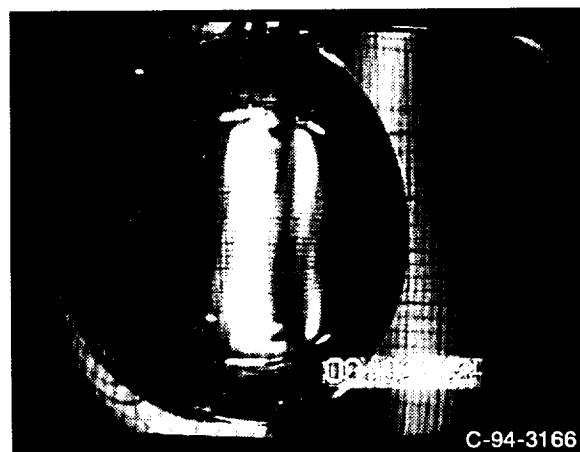


Figure 19.—Initial location of ullage bubble (run 7). Elapsed heating time, 0 s.

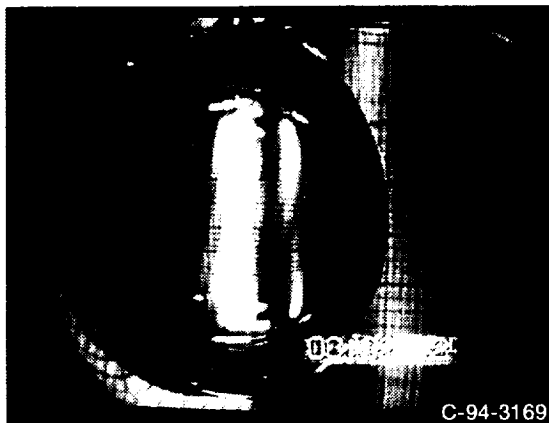


Figure 20.—Initial location of ullage bubble (run 8).
Elapsed heating time, 0 s.

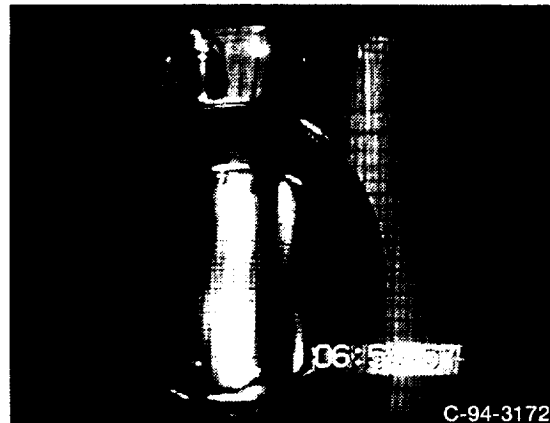


Figure 21.—Initial location of ullage bubble (run 12).
Elapsed heating time, 0 s.

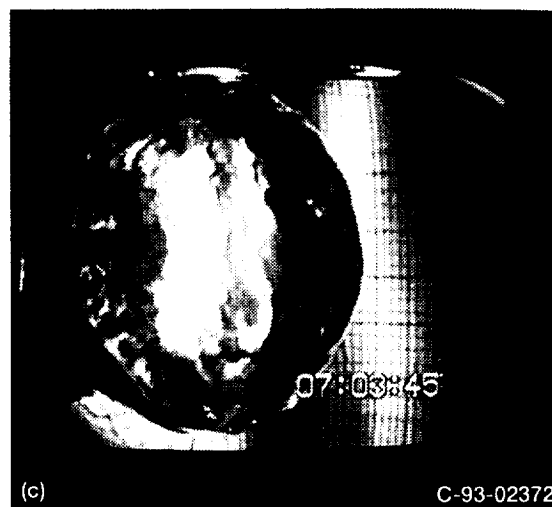
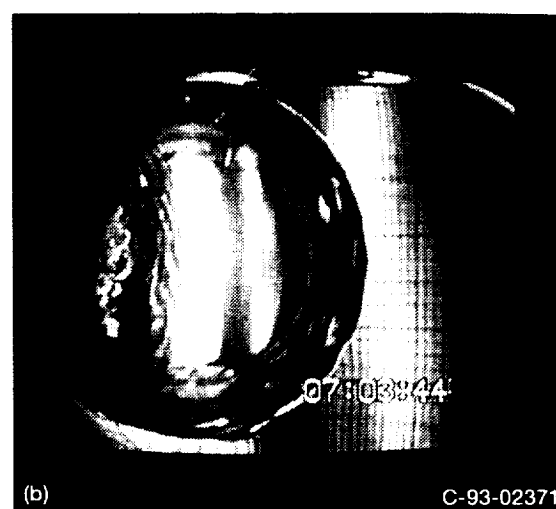
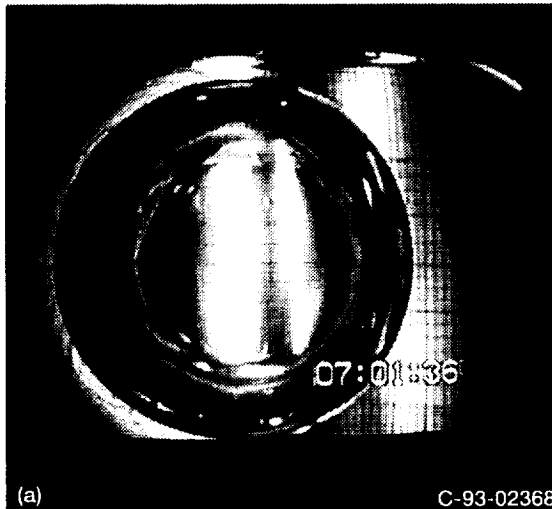


Figure 22.—Boiling process on heater A (run 12). (a) Ullage bubble location: elapsed heating time, 6 min and 39 s.
(b) Explosive growth of vapor mass: wall superheat 10.6 deg C; elapsed heating time, 8 min and 47 s.
(c) Growth of vapor mass, surface agitation, and bulk liquid motion.
(d) Stable nucleate boiling (ullage bubble acts as sink to smaller bubble.)

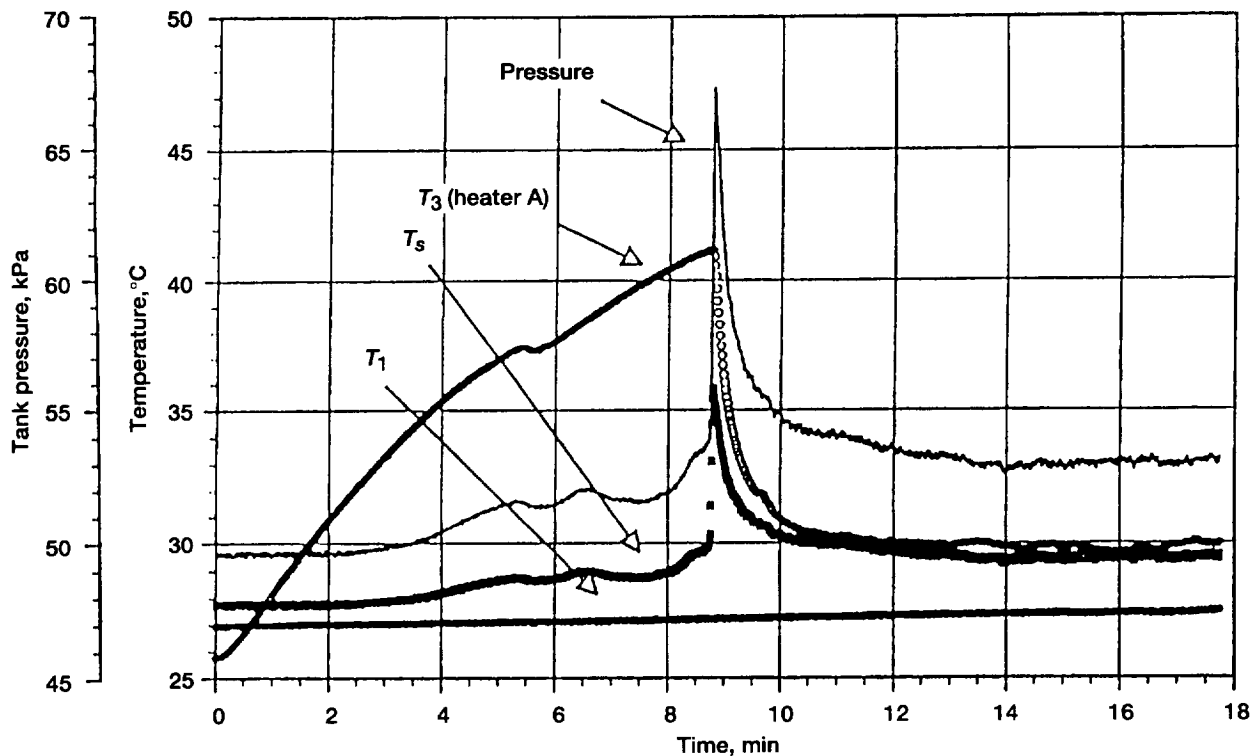


Figure 23.—Heater A and liquid temperatures and tank pressure as functions of time (run 12).

The explosive boiling observed in microgravity under very slow heating is distinctly different from explosive boiling under rapid heating (refs. 18 and 19). However, the type of explosive boiling described in this report was also observed by Ervin et al. (ref. 20) in a microgravity pool boiling experiment with nearly saturated Freon 113 performed in the drop tower at the NASA Lewis Research Center. Explosive boiling from a flat heating surface was observed at a heat flux of 54 kW/m^2 . A lower limit of heat flux that might produce this type of boiling could not be established because the time available in microgravity was too short (5.1 sec) for boiling incipience to take place at the low heat flux level. In the drop tower tests a heat flux of 40 kW/m^2 did not result in incipient boiling (ref. 21). The results obtained in the present tests, performed in the long-duration microgravity environment of the space shuttle, show that explosive boiling from a large heating surface can be produced with a heat flux of about 1 kW/m^2 .

Steady nucleate boiling.—For test runs with heater B boiling occurred (except for run 18) within 2 to 4 min of heating. The incipient boiling wall superheat varied from 5 to 7 deg C for a heat flux of about 1.0 kW/m^2 . After boiling inception the heater wall temperature dropped by about 2 deg C and then remained nearly constant during the rest of the heating period. Figure 24 shows heater B surface temperature as measured by thermistor T_6 as a function of time for run 10. The figure also includes the tank pressure, the saturation temperature corre-

sponding to the tank pressure, and the bulk liquid temperature as measured by thermistor T_1 . This figure is representative of all test runs with heater B, except run 18. Figure 25, a still photograph taken from videotape for run 10 after 17 min and 2 s of elapsed heating time, clearly shows the growth and departure of bubbles from the heater surface. The heater temperature history after 6 min as shown in figure 24 and the bubble growth and departure as shown in figure 25, or more vividly in the video tape, clearly demonstrate that steady nucleate boiling is viable in a long-duration, low-gravity condition at low heat fluxes. For run 10 the wall heat flux was 0.98 kW/m^2 and the wall superheat ΔT_{sat} during steady nucleate boiling was about 3.4 deg C for a liquid subcooling ΔT_{sub} of about 1.7 deg C. The wall superheat values during nucleate boiling for all other runs, along with their corresponding heat fluxes, are listed in table VI. For the same heat flux the wall superheat during nucleate boiling for heater A (0.4 to 1.1 deg C) was lower than that for heater B (2.5 to 4.2 deg C). For heater A a relatively high incipient boiling superheat resulted in explosive boiling with a rapid growth in vapor mass. The sudden increase of vapor mass induced violent liquid motion and swept away the vapor bubbles from the heater surface, lowering heater surface temperature. Also, during tail-first orbiter attitude the ullage bubble remained close to heater A and acted as a vapor sink to smaller bubbles. The bubbles formed on the surface of heater A merged with the ullage bubble while they were relatively small. This

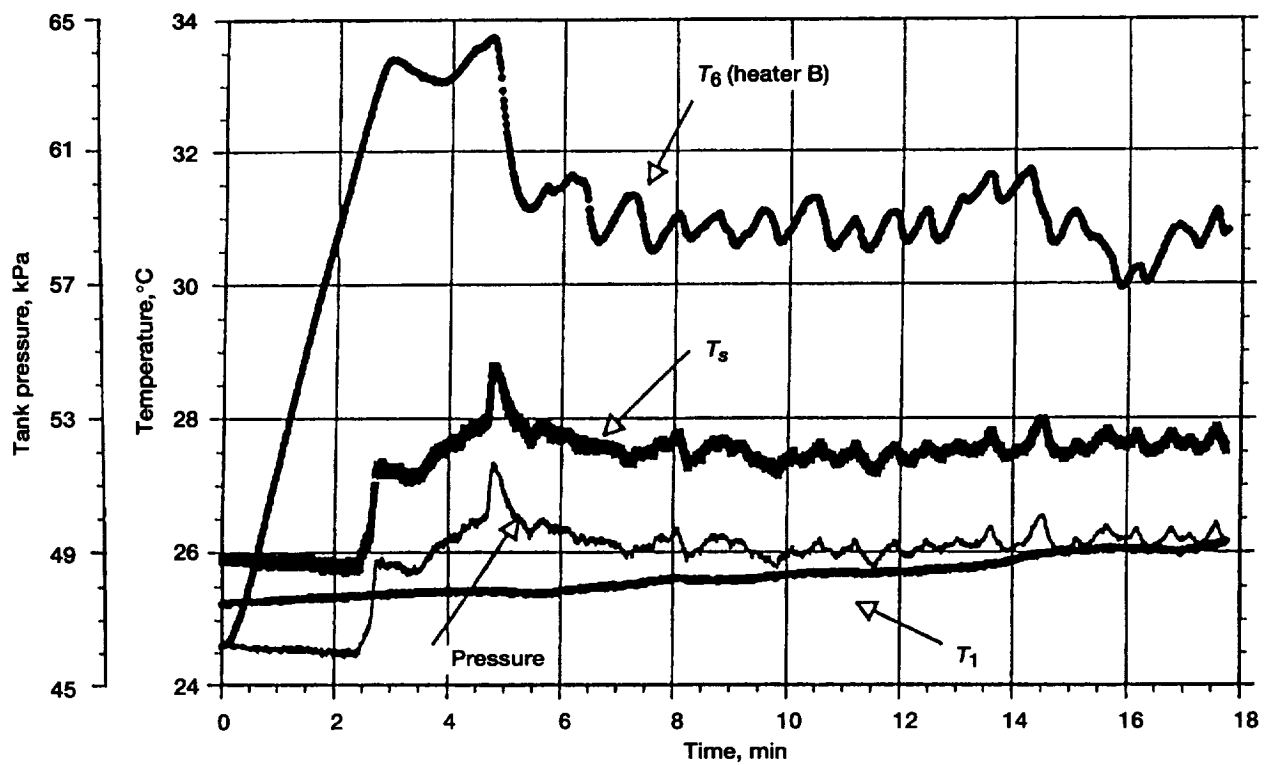


Figure 24.—Heater B and liquid temperatures and tank pressure as functions of time (run 10).

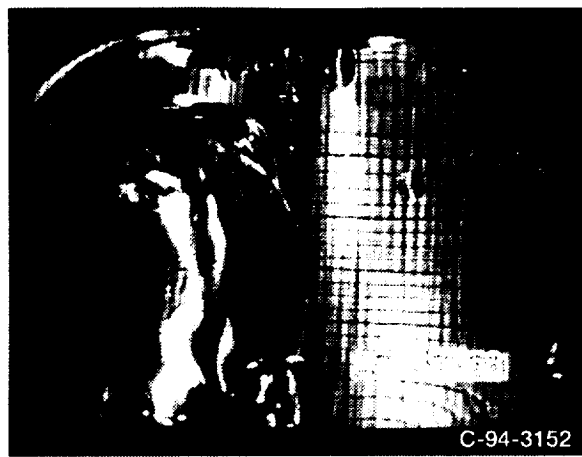


Figure 25.—Bubble growth and departure from heater B (run 10). Elapsed heating time, 17 min and 2 s.

process also helped to enhance heat removal from the heater surface.

For runs 11 and 20 the tank pressure started to increase sharply immediately (within 30 s) after the start of heating. In contrast, in all other test runs the tank pressure changed only slightly up to the point of boiling inception. The tank pressure histories for runs 11 and 20 are shown in figures A11(a) and A20(a), respectively. Figures 26(a) to (e), taken from the flight videotape of run 11, show the location and movement of the ullage bubble and the boiling process on heater B for this run. At the start of heating (fig. 26(a)) the ullage bubble was touching one side of heater B. After 1 min and 9 s of heating (fig. 26(b)) the ullage bubble was in contact with the heating surface. Video observation shows that there was no bubble formation anywhere on the heating surface during this elapsed heating period. Therefore, the sharp increase in the tank pressure rise rate is due to the evaporation of the thin liquid layer separating the heater surface and the ullage bubble. After 1 min and 35 s of heating time (fig. 26(c)) the ullage bubble had moved away from heater B, probably owing to a spike in the y -component of acceleration in the negative y -direction. Figures 26(d) and (e) show boiling inception and the continuation of the nucleate boiling process. Figure 27 shows heater B surface temperature T_w measured by thermistor T_6 , the liquid temperature measured by thermistor T_1 , and the tank pressure as functions of time for run 11. Included in this figure is the saturation temperature T_s corresponding to the instantaneous tank pressure. Note that after 3 min of heating the difference between heater surface temperature and saturation temperature $T_w - T_s$ was nearly constant during the remaining heating period, showing the sustainability of nucleate boiling in microgravity.

During the heating phase of runs 15, 16, and 19 heaters A and B were turned on simultaneously. The total power input for each test was about 7.3 W. Power input to the individual heaters was not measured, but the heating elements of both heaters were similar. Also, the surface areas of both heaters were nearly equal. Therefore, the heat flux was calculated by dividing the total power input by the total surface areas of heaters A and B. The heat flux for these tests was about 0.23 kW/m². The wall superheat varied from 3.0 to 4.5 deg C for heater A and from 6.5 to 7.5 deg C for heater B. The video observation of runs 15 and 16 did not show any bubble formation during 18 min of heating. The heating period of run 19 was extended to 40 min and was performed without video recording. The tank pressure and heater temperature data (figs. A19(a) and (b)) show a pressure spike and an abrupt drop in heater temperature after 38 min of heating, suggesting that explosive boiling of the type described above may have occurred in this case.

The most important result of practical significance for the storage of cryogenic liquid in microgravity is the pressure spike due to explosive boiling. The magnitude of the pressure spike will depend on the degree of liquid superheat and the

liquid volume fraction (also referred to as fill level). Experimental results show that for the 83-percent liquid fill level used in this experiment a higher wall superheat at boiling inception resulted in a higher pressure spike. This result was expected because a higher superheated condition results in more rapid growth of vapor mass. However, the incipient boiling wall superheat in this experiment was found to be affected by the location of the ullage bubble. The highest superheat occurred when the ullage bubble was the farthest from heater A (run 13). Temperature data recorded in the present experiment were not sufficient to quantify the effect of ullage location on the sustainable liquid superheat.

Mixing Phase

The jet-induced fluid mixing experiment was performed at low jet flow rates. Except for runs 1, 5, 9, and 14 the jet flow rate, which varied from 0.2 to 1.8 liters/min, was kept constant during a test. The jet Reynolds number Re_j and the jet Weber number We_j corresponding to these flow rates varied from 1900 to 8000 and 0.2 to 6.5, respectively. The jet Weber number is defined as the ratio of the jet's momentum to the surface tension force at the liquid-vapor interface:

$$We_j = \frac{\rho(V_o D_o)^2}{4\sigma D_j} \quad (1)$$

where V_o is the jet velocity at the nozzle outlet, D_o is the jet diameter at the nozzle outlet, and D_j is the jet diameter at the liquid-vapor interface. Figure 28 describes the pertinent variables in the definition of We_j . This definition of Weber number is adopted from reference 5. The estimation of the jet diameter at the liquid-vapor interface is based on the following assumptions:

1. The jet spread half-angle is 7° for the first 12.4 outlet diameters and 11° thereafter.
2. The distance from the nozzle outlet to the interface h_b is 0.127 m.

The first assumption is based on the findings (ref. 5) of the spread angles for submerged turbulent jets in drop tower tests. The second assumption is an approximation based on the following: For an 83-percent fill level a spherical ullage has a diameter of 0.165 m. If the ullage is located at the opposite end of the tank at the moment when the jet either penetrates it or is resisted by the interface, the distance to the closest point of the sphere is 0.127 m. Using the nozzle outlet diameter of 0.01 m and the above spread angles results in a constant D_j of 0.0494 m. It is recognized that D_j may vary somewhat from this approximation as the location and shape of the ullage changes. However, scaling of D_j from the video images

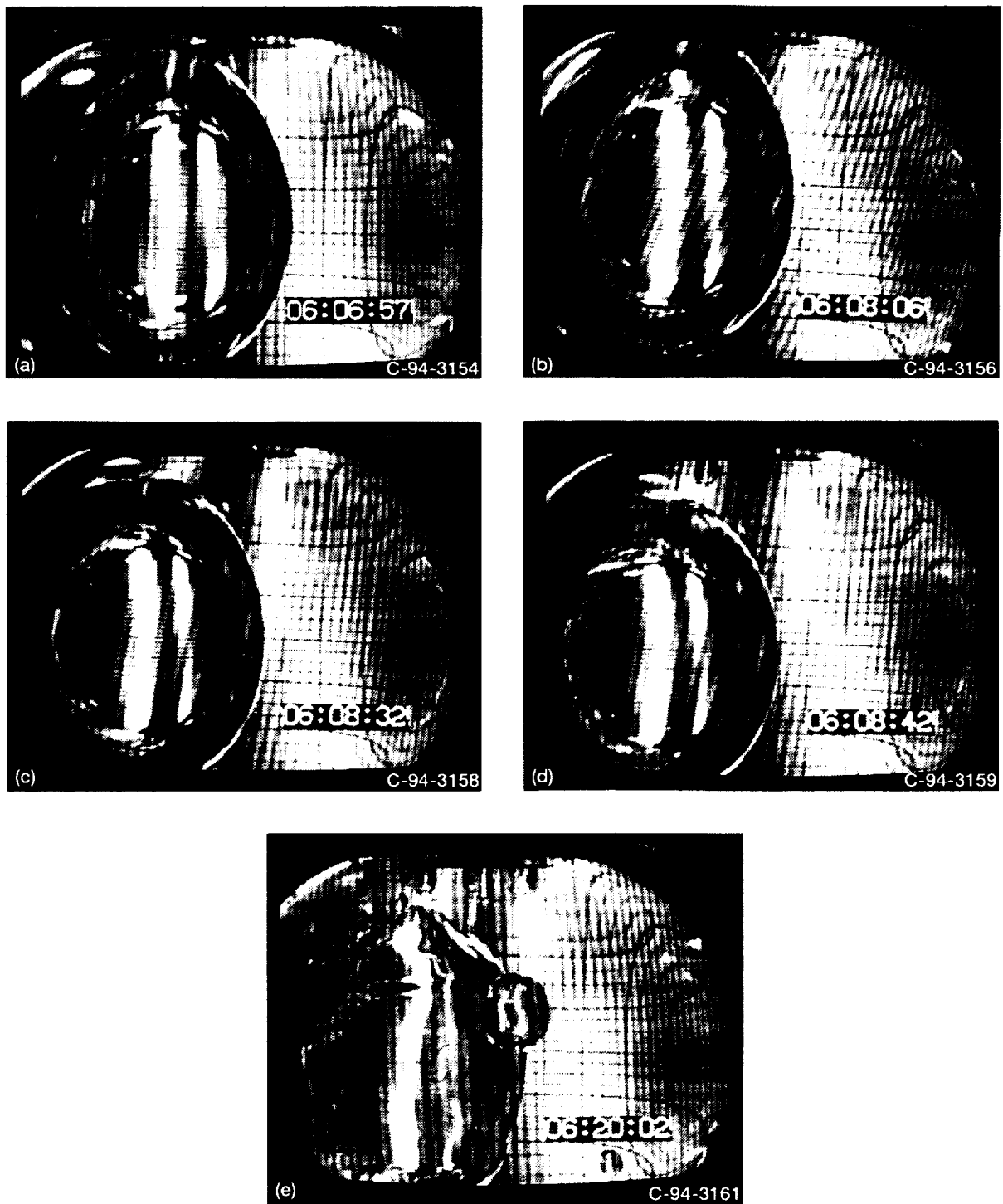


Figure 26.—Still photographs from videotape showing location and movement of ullage bubble and boiling on heater B (run 11). (a) Location of ullage bubble at start of heating: elapsed heating time, 0 s. (b) Ullage bubble location: elapsed heating time, 1 min and 9 s. (c) Ullage bubble moved away from heater: elapsed heating time, 1 min and 35 s. (d) Bubble formation and growth on heater B: elapsed heating time, 1 min and 45 s. (e) Steady nucleate boiling: elapsed heating time, 13 min and 5 s.

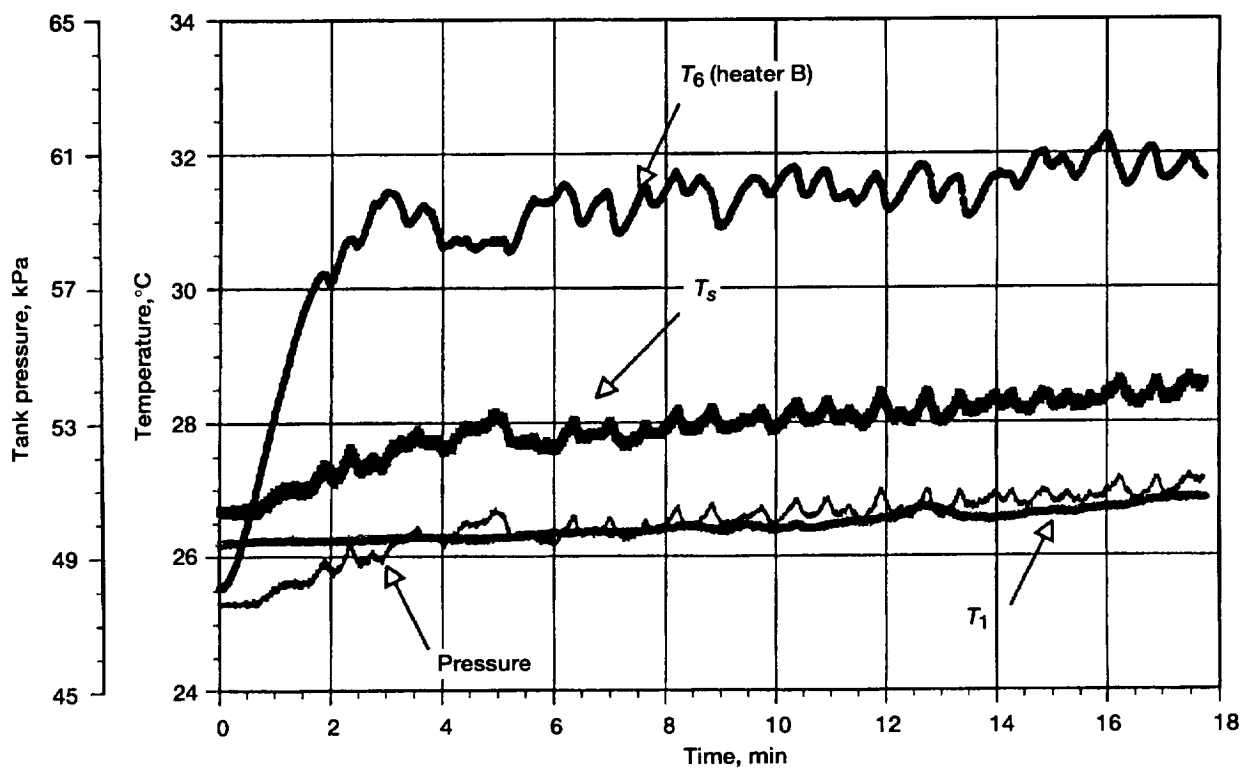


Figure 27.—Heater B and liquid temperatures (T_6 and T_1) and tank pressure as function of time (run 11).

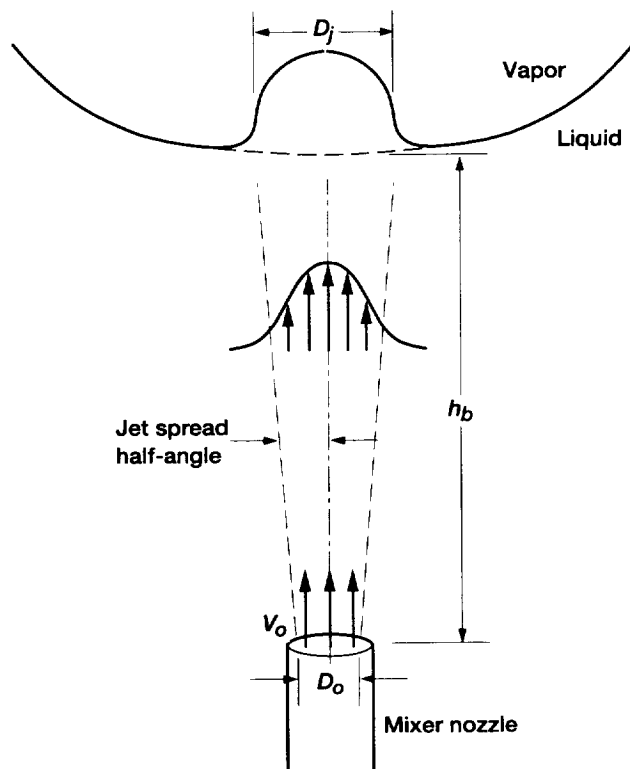


Figure 28.—Jet and liquid-vapor interface interaction.

suggests that this diameter is correct to within 20 percent in both the symmetrical nonpenetrating and penetrating flow patterns.

At low Weber numbers the jet impinges on the ullage bubble, forming a bulge, but does not penetrate the interface. This flow pattern, which is generally found to be axisymmetric and stable, is comparable to flow pattern I defined in reference 5. At somewhat higher Weber numbers the jet may initially form a geyser in the center of the ullage, but it rapidly deflects to one side and remains asymmetric. At still higher Weber numbers the jet completely penetrates the ullage, reaches the opposite end of the tank, and recirculates along the tank wall. This flow pattern, comparable to flow pattern IV (ref. 5), was observed to be asymmetric at times and to sometimes flip-flop between symmetric and asymmetric behavior.

For each run having a nonzero flow rate the observed flow patterns and the corresponding Weber numbers in ascending order of flow rate are listed in table VII. The table includes results from both flight experiments TPCE (STS-43) and TPCE/TP (STS-52). The classification of the observed flow patterns was described by Bentz et al. (ref. 15). Comparing the results shows that under identical flow conditions similar flow patterns were obtained from both flight experiments. Nonpenetration is seen at $We_j < 1.5$, although at $We_j = 1.5$ the flow was only marginally in this category and was at times asymmetric. For $3 < We_j < 5$ the flow was symmetric, and for $We_j > 5$ the flow pattern was generally in the penetrating symmetrical classification.

The jet-induced fluid mixing process described above may be quantified either in terms of a pressure or temperature equilibration rate. An important parameter of practical interest for tank pressure control is the mixing time based on the pressure equilibrium. Bentz et al. (ref. 15) analyzed the fluid mixing data and quantified the results in terms of a pressure collapse time, which is defined as the time required for the mixer to reduce the tank pressure to 75 percent of its equilibrium value,

$$\frac{P - P_{eq}}{P_i - P_{eq}} = 0.25 \quad (2)$$

where P is the instantaneous tank pressure, P_i is the pressure at the initiation of mixing, and P_{eq} is the equilibrium pressure attained during mixing. The rationale for selecting 75-percent pressure collapse time is given in reference 13. Figure 29 (taken from ref. 15) shows a plot of pressure collapse time as a function of Weber number. Results from the first flight experiment, TPCE (STS-43), are also included in the figure for comparison. The open symbols are data from the TPCE, and the solid symbols are the present data (TPCE/TP).

TABLE VII.—FLOW PATTERNS FOR JET WEBER NUMBERS: TPCE AND TPCE/TP RESULTS

Mission/run	Flow rate, liter/min	Jet Weber number, We_j	Pattern
STS-43/25	0.378	0.288	Nonpenetrating
STS-43/32	.385	.298	
STS-52/02	.435	.381	
STS-52/06	.454	.416	
STS-52/13	.517	.539	
STS-43/03	.541	.590	
STS-43/11	.593	.708	
STS-43/16	.596	.717	
STS-43/08	.603	.732	
STS-43/20	.604	.735	
STS-43/23	.619	.773	
STS-43/33	.638	.821	
STS-43/27	.801	1.293	
STS-52/07	.820	1.357	
STS-52/03	.835	1.405	
STS-43/31	.845	1.438	
STS-52/10	.875	1.545	
STS-52/04	1.220	3.000	Asymmetrical
STS-43/29	1.239	3.095	
STS-43/26	1.243	3.113	
STS-52/12	1.278	3.291	
STS-52/08	1.283	3.319	
STS-43/04	1.532	4.730	
STS-43/07	1.533	4.736	
STS-43/15	1.534	4.742	
STS-43/12	1.540	4.781	Penetrating
STS-43/34	1.541	4.787	Asymmetrical
STS-43/24	1.569	4.963	Penetrating
STS-43/19	1.585	5.062	Penetrating
STS-52/15	1.595	5.126	Asymmetrical
STS-52/16	1.643	5.444	Penetrating
STS-43/28	1.711	5.901	Asymmetrical
STS-43/30	1.768	6.303	Penetrating
STS-43/02	2.683	14.509	
STS-43/05	2.719	14.905	
STS-43/10	2.742	15.155	
STS-43/13	2.777	15.550	
STS-43/17	2.784	15.621	
STS-43/36	2.825	16.084	
STS-43/22	2.836	16.219	
STS-43/37	3.339	22.477	
STS-43/38	3.351	22.637	

Figure 29 shows that the pressure collapse times from the two flight experiments were consistent and repeatable and suggests the possibility of describing the mixing time as a function of Weber number.

The dimensionless mixing time t^* from both flight experiments and the ground simulation using Freon 113 are plotted in figure 30 as a function of Richardson number Ri . The dimensionless mixing time is defined as $t^* = tV_oD_o/D^2$, where the mixing time t is the time required from the start of a

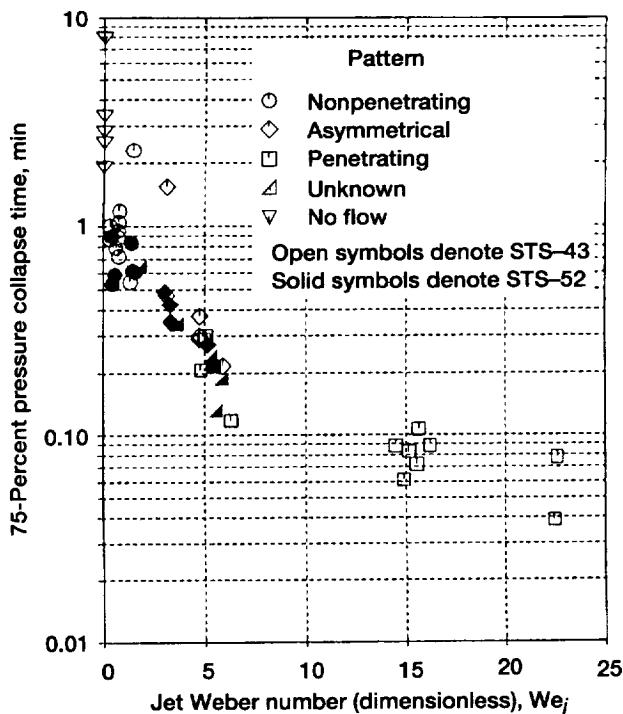


Figure 29—Pressure collapse time as function of jet Weber number.

mixing operation to the time when equilibrium tank pressure is achieved. The Richardson number, which scales the buoyancy effect, is defined as $Ri = g\beta(T_s - T_1)h_b/V_o^2$. The figure also includes Lin et al.'s (ref. 22) jet-induced mixing results for a thermally stratified liquid hydrogen tank. For the flight experiments Ri approached zero. For the normal-gravity experiments Ri approached zero for high jet flow velocities. Comparing the results obtained from the flight experiments with the normal-gravity results suggests the possibility of developing a method to extrapolate normal-gravity, jet-induced mixing results to microgravity conditions.

Effect of noncondensable gas.—The mixing time definition based on the pressure equilibrium should be affected by the pressure decay rate, which is controlled by the vapor condensation rate at the interface and the thermodynamic state of the vapor. The vapor condensation rate may be reduced significantly by the presence of noncondensable gases. During the TPCE (STS-43) the sum of partial pressures of noncondensable gases P_{nc} was estimated to be 4.2 kPa. For the present experiment (STS-52) P_{nc} was reduced to about 1.0 kPa. The mass fraction of noncondensable gases for this range of P_{nc} is estimated to vary from 0.5 to 2.0 percent. Figure 31 compares the pressure decay from the two flight experiments under nearly identical flow conditions. These experiments did not provide the necessary data to quantify the effects of noncondensable gas. However, comparing the pressure decay data suggests that for noncondensable mass fractions of less than 2 percent its effects on the vapor condensation rate may be neglected.

Flow patterns in absence of heating.—Video observations of runs 1, 5, 9, and 14 clearly demonstrate the response of the liquid-vapor interface and the flow pattern transition as a function of the jet flow rate. These four runs, with nearly identical initial conditions, were performed in the absence of heating. The jet flow rate was planned to increase in steps of 0.19 liter/min every 30 s over a 6-min period to help determine the boundaries of the various flow regimes. Figure 32 shows the actual flow rates obtained during these four runs. Figure 33, still photographs taken from the video recording of run 14, shows that at flow rates of 0.3 and 0.5 liter/min the jet impinged on the ullage bubble, forming a bulge. The jet Weber numbers corresponding to these flow rates are 0.2 and 0.5, respectively. At flow rates of less than 0.7 liter/min a stable geyser formed in the center of the ullage. The stable geyser could not be sustained for jet flow rates corresponding to Weber numbers greater than 1.5. Comparing video observations of these runs shows remarkable similarity in the response of the liquid-vapor interface and the flow transition under identical flow conditions. Experimental results of these four runs along with their video observations provide an excellent data base for comparing microgravity computational fluid dynamics codes.

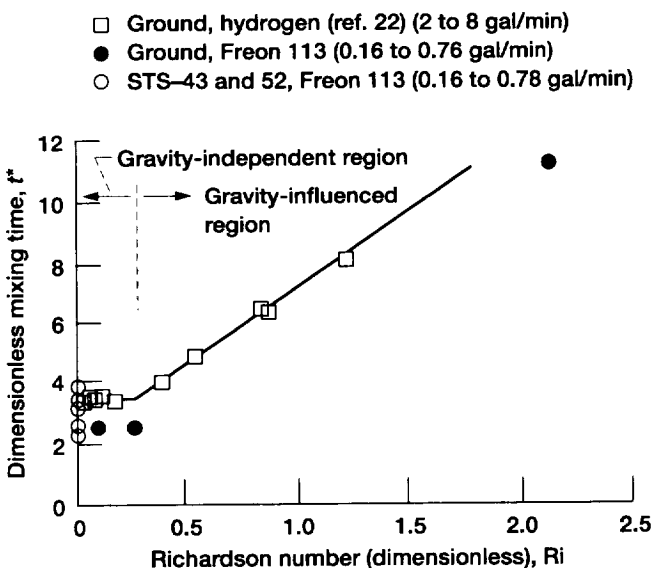


Figure 30.—Dimensionless mixing time as function of Richardson number (comparison of STS-42 flight data with ground data).

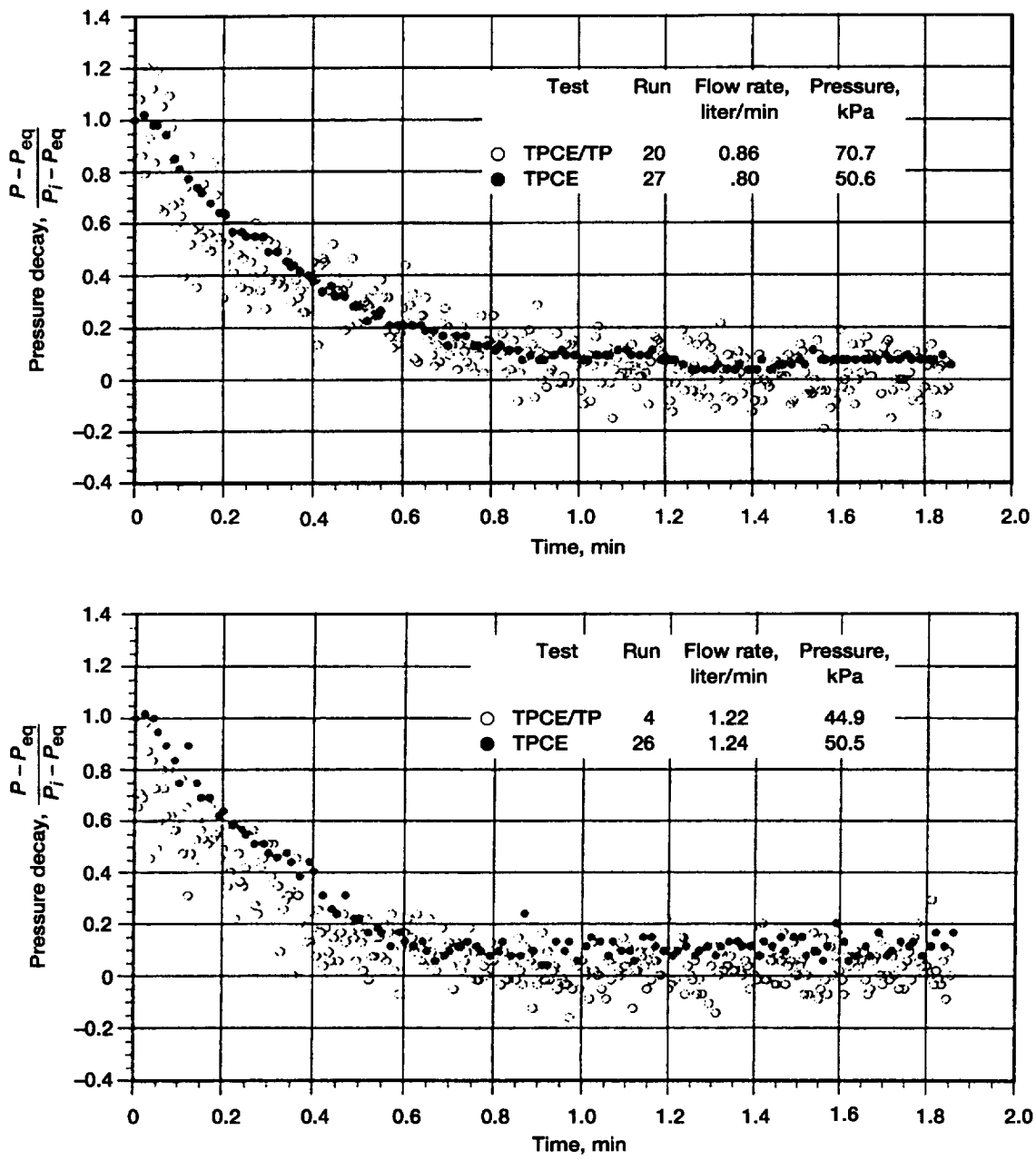


Figure 31.—Comparison of TPCE and TPCE/TP mixing results: effect of noncondensable gas on pressure decay rate.

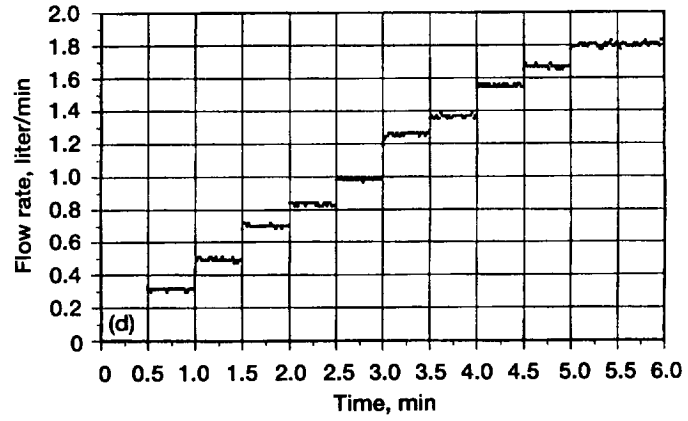
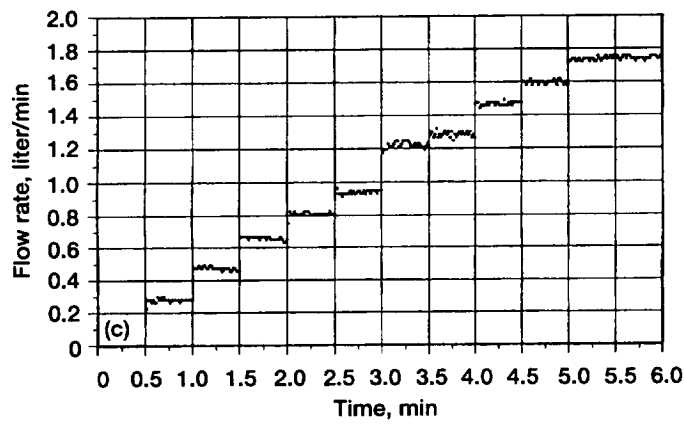
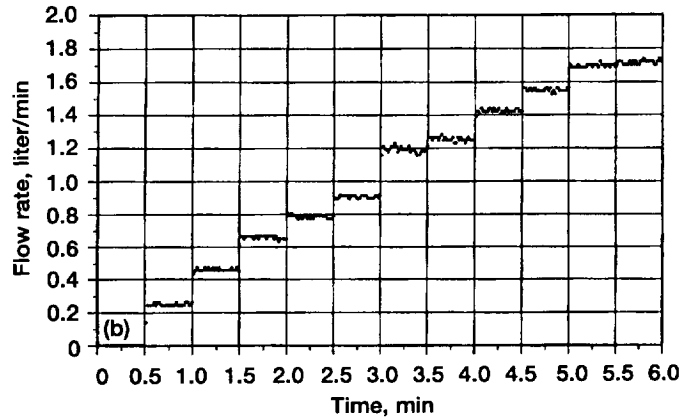
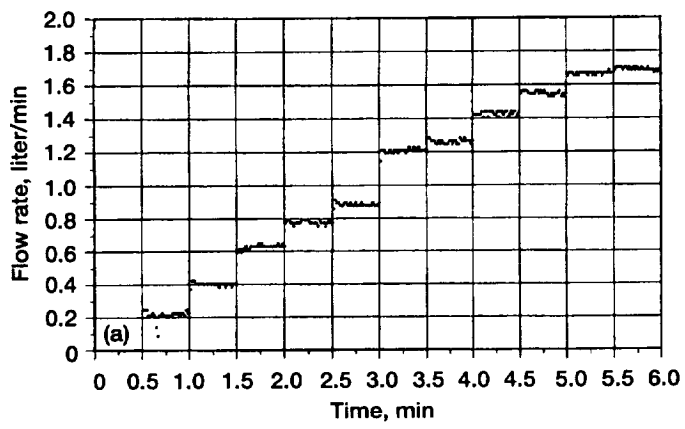


Figure 32.—Jet flow rate variation. (a) Run 1. (b) Run 5. (c) Run 9. (d) Run 14.

Conclusions

The experimental results are presented here for the flight experiment TPCE/TP performed in the microgravity environment of space shuttle flight STS-52. Results include experimental data and video observations of pool boiling in nearly saturated (<1 deg C subcooling) Freon 113 and low-velocity, axial, jet-induced mixing in a partially filled tank. Preliminary evaluation and analyses of data gave the following results:

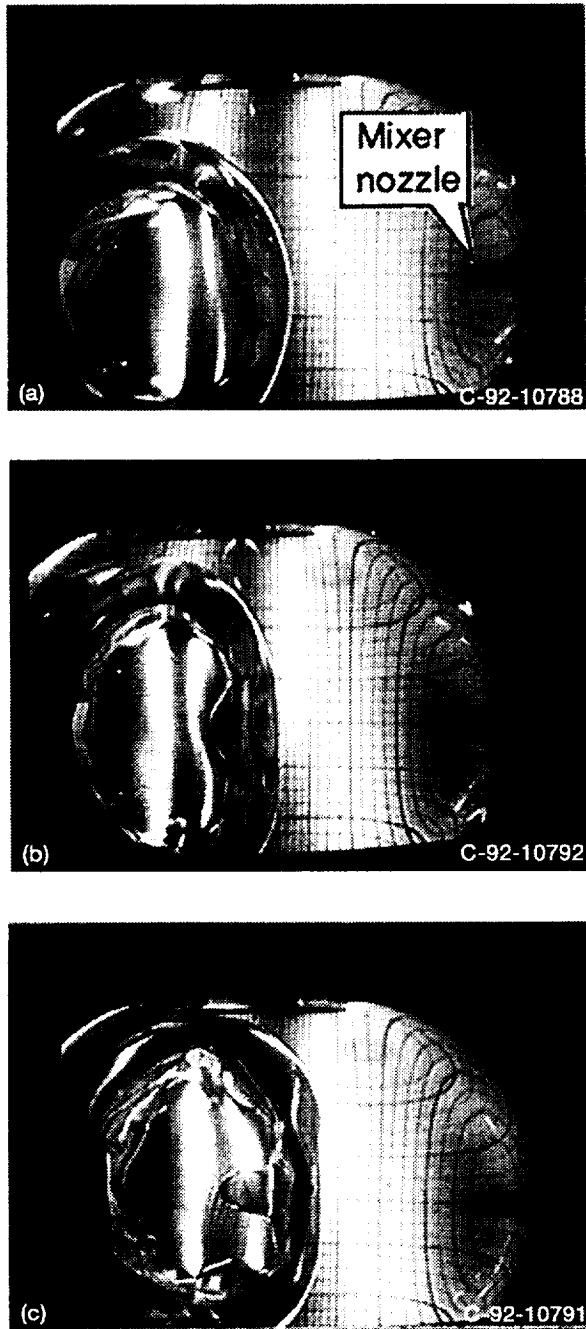


Figure 33.—Interface response and flow pattern transition during jet-induced mixing. (a) Flow rate, 0.3 liter/min. (b) Flow rate, 0.5 liter/min. (c) Flow rate, 0.7 liter/min.

1. The pool boiling data at low heat fluxes, 0.8 to 1.1 kW/m^2 , clearly demonstrated that nucleate boiling is viable in microgravity. However, the heat flux range covered in this experiment was not sufficient to determine the span of the nucleate boiling regime.

2. The data also demonstrated the sustainability of high liquid superheat for long periods and the occurrence of explosive boiling at low heat fluxes. In a closed system explosive boiling due to flashing of superheated liquid resulted in pressure spikes and violent bulk liquid motion.

3. For a given liquid fill level a higher incipient wall superheat resulted in a higher pressure spike. For a heat flux of 0.97 kW/m^2 a wall superheat of 17.9 deg C was attained in 10 min of heating, resulting in a pressure spike of about 19.3 kPa. The magnitude of the pressure spike in this case was about 38 percent of the tank pressure at the inception of boiling.

4. Fluid mixing results from this experiment and comparison with the TPCE results showed that the flow patterns produced by an axial jet can be classified in terms of the jet Weber number. A stable geyser at the liquid-vapor interface was sustainable for Weber numbers less than 1.5. At Weber numbers greater than 5 the jet completely penetrated the ullage.

5. Mixing time based on the pressure decay rate or the pressure collapse time can be described as a function of Weber number.

6. Comparing the mixing time results from the flight experiments with the normal-gravity results showed that high-velocity (Richardson number < 0.5 for cylindrical tanks), normal-gravity mixing results may be applicable for microgravity conditions.

7. Comparing pressure decay data suggests that the effects of noncondensable gases on the vapor condensation rate may be neglected for noncondensable mass fractions of less than 2 percent.

Lewis Research Center
National Aeronautics and Space Administration
Cleveland, Ohio, August 29, 1995

Appendix—Experimental Results for All 21 Test Runs

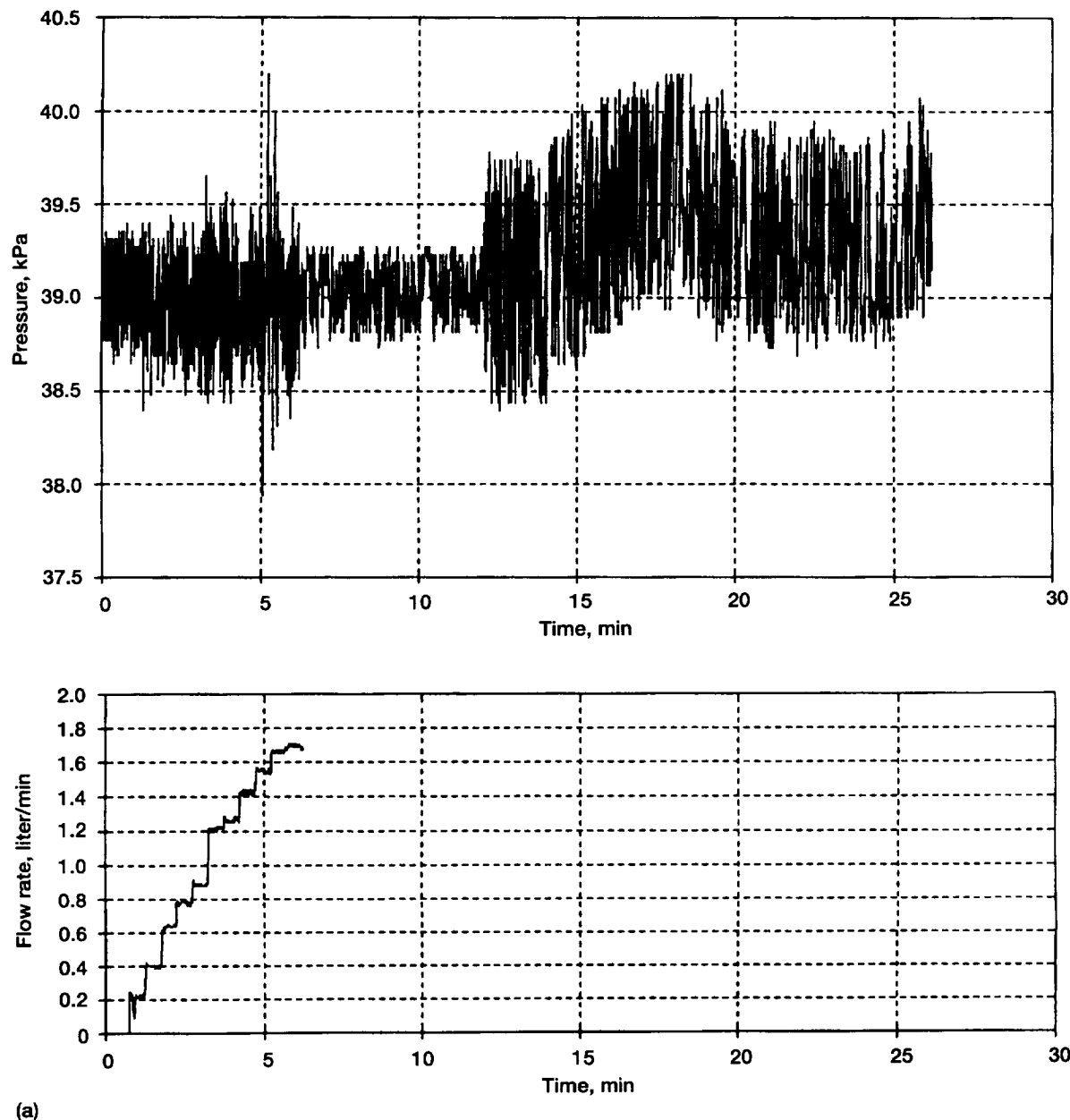


Figure A1.—Run 1. (a) Pressure and flow rate. (b) Fluid and heater temperatures. (c) Accelerations.

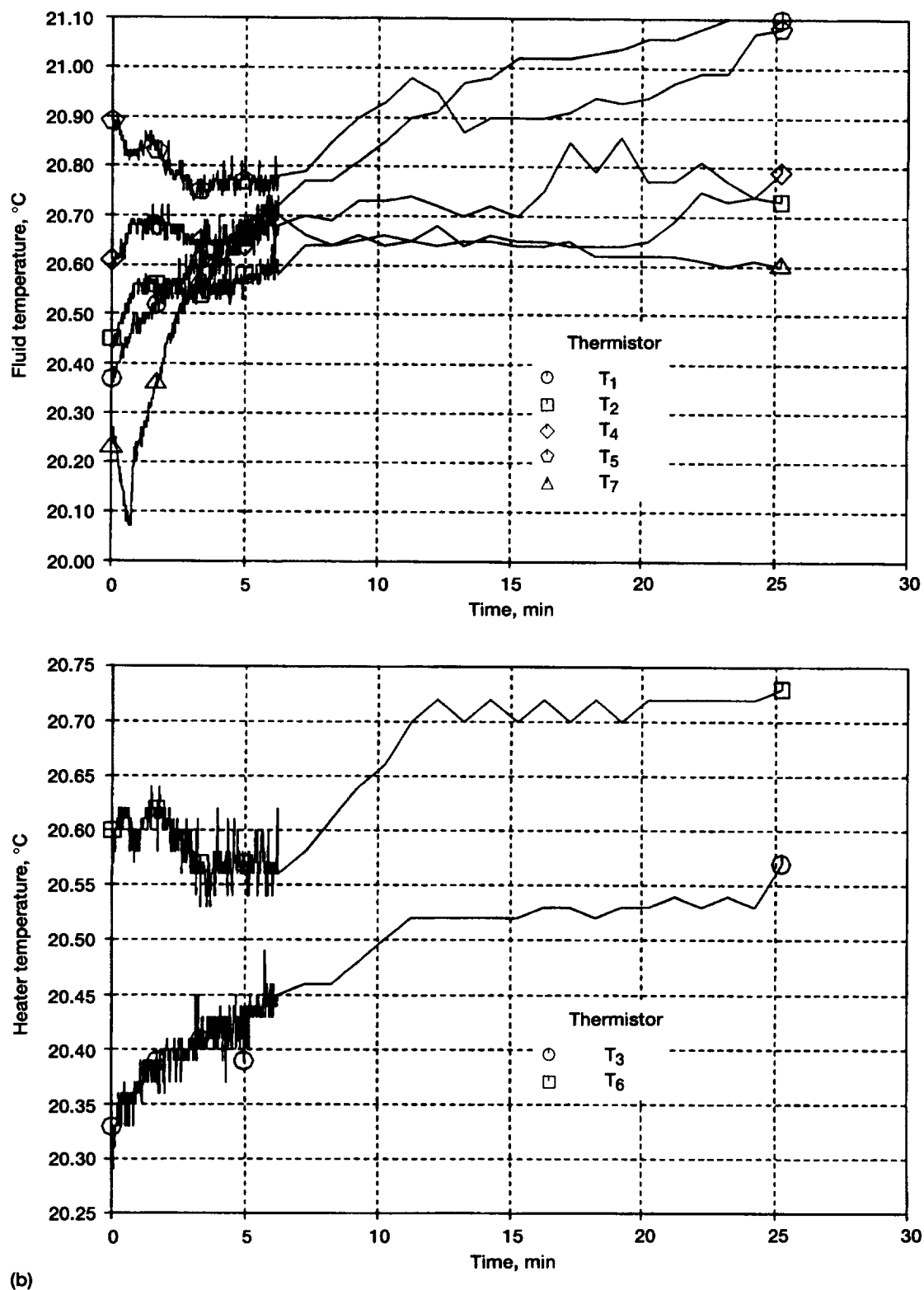
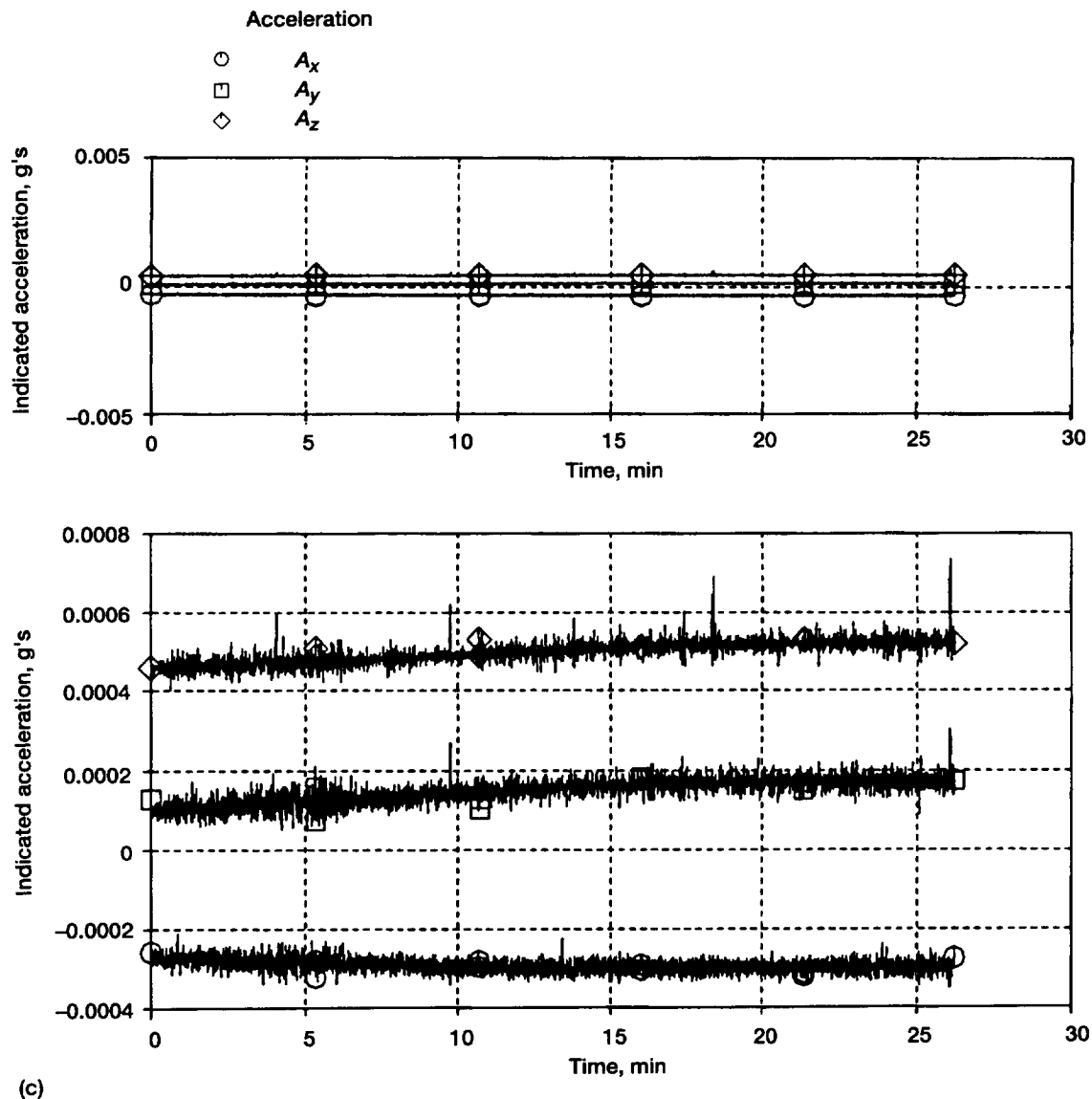


Figure A1.—Continued. (b) Fluid and heater temperatures.



(c)

Figure A1.—Concluded. (c) Accelerations. (Bottom graph shows expanded scale.)

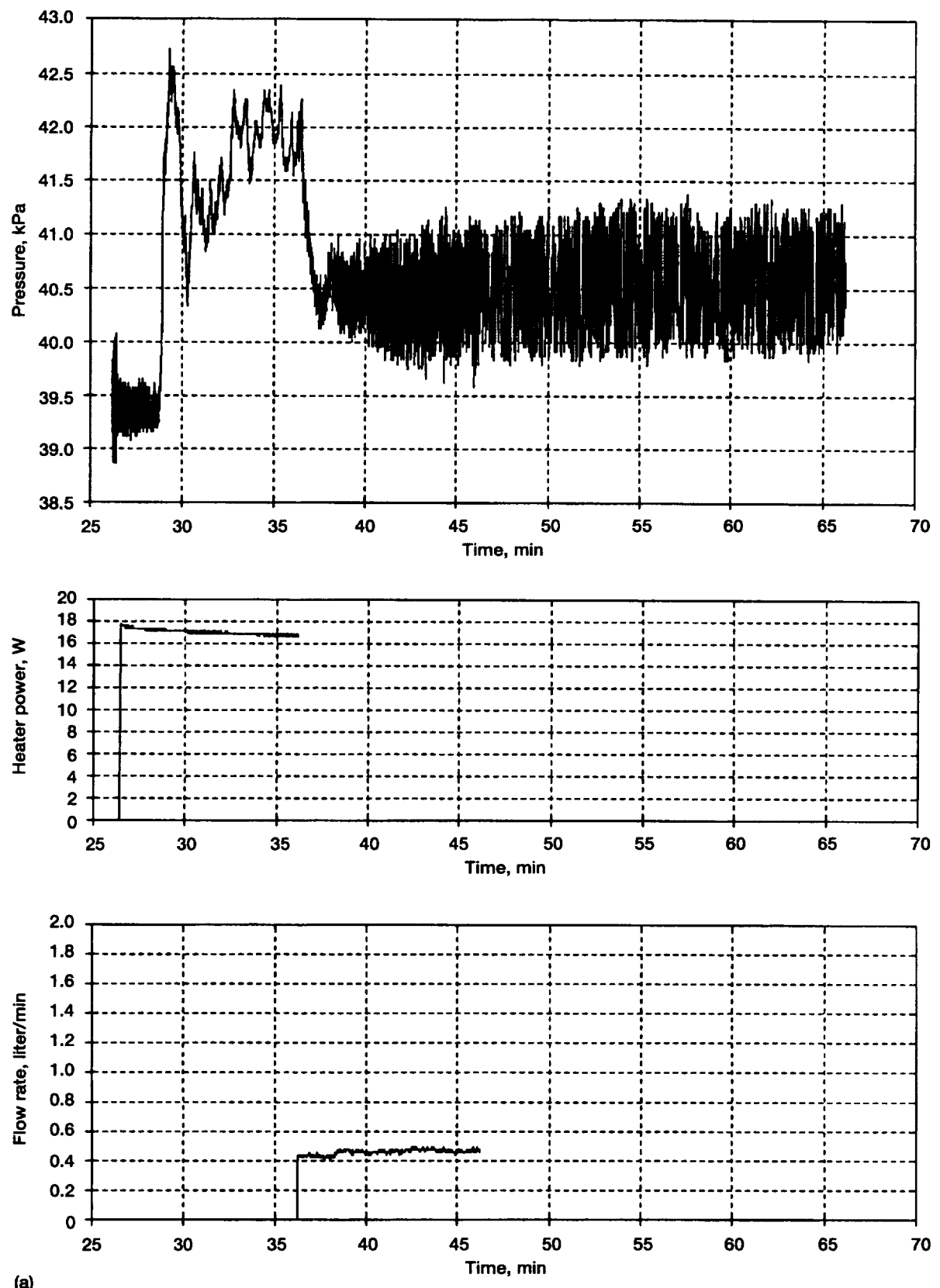
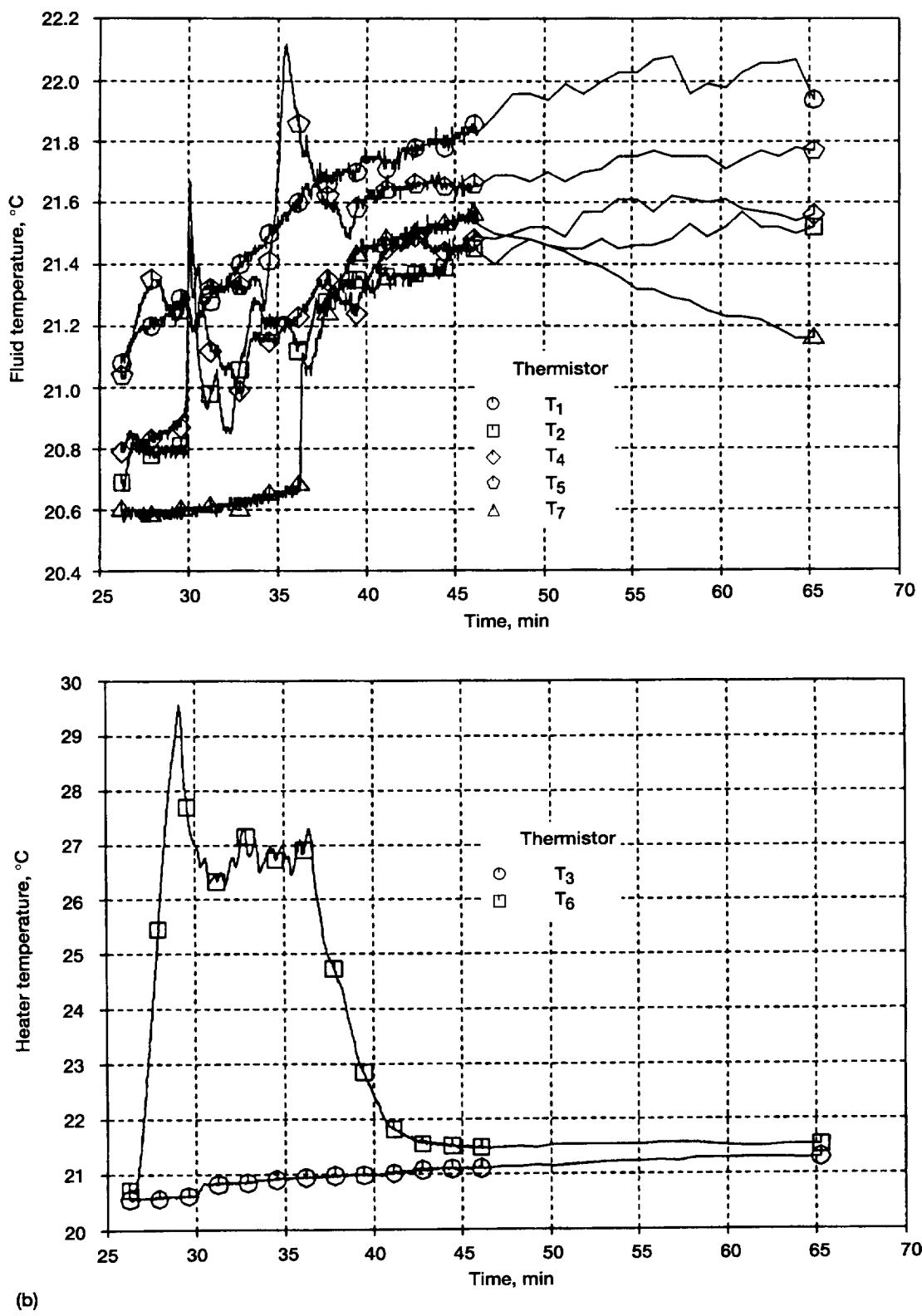


Figure A2.—Run 2. (a) Pressure, heater power, and flow rate. (b) Fluid and heater temperatures. (c) Accelerations.



(b)

Figure A2.—Continued. (b) Fluid and heater temperatures.

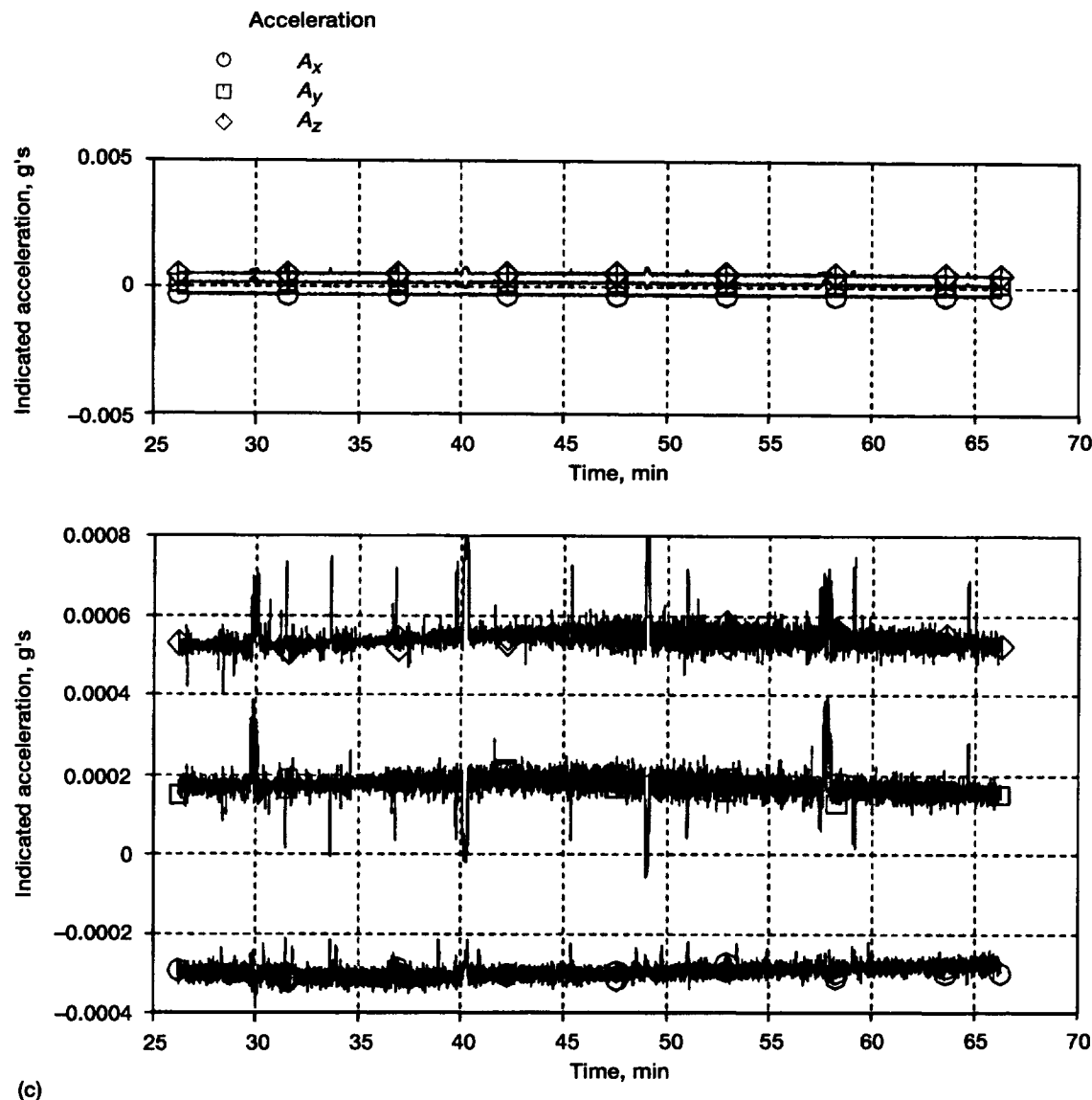
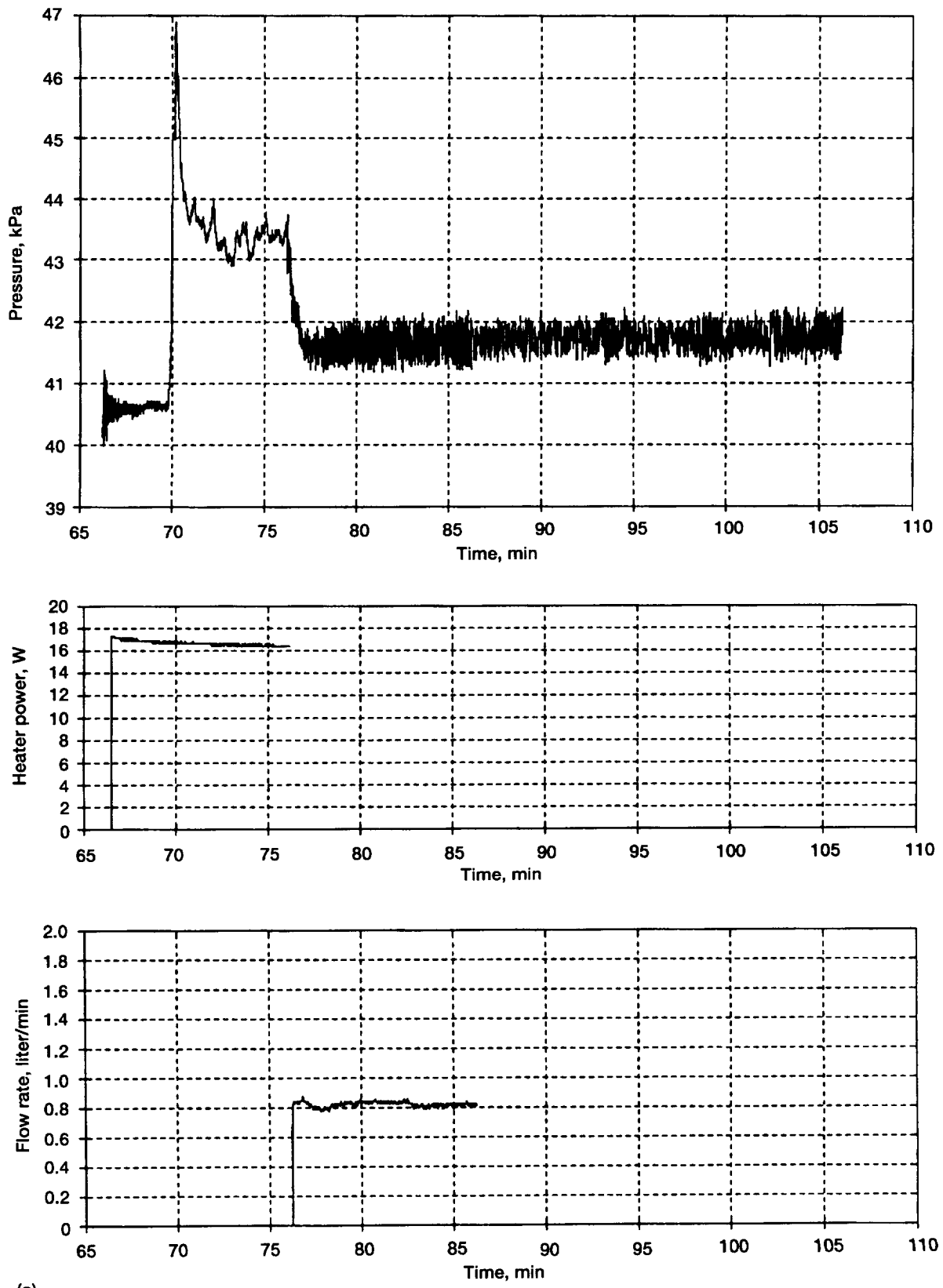


Figure A2.—Concluded. (c) Accelerations. (Bottom graph shows expanded scale.)



(a)

Figure A3.—Run 3. (a) Pressure, heater power, and flow rate. (b) Fluid and heater temperatures. (c) Accelerations.

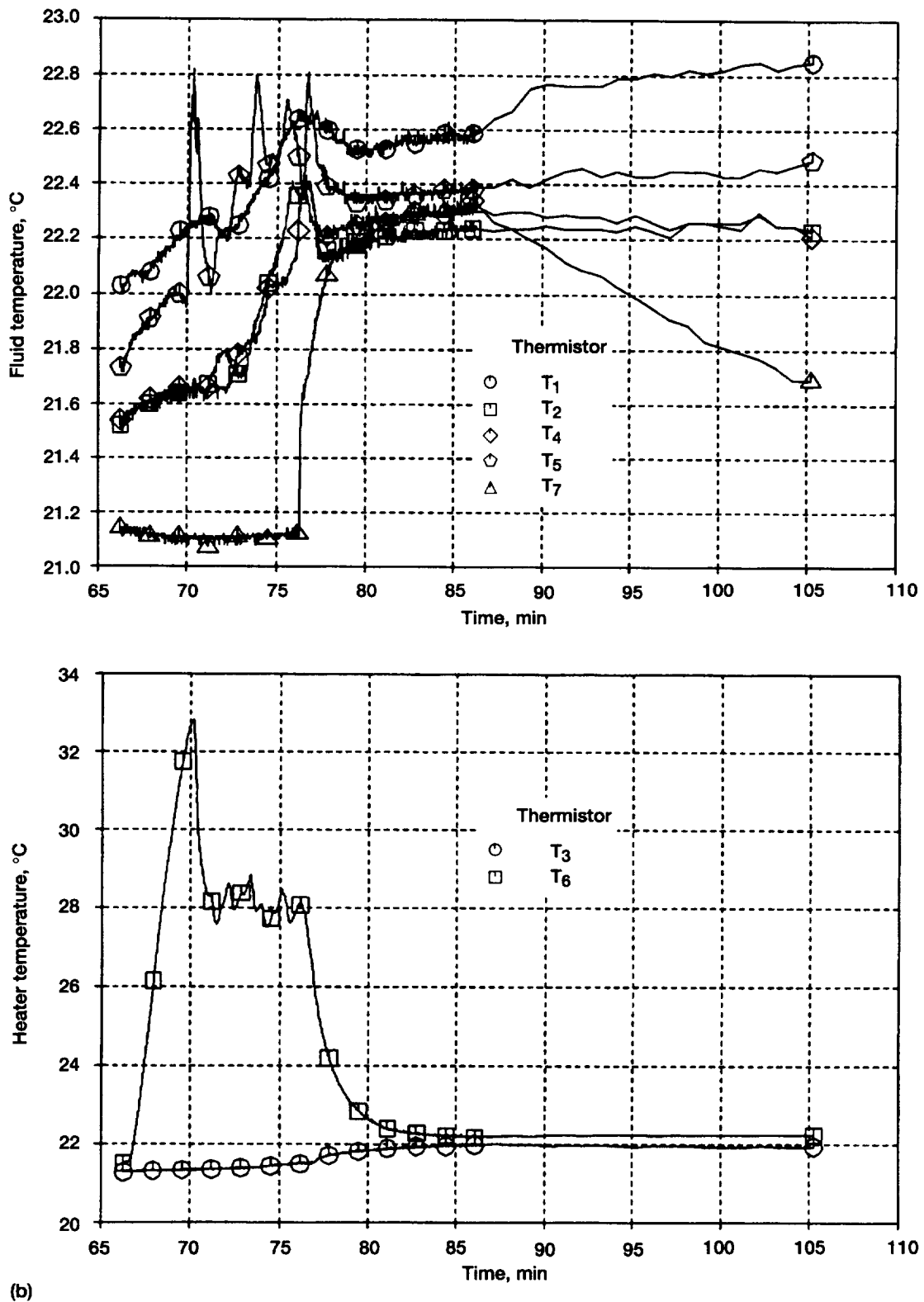


Figure A3.—Continued. (b) Fluid and heater temperatures.

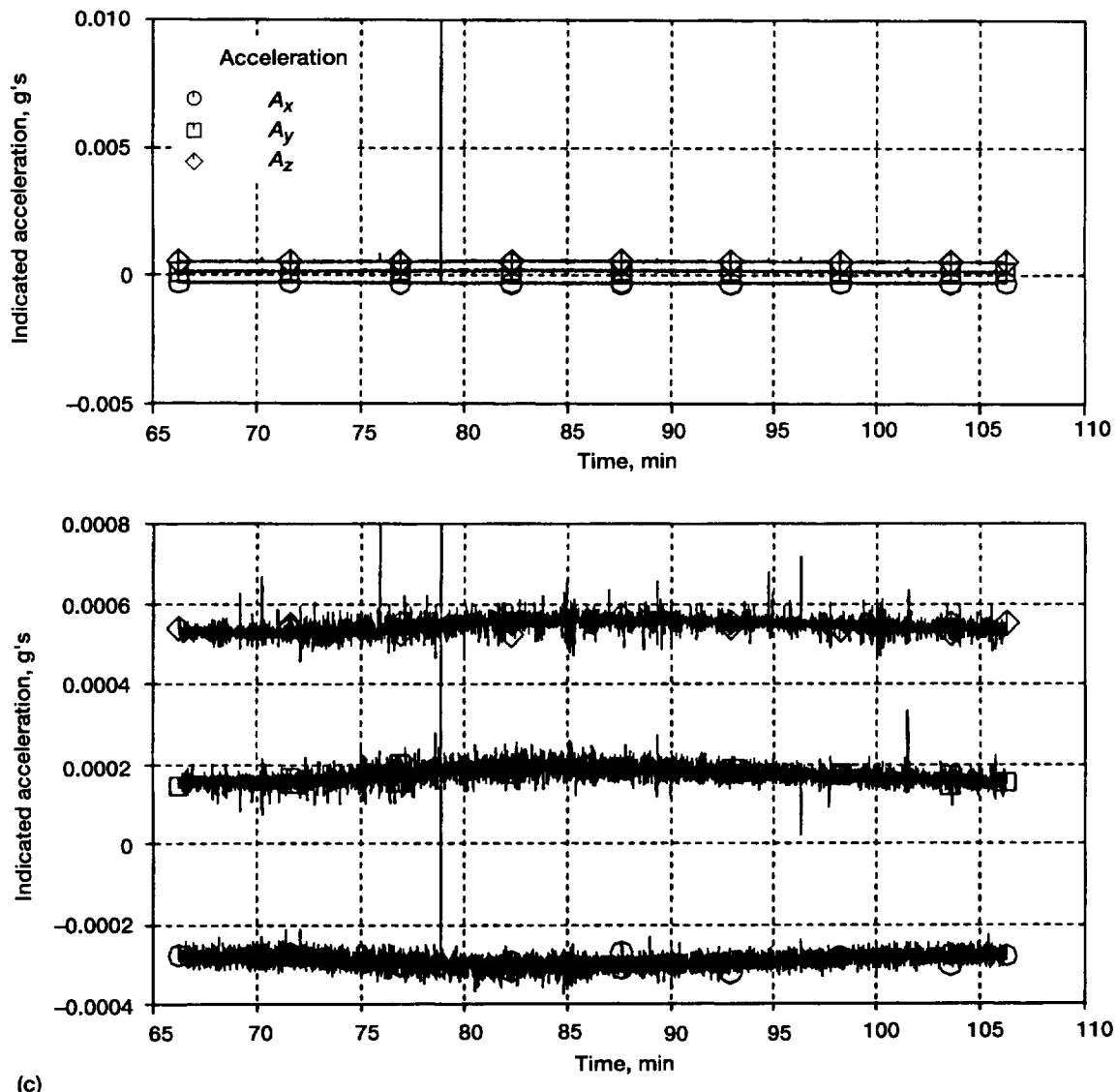
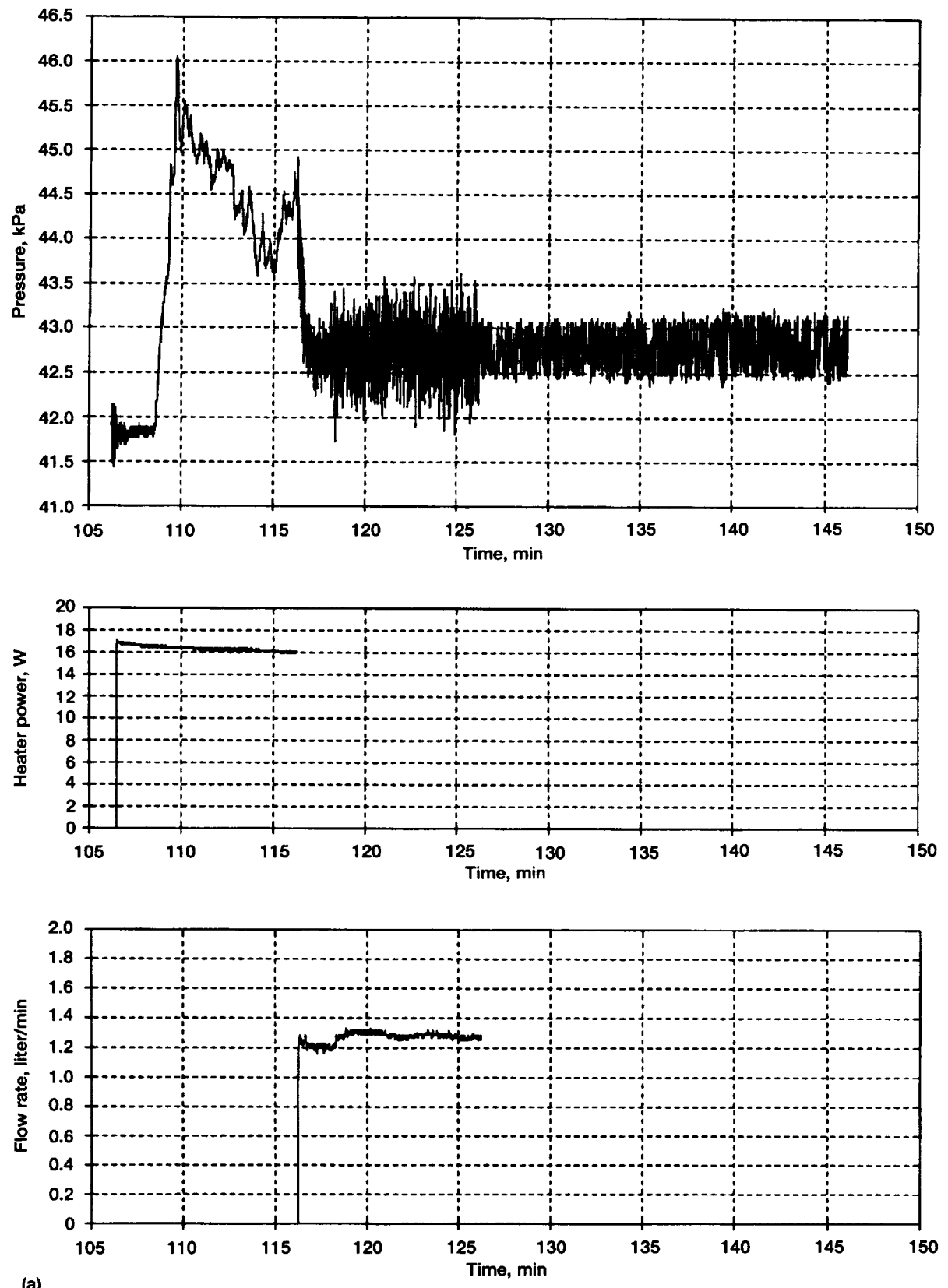


Figure A3.—Concluded. (c) Accelerations. (Bottom graph shows expanded scale.)



(a)

Figure A4.—Run 4. (a) Pressure, heater power, and flow rate. (b) Fluid and heater temperatures. (c) Accelerations.

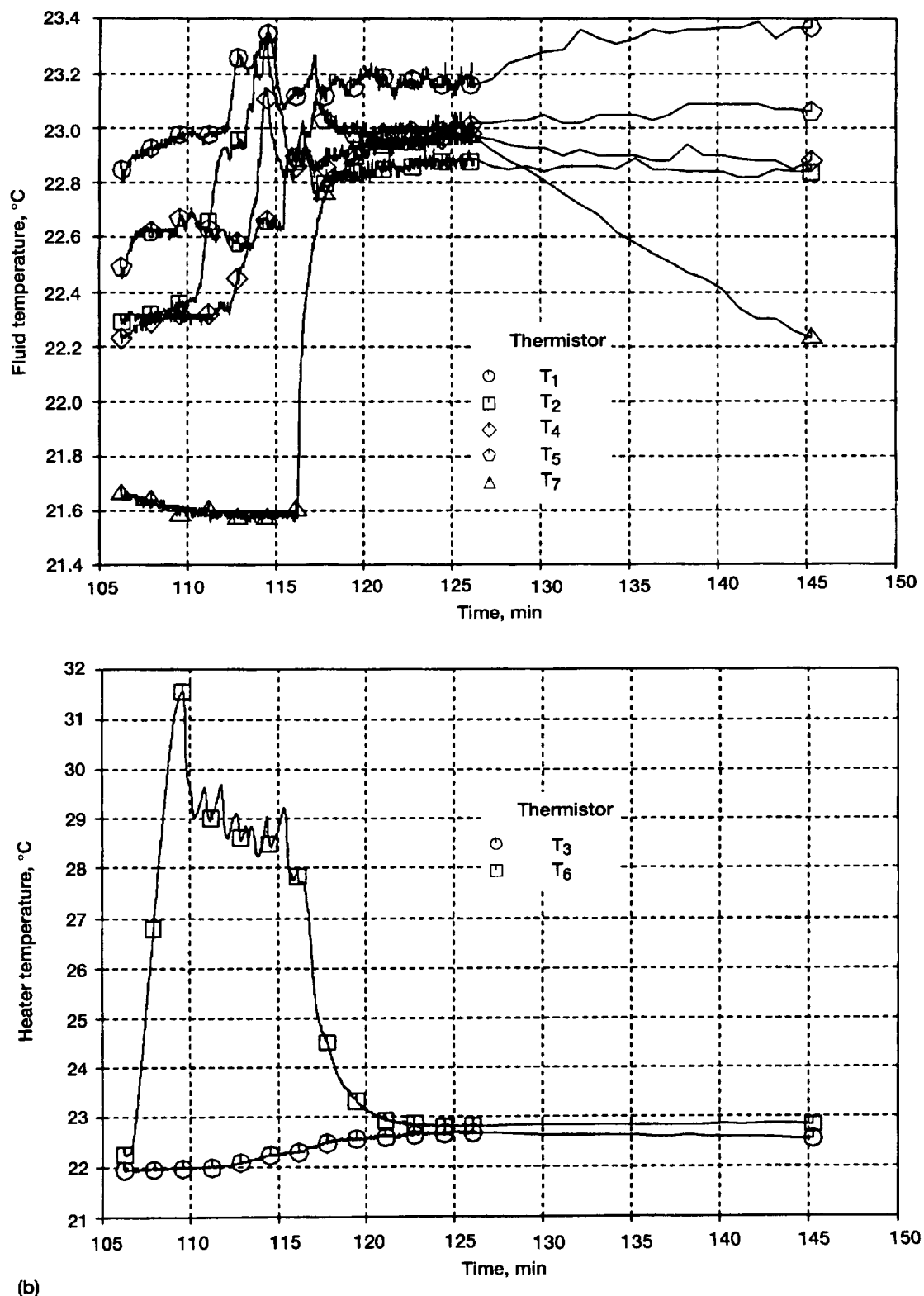


Figure A4.—Continued. (b) Fluid and heater temperatures.

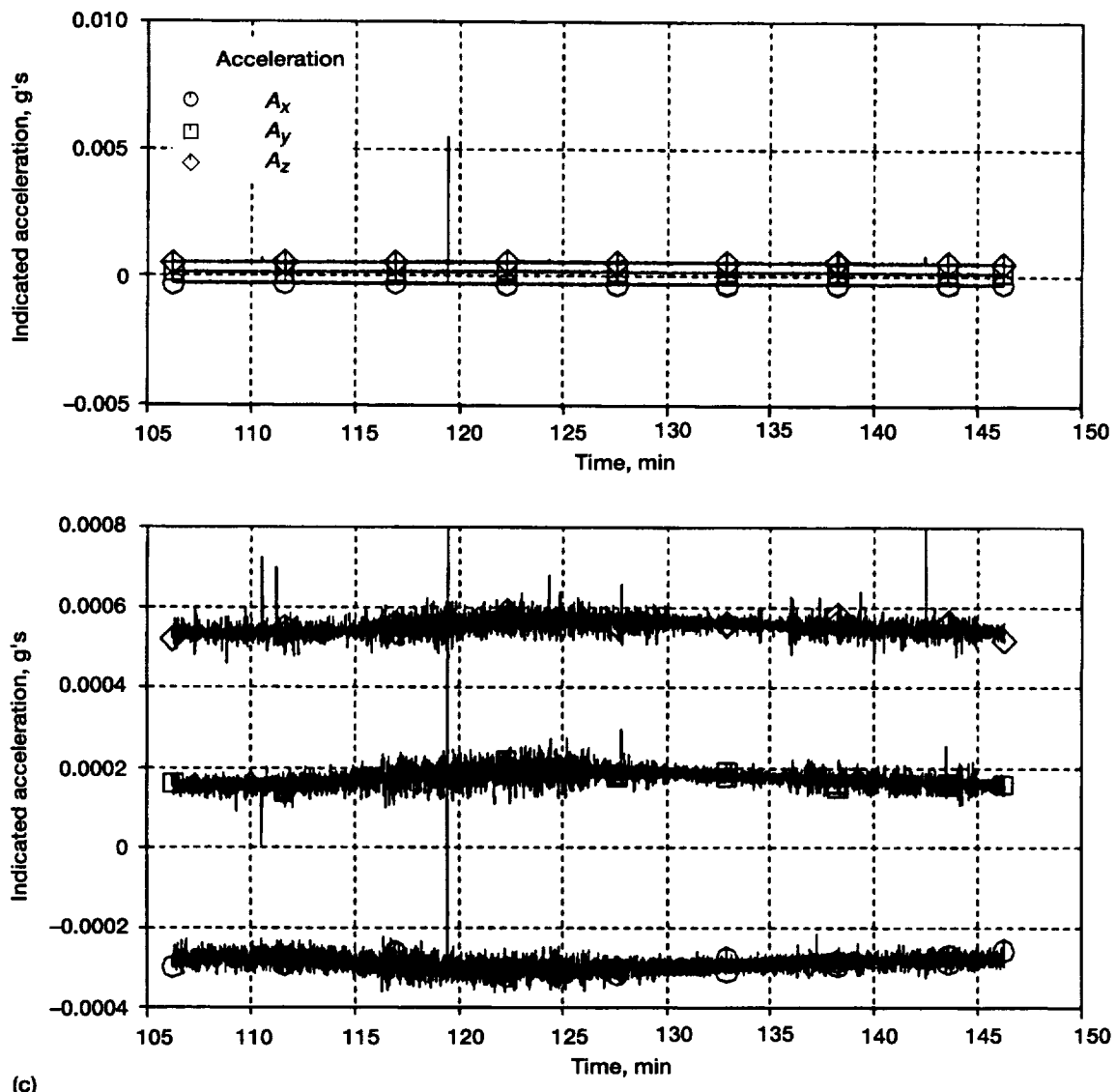
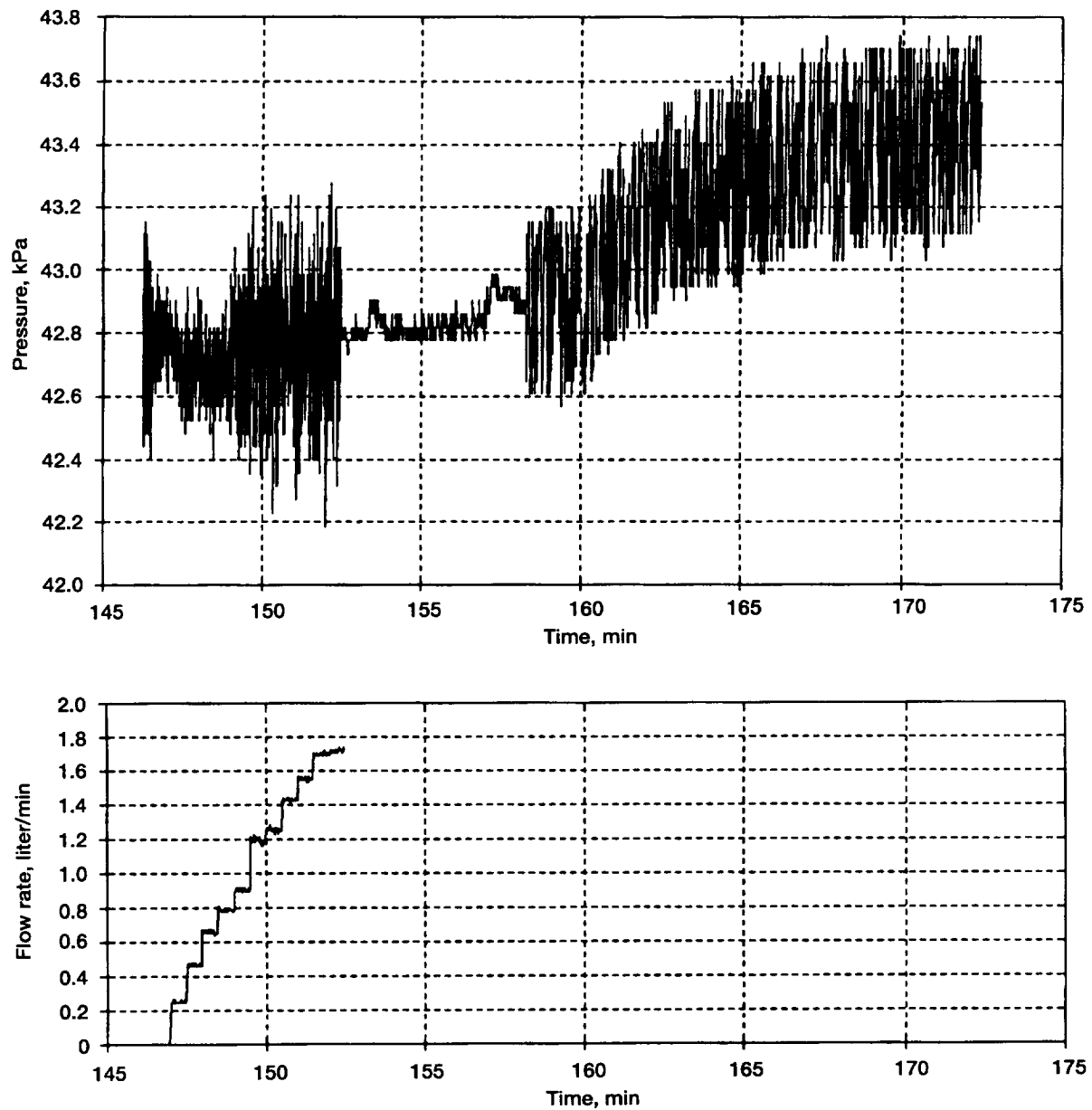


Figure A4.—Concluded. (c) Accelerations. (Bottom graph shows expanded scale.)



(a)

Figure A5.—Run 5. (a) Pressure and flow rate. (b) Fluid and heater temperatures. (c) Accelerations.

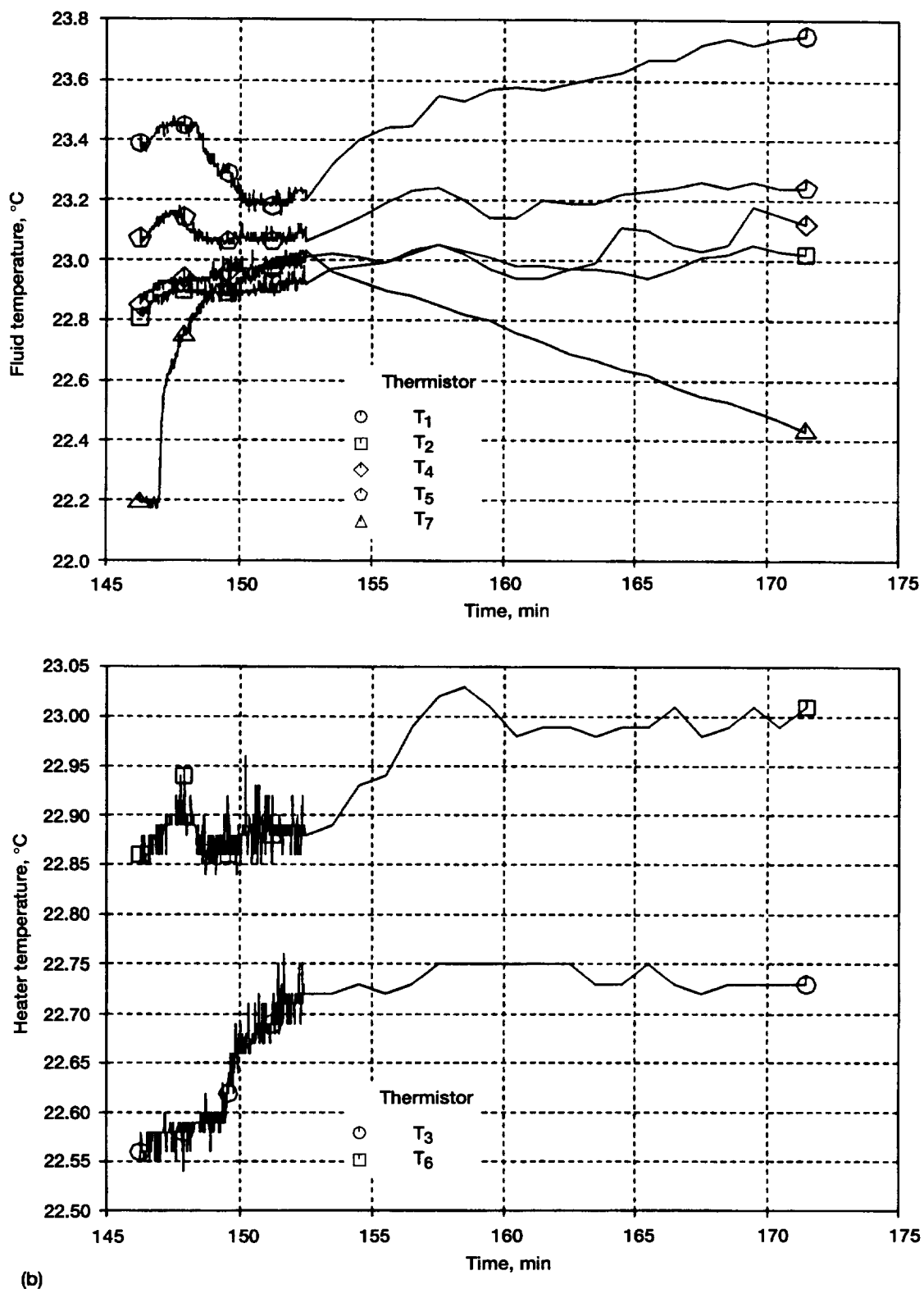


Figure A5.—Continued. (b) Fluid and heater temperatures.

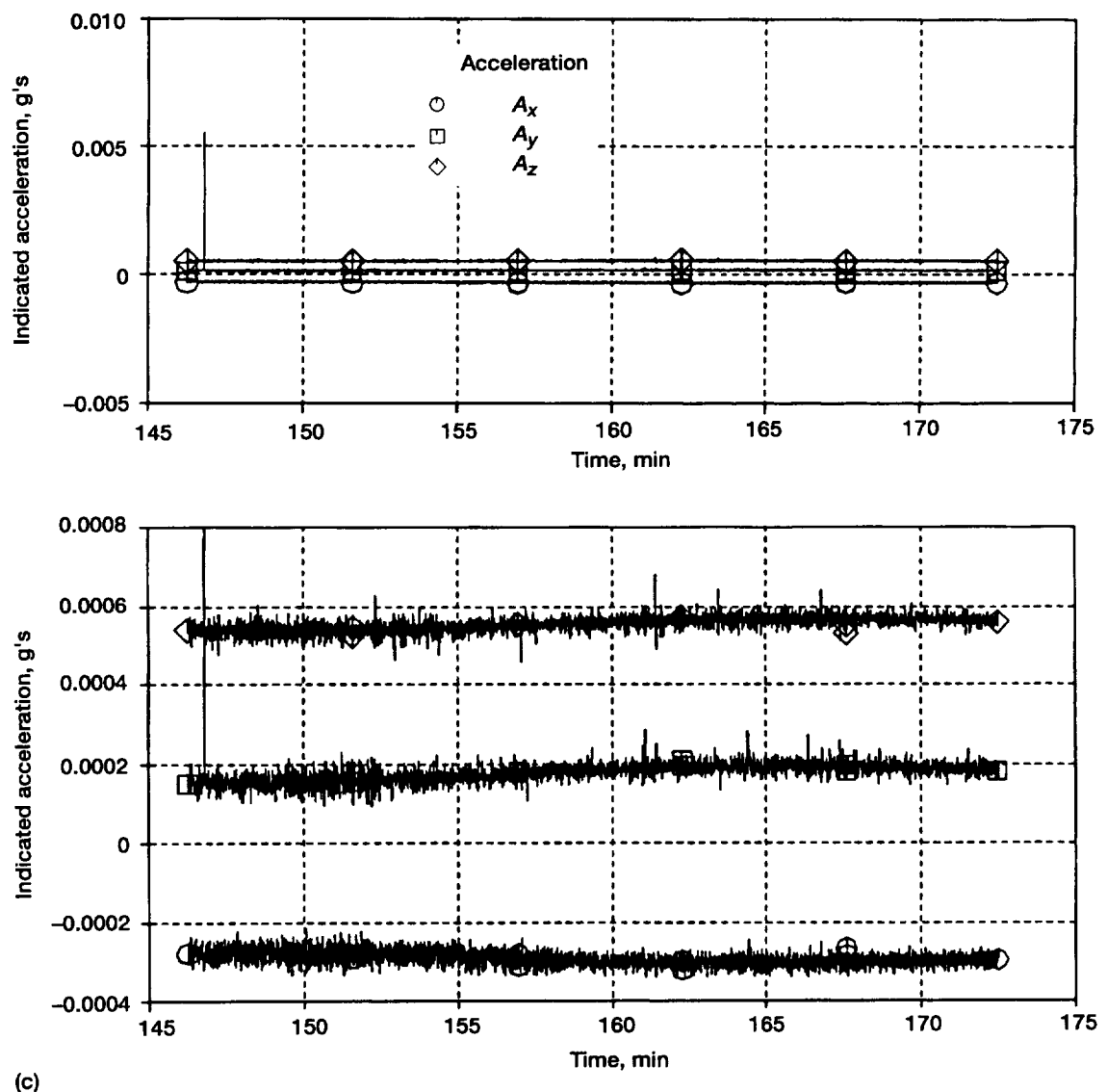
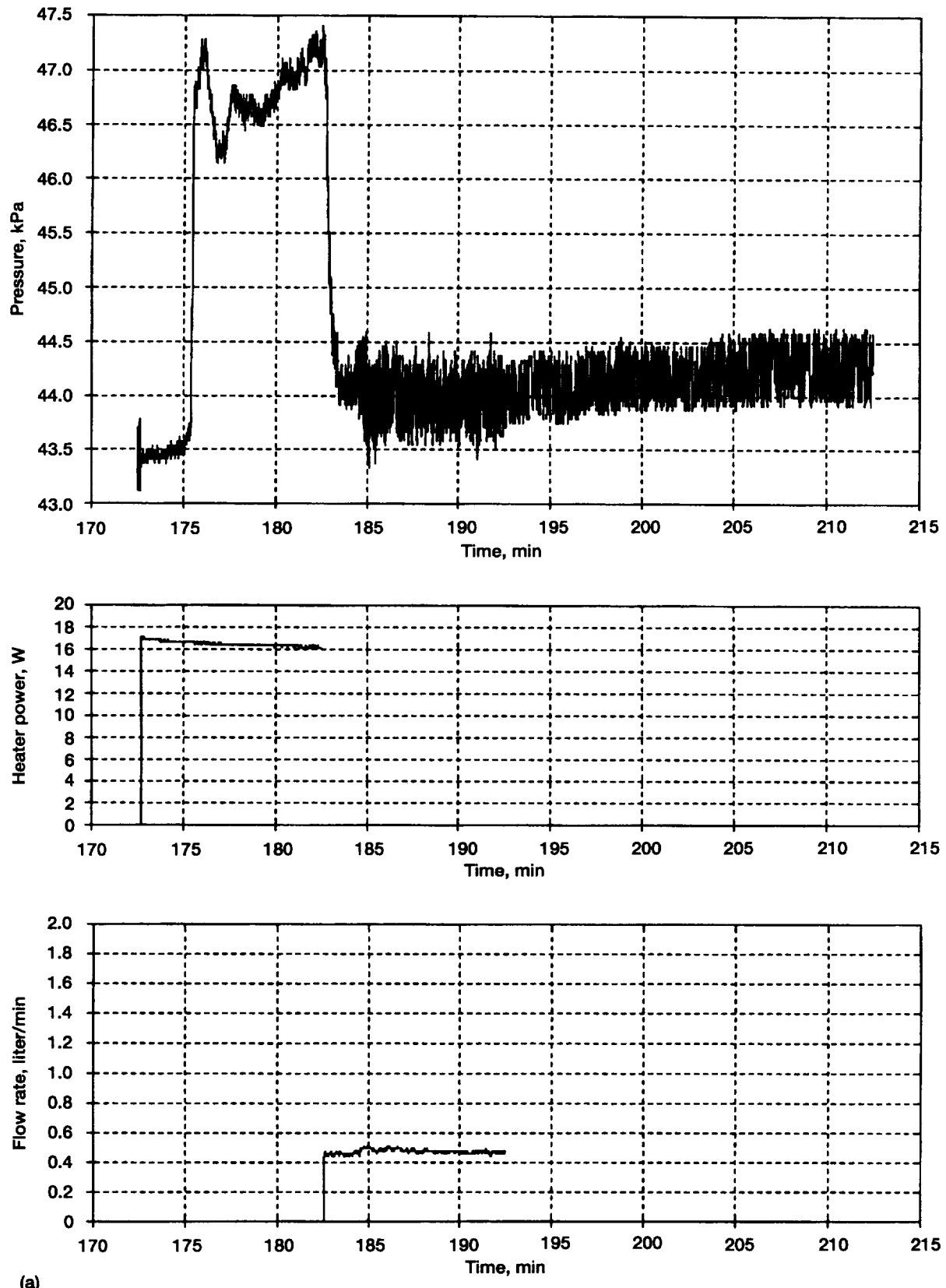
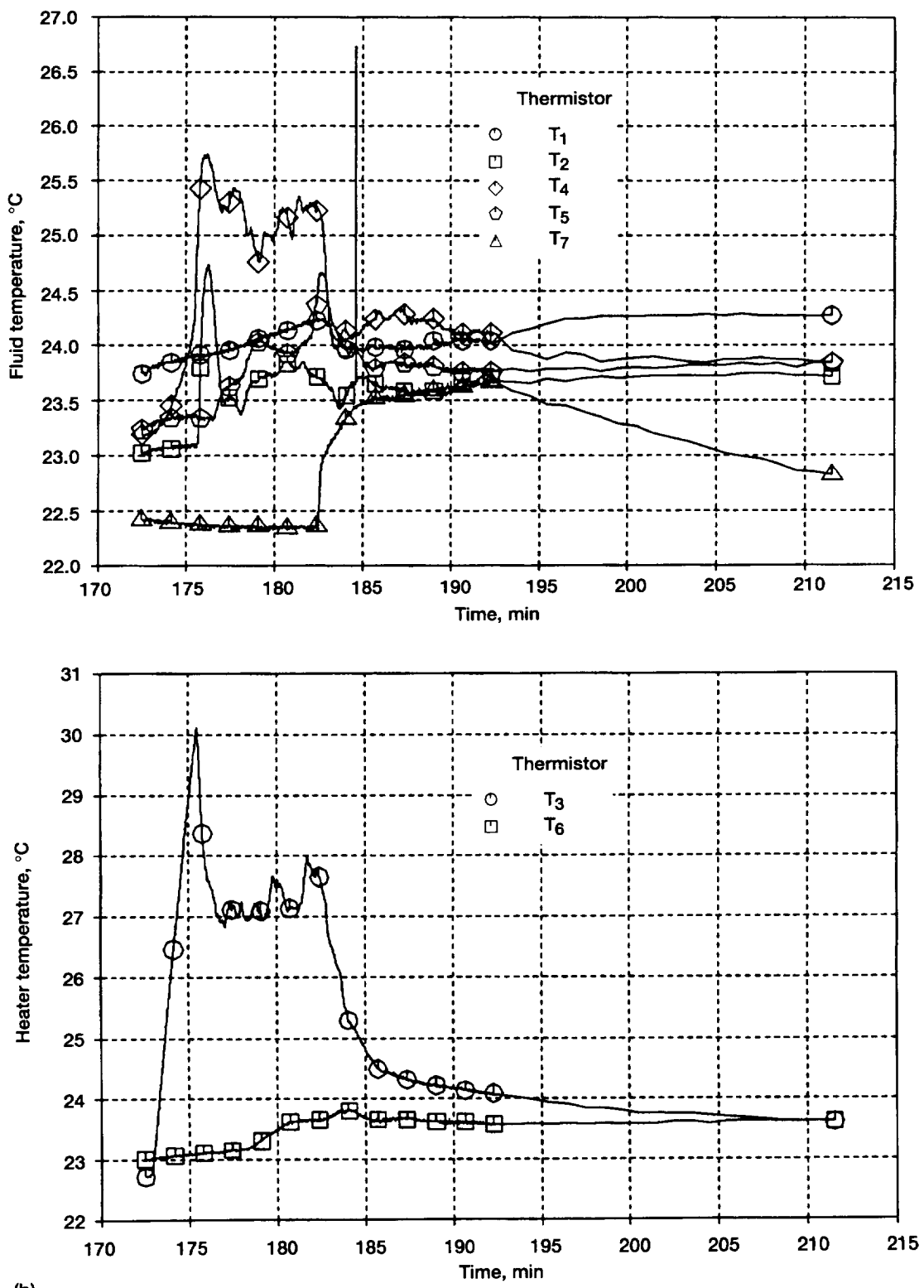


Figure A5.—Concluded. (c) Accelerations. (Bottom graph shows expanded scale.)



(a)

Figure A6.—Run 6. (a) Pressure, heater power, and flow rate. (b) Fluid and heater temperatures. (c) Accelerations.



(b)

Figure A6.—Continued. (b) Fluid and heater temperatures.

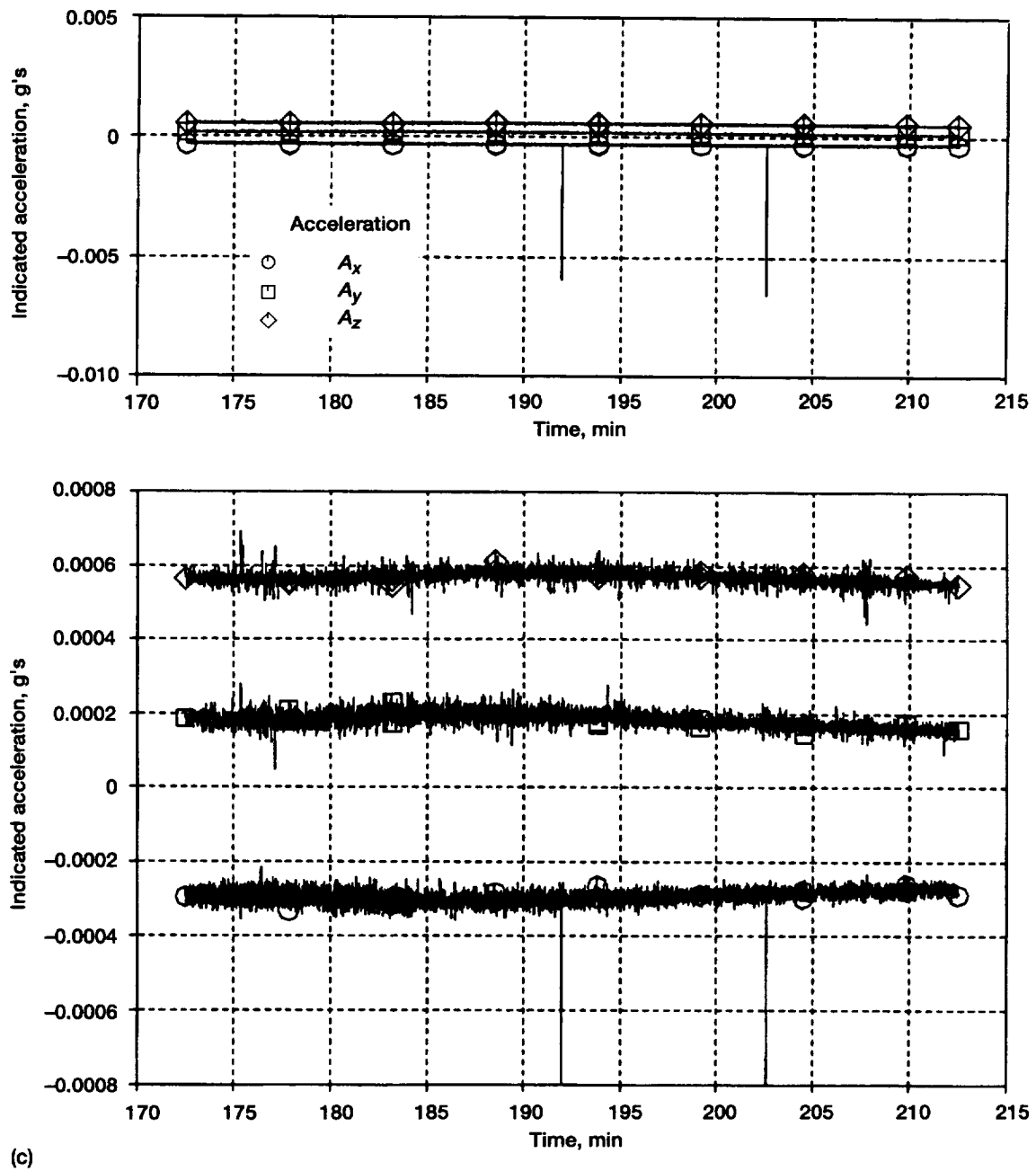
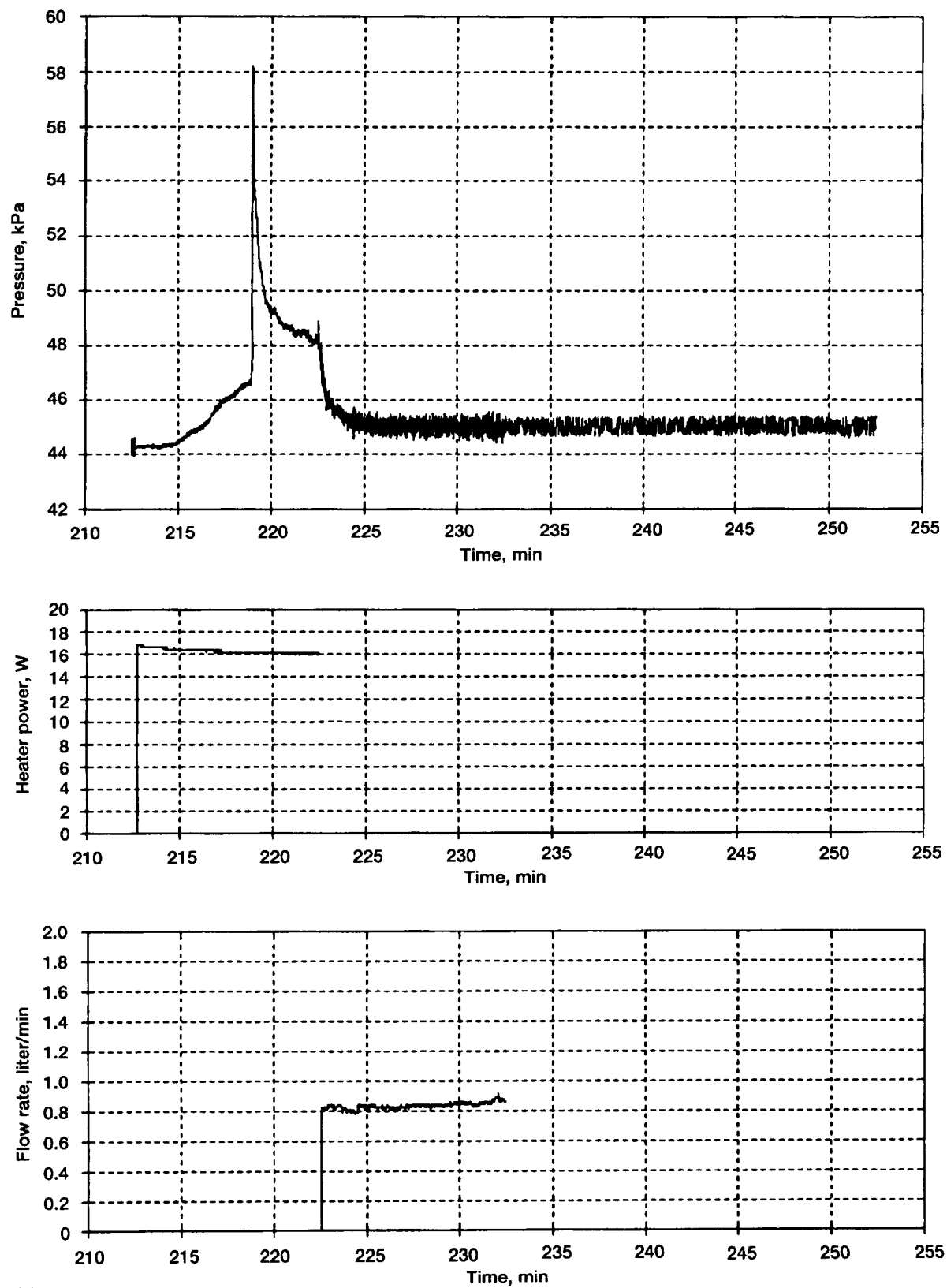
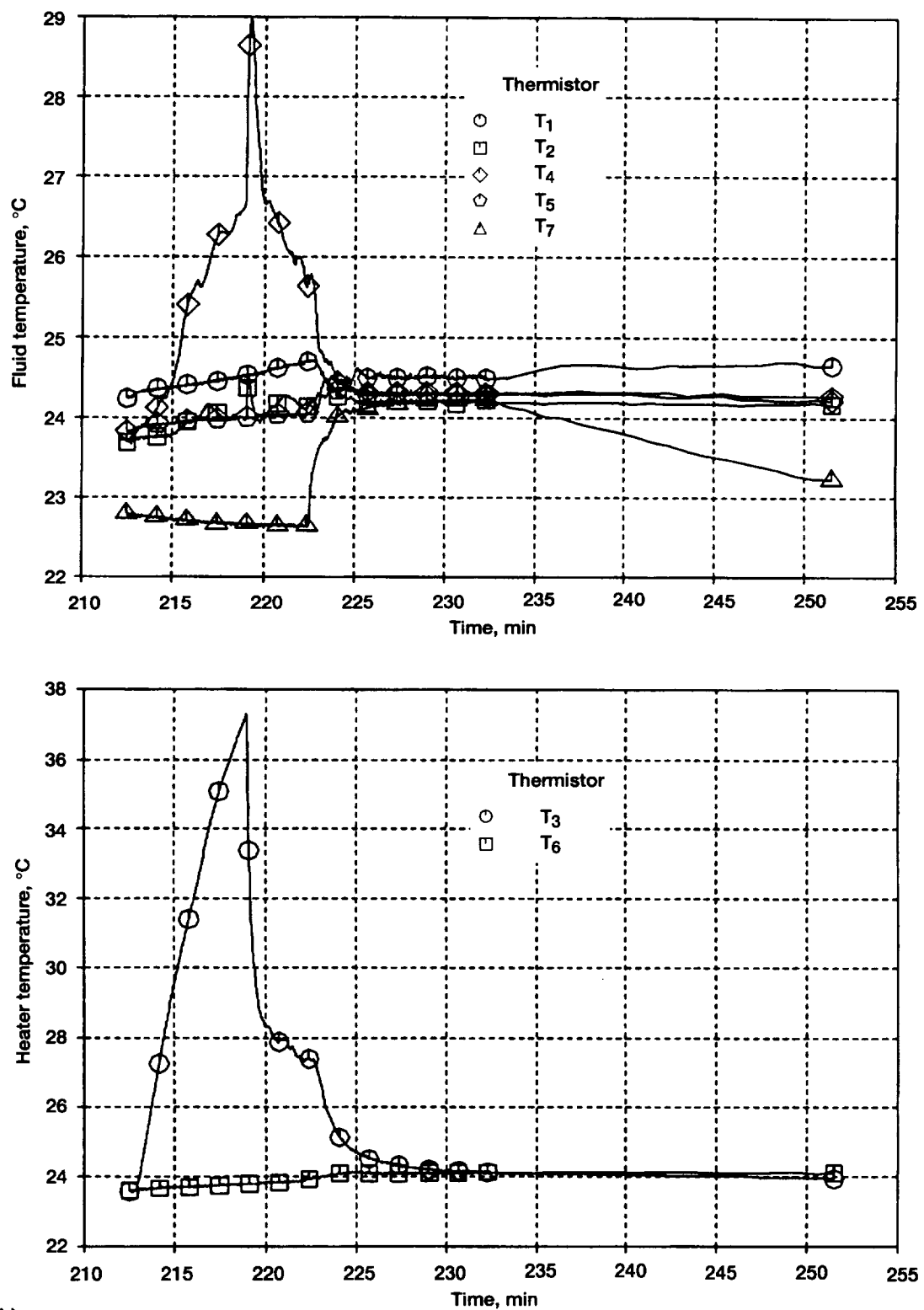


Figure A6.—Concluded. (c) Accelerations.



(a)

Figure A7.—Run 7. (a) Pressure, heater power, and flow rate. (b) Fluid and heater temperatures. (c) Accelerations.



(b)

Figure A7.—Continued. (b) Fluid and heater temperatures.

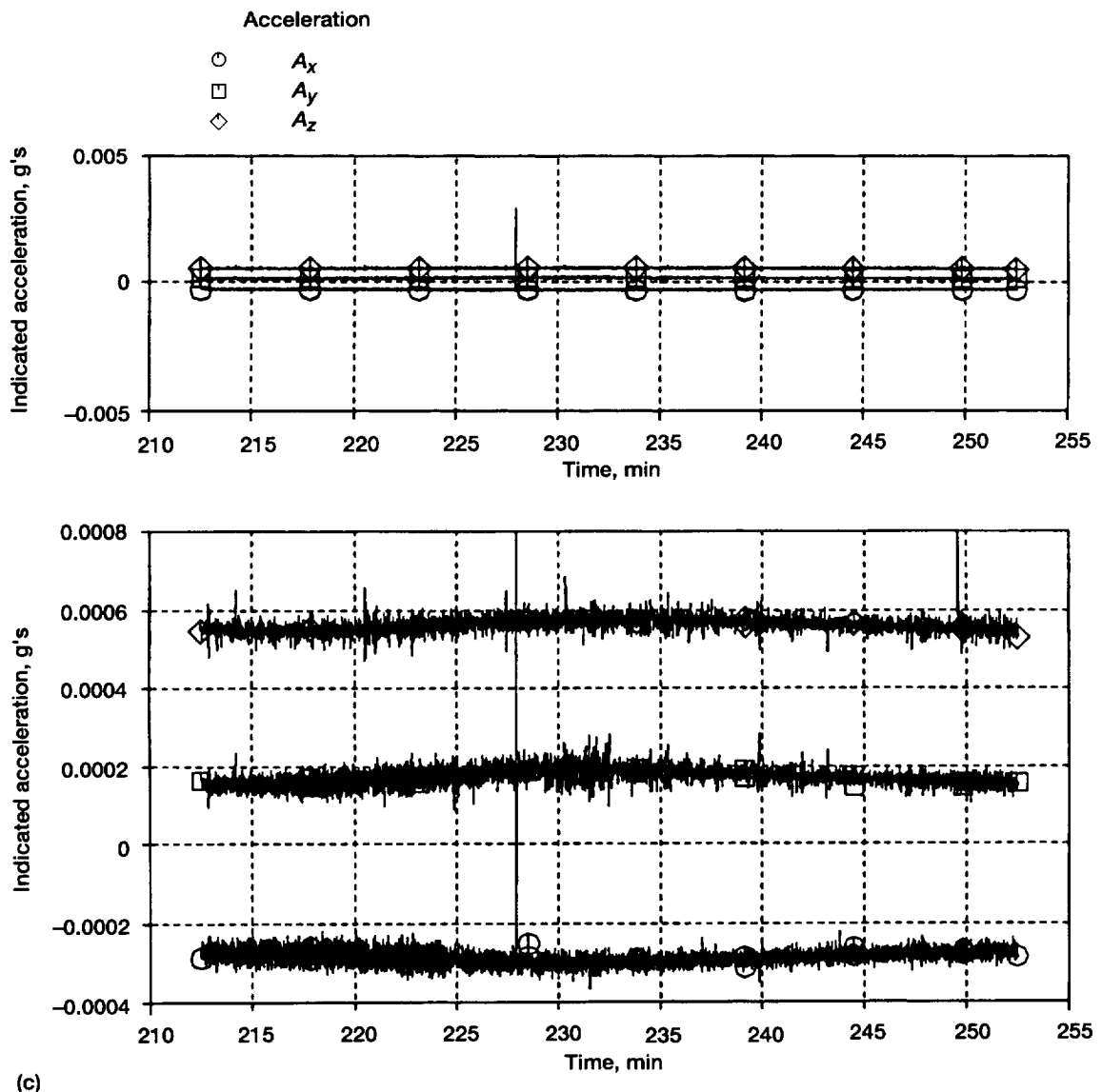


Figure A7.—Concluded. (c) Accelerations. (Bottom graph shows expanded scale.)

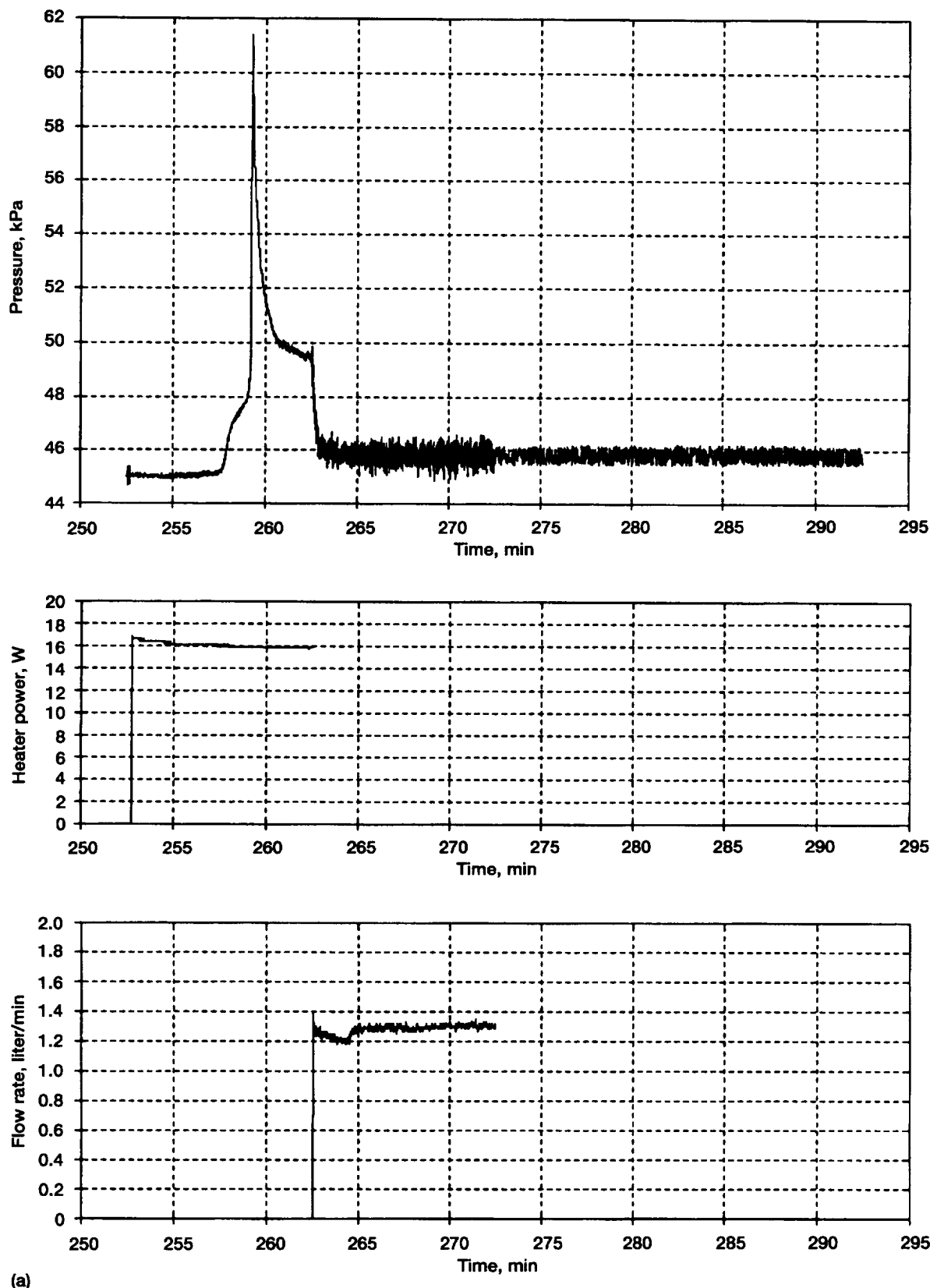
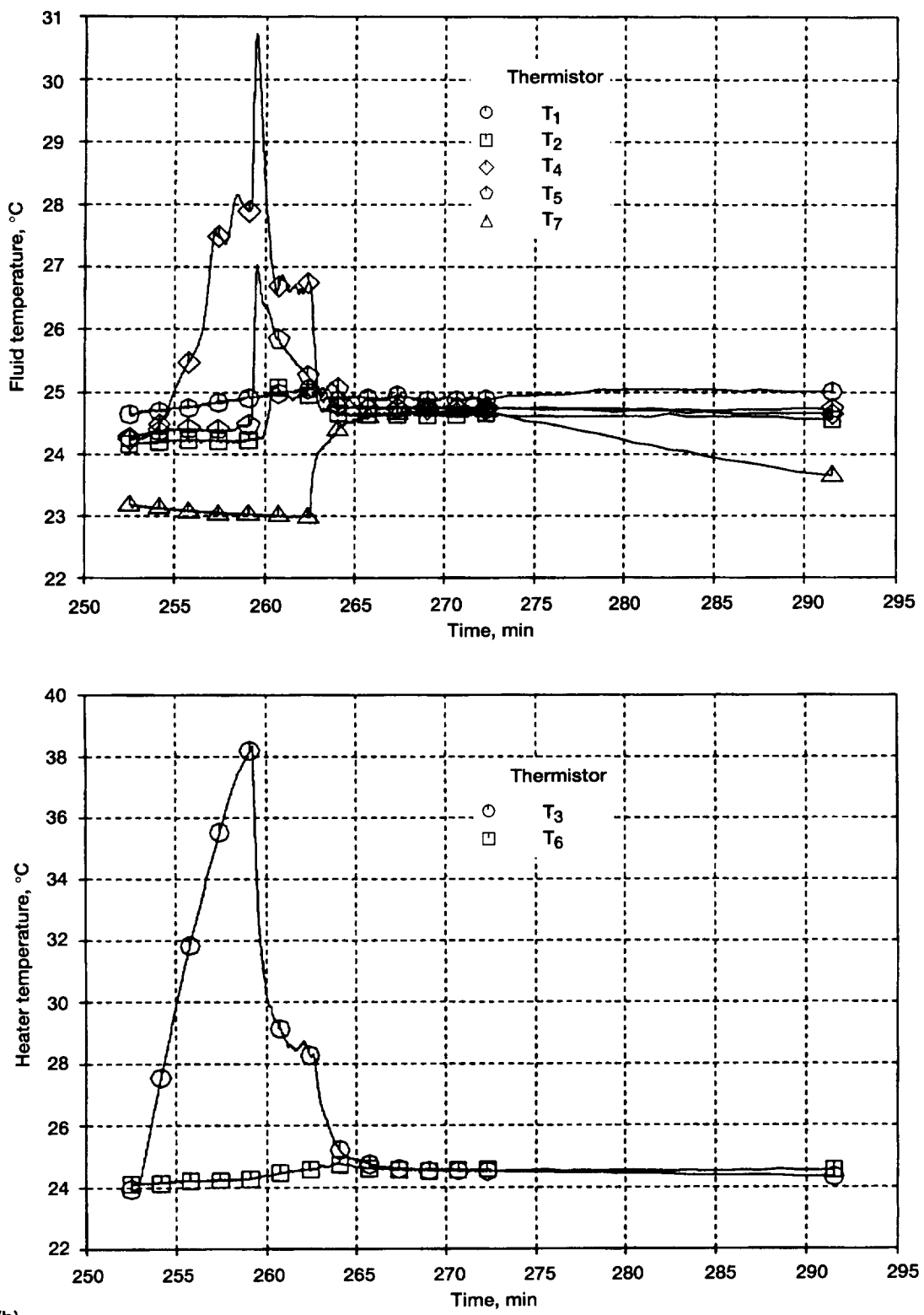


Figure A8.—Run 8. (a) Pressure, heater power, and flow rate. (b) Fluid and heater temperatures. (c) Accelerations.



(b)

Figure A8.—Continued. (b) Fluid and heater temperatures.

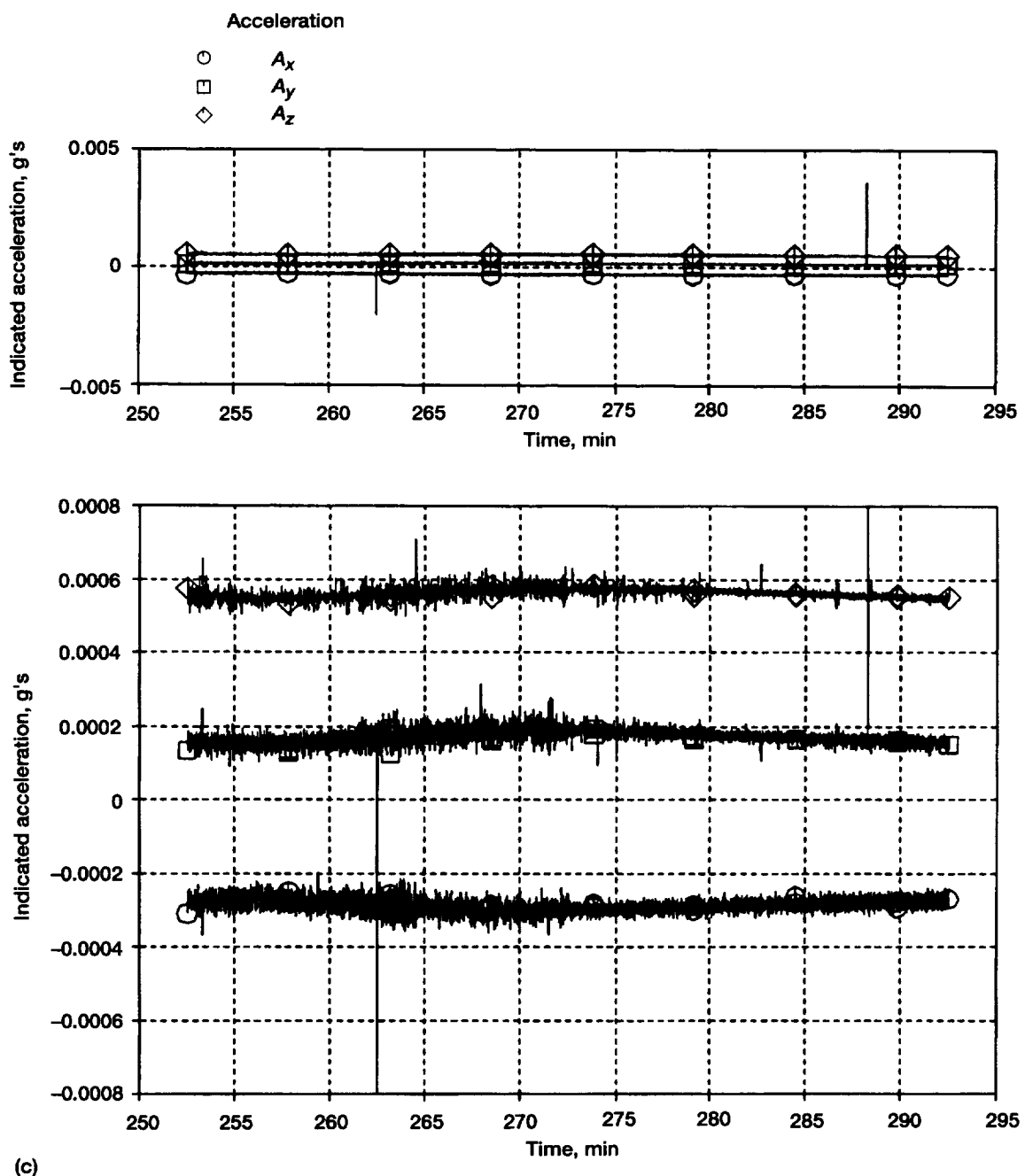
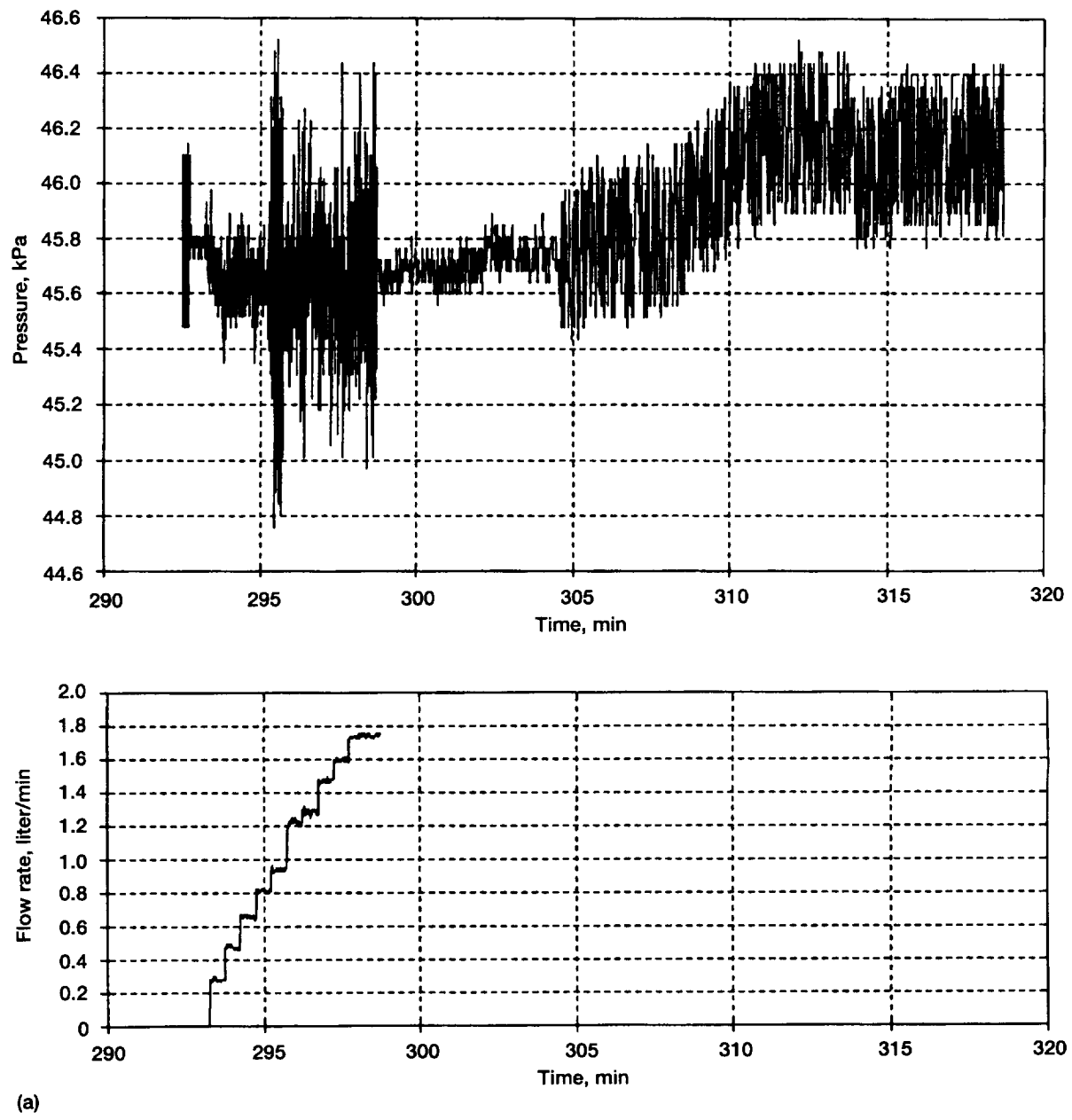
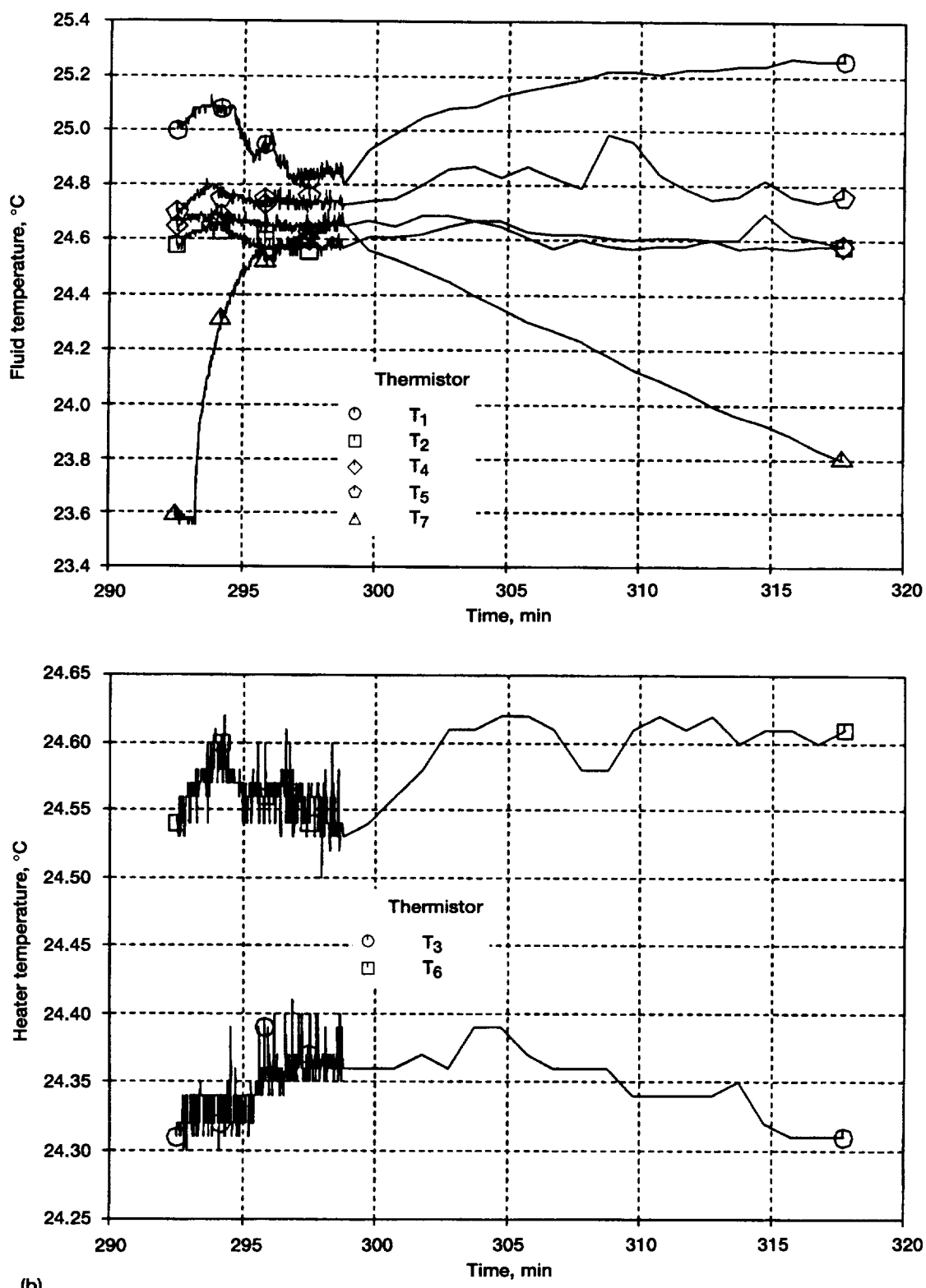


Figure A8.—Concluded. (c) Accelerations. (Bottom graph shows expanded scale.)



(a)

Figure A9.—Run 9. (a) Pressure and flow rate. (b) Fluid and heater temperatures. (c) Accelerations.



(b)

Figure A9.—Continued. (b) Fluid and heater temperatures.

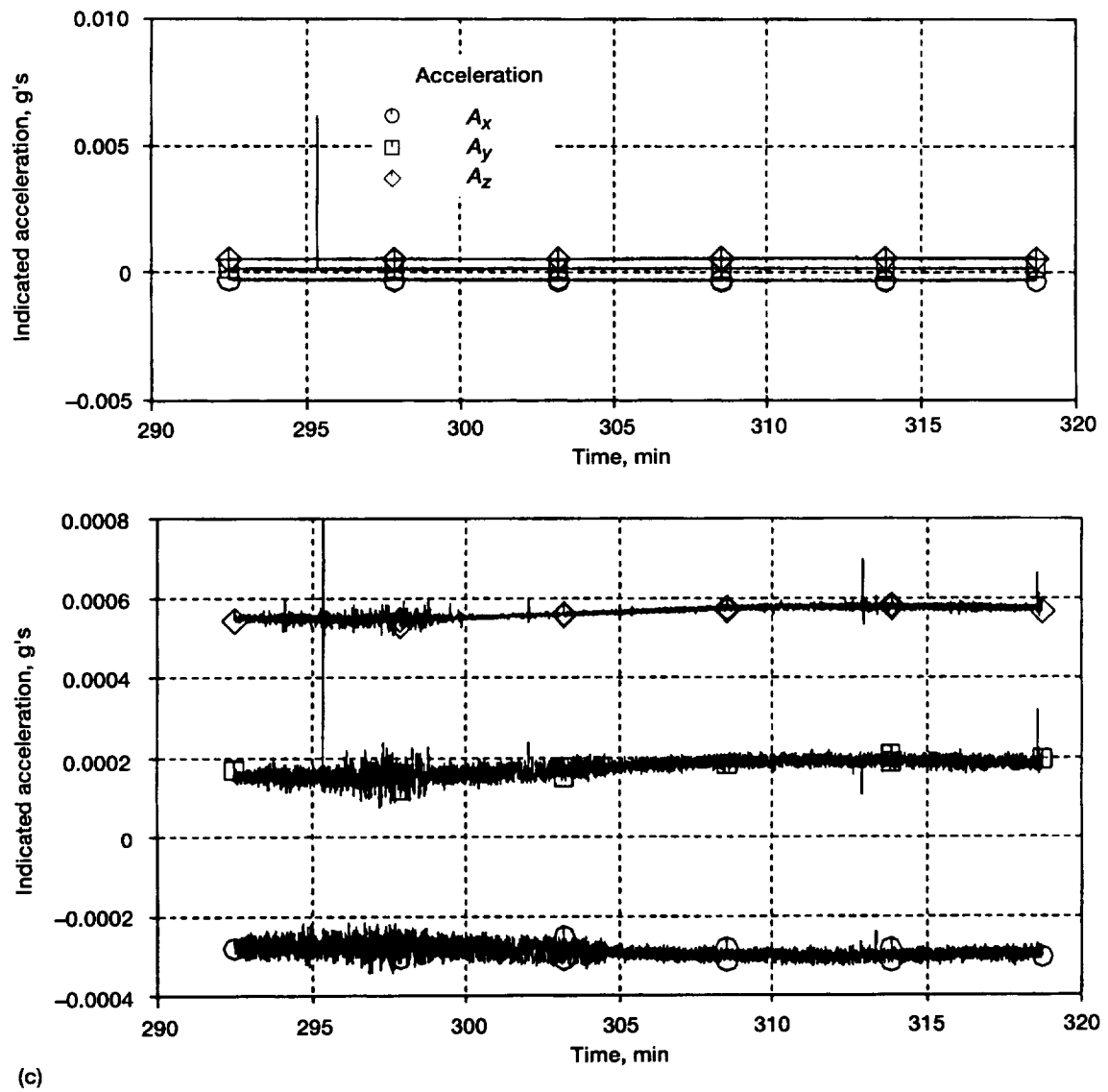


Figure A9.—Concluded. (c) Accelerations. (Bottom graph shows expanded scale.)

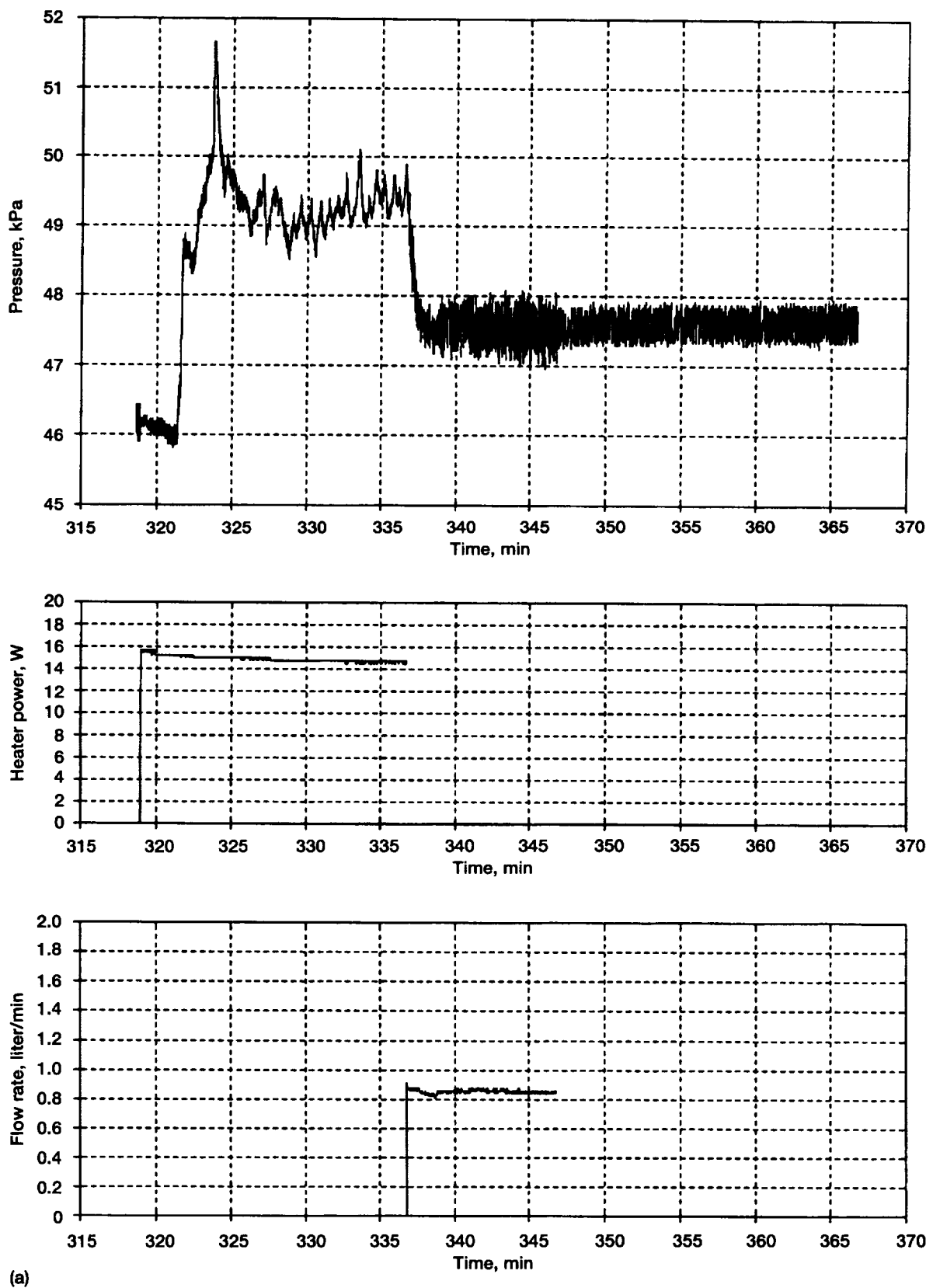
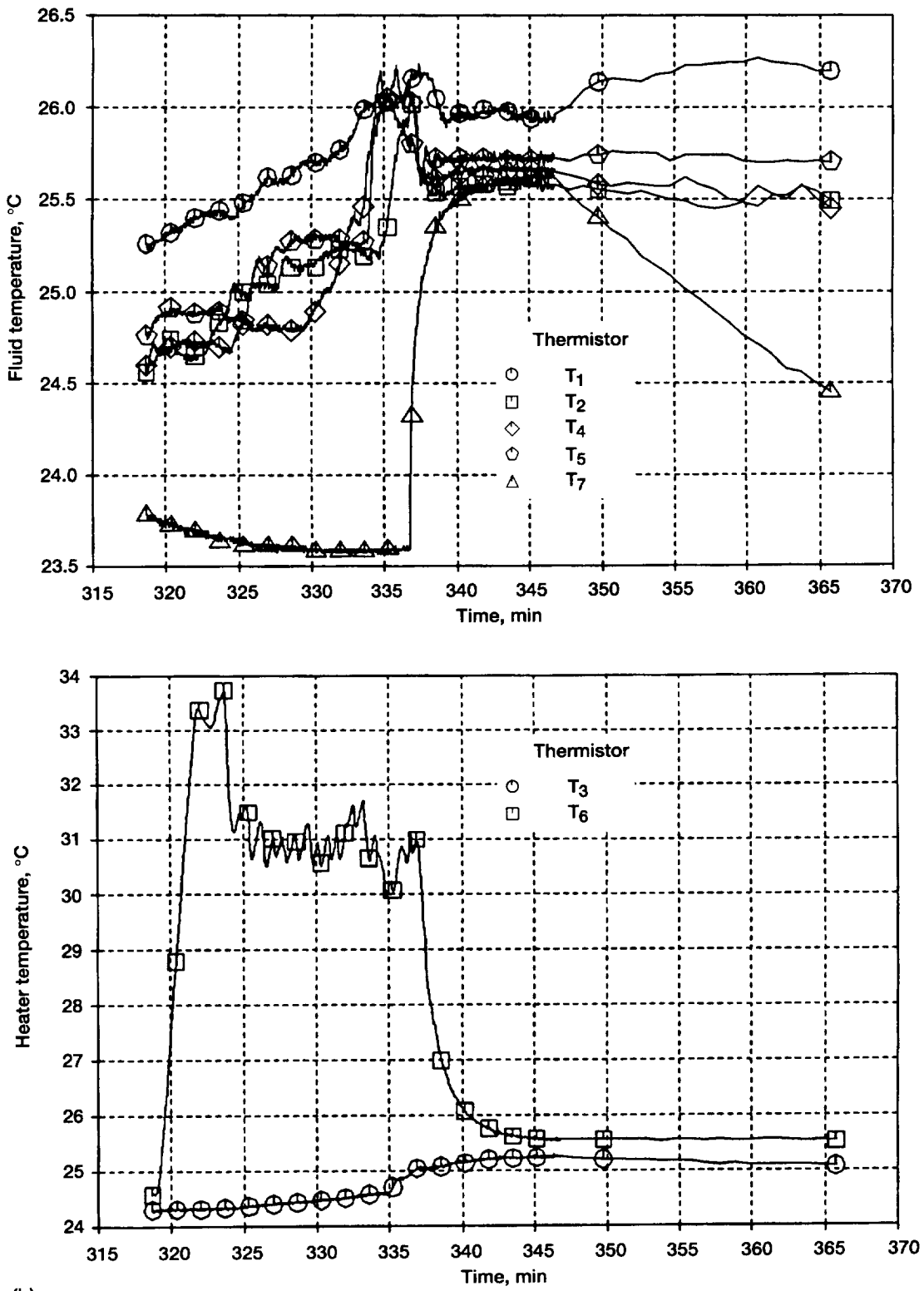


Figure A10.—Run 10. (a) Pressure, heater power, and flow rate. (b) Fluid and heater temperatures.
(c) Accelerations.



(b)

Figure A10.—Continued. (b) Fluid and heater temperatures.

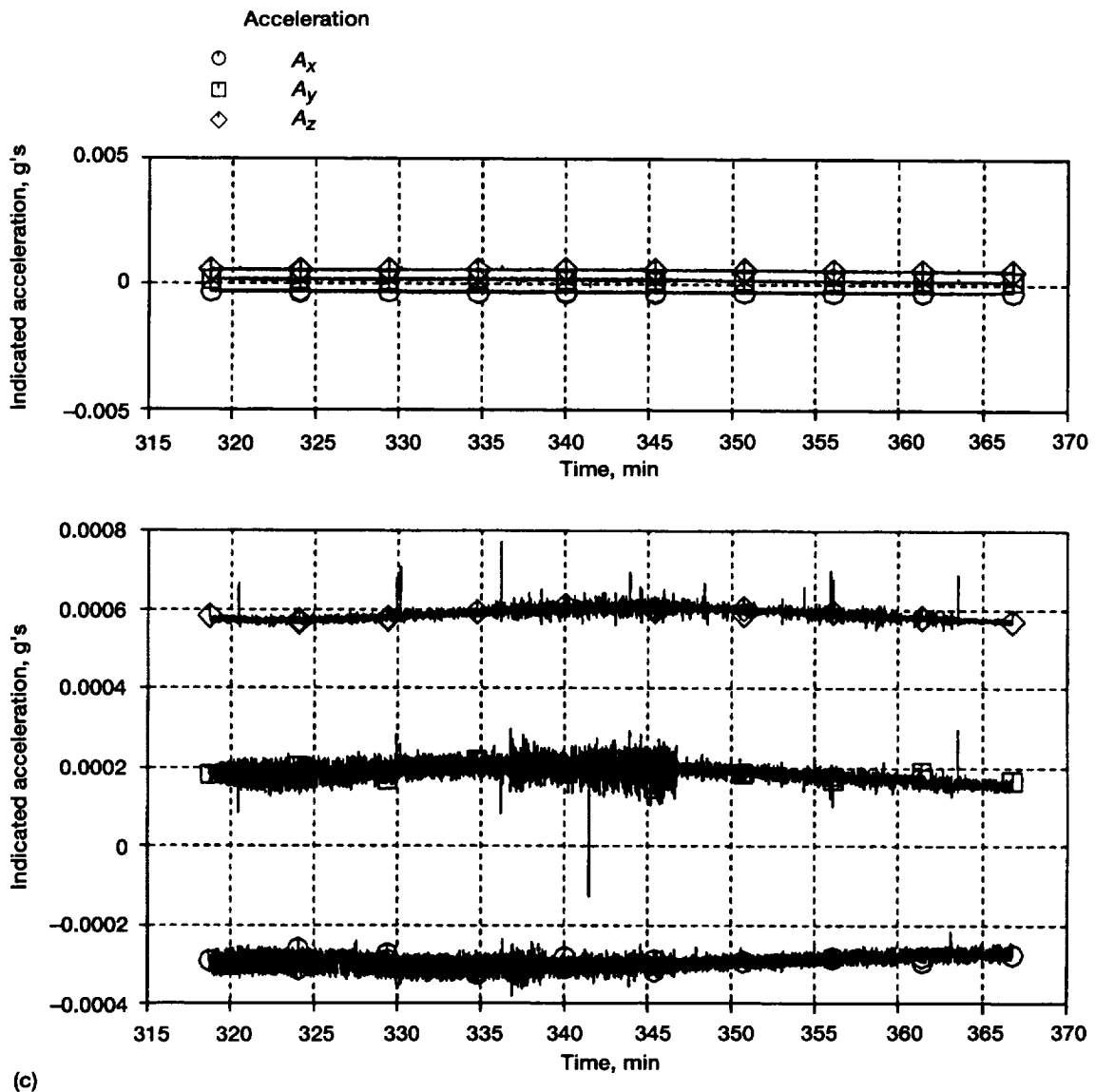
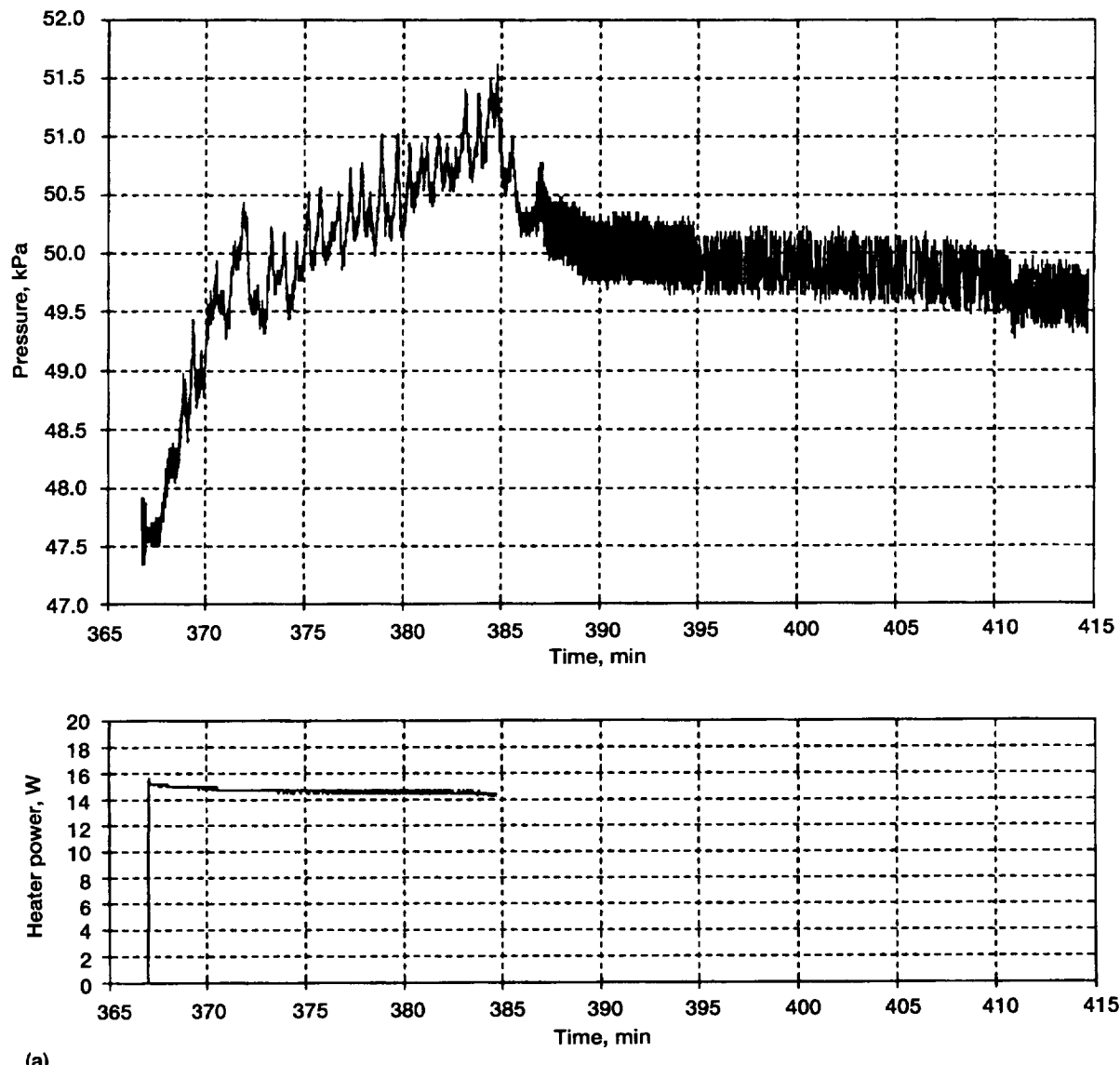
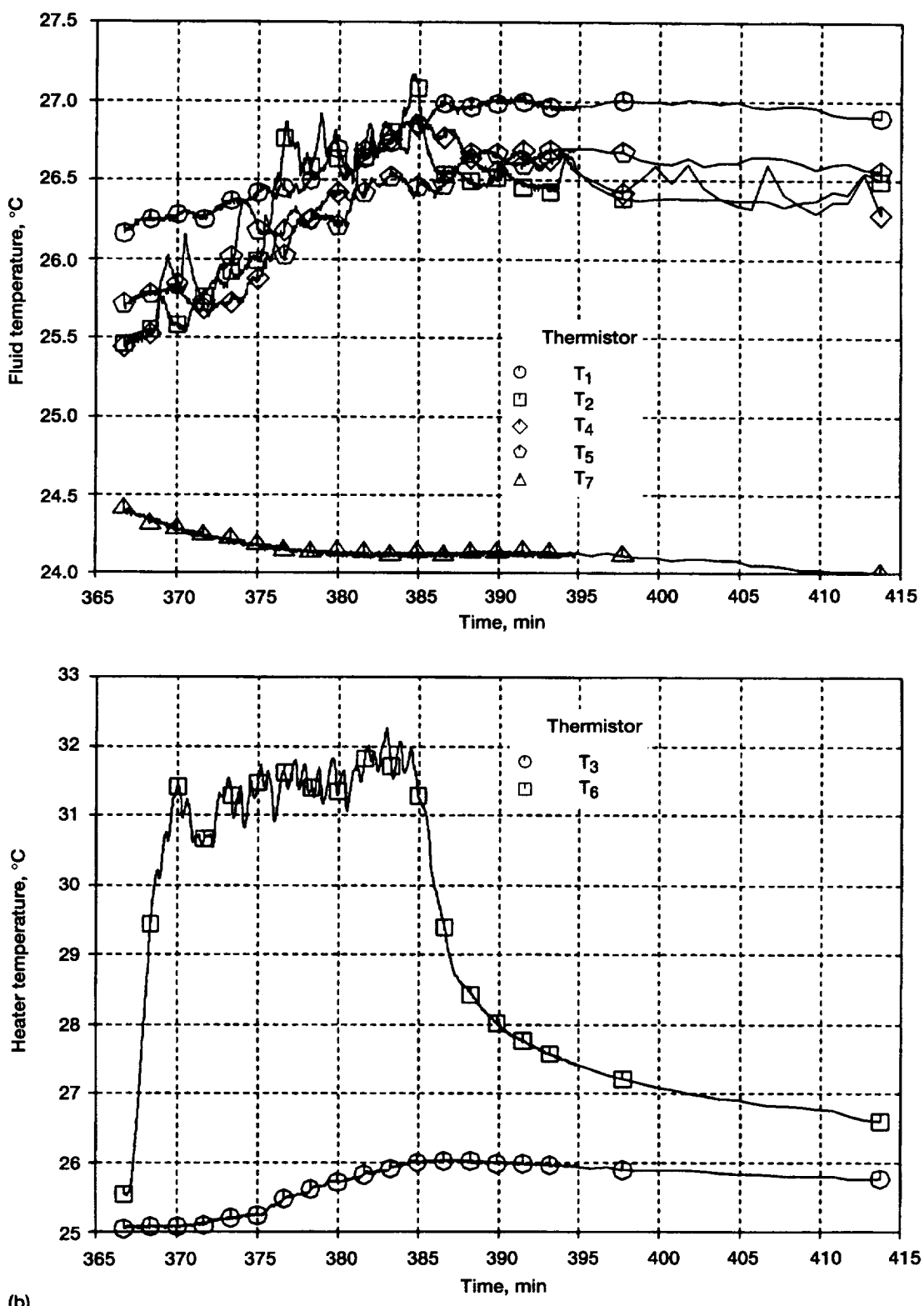


Figure A10.—Concluded. (c) Accelerations. (Bottom graph shows expanded scale.)



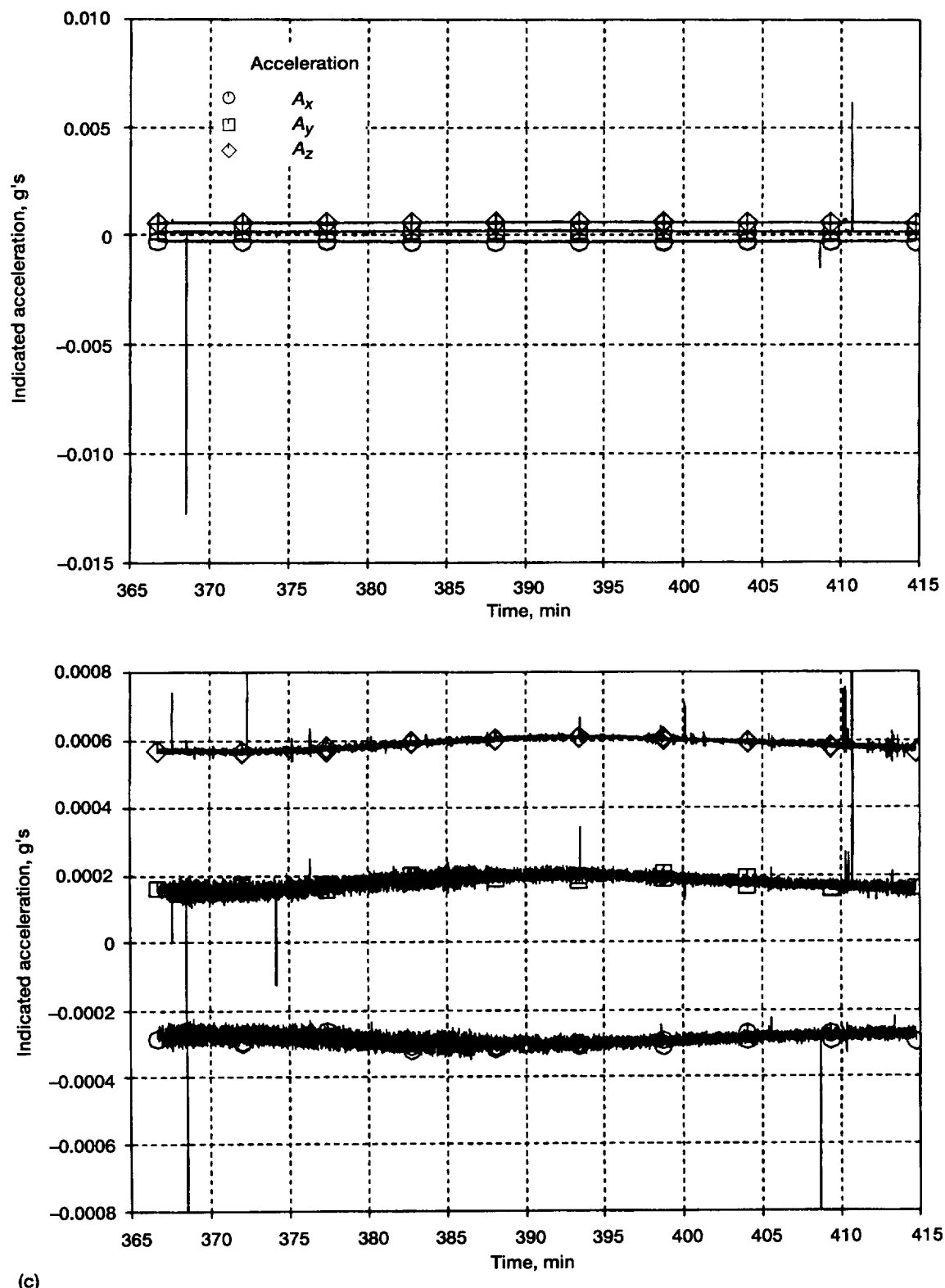
(a)

Figure A11.—Run 11. (a) Pressure and heater power. (b) Fluid and heater temperatures. (c) Accelerations.



(b)

Figure A11.—Continued. (b) Fluid and heater temperatures.



(c)

Figure A11.—Concluded. (c) Accelerations. (Bottom graph shows expanded scale.)

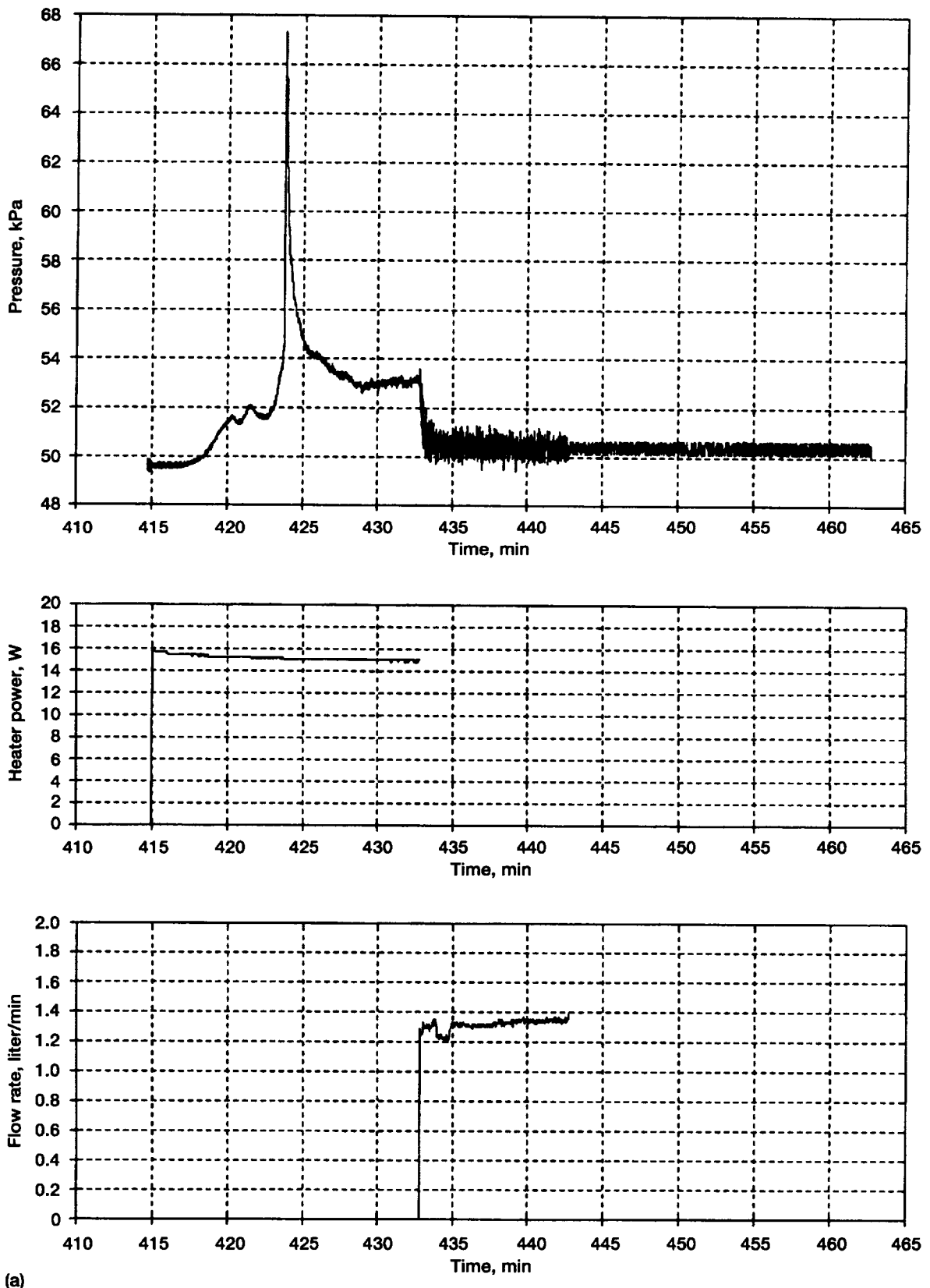
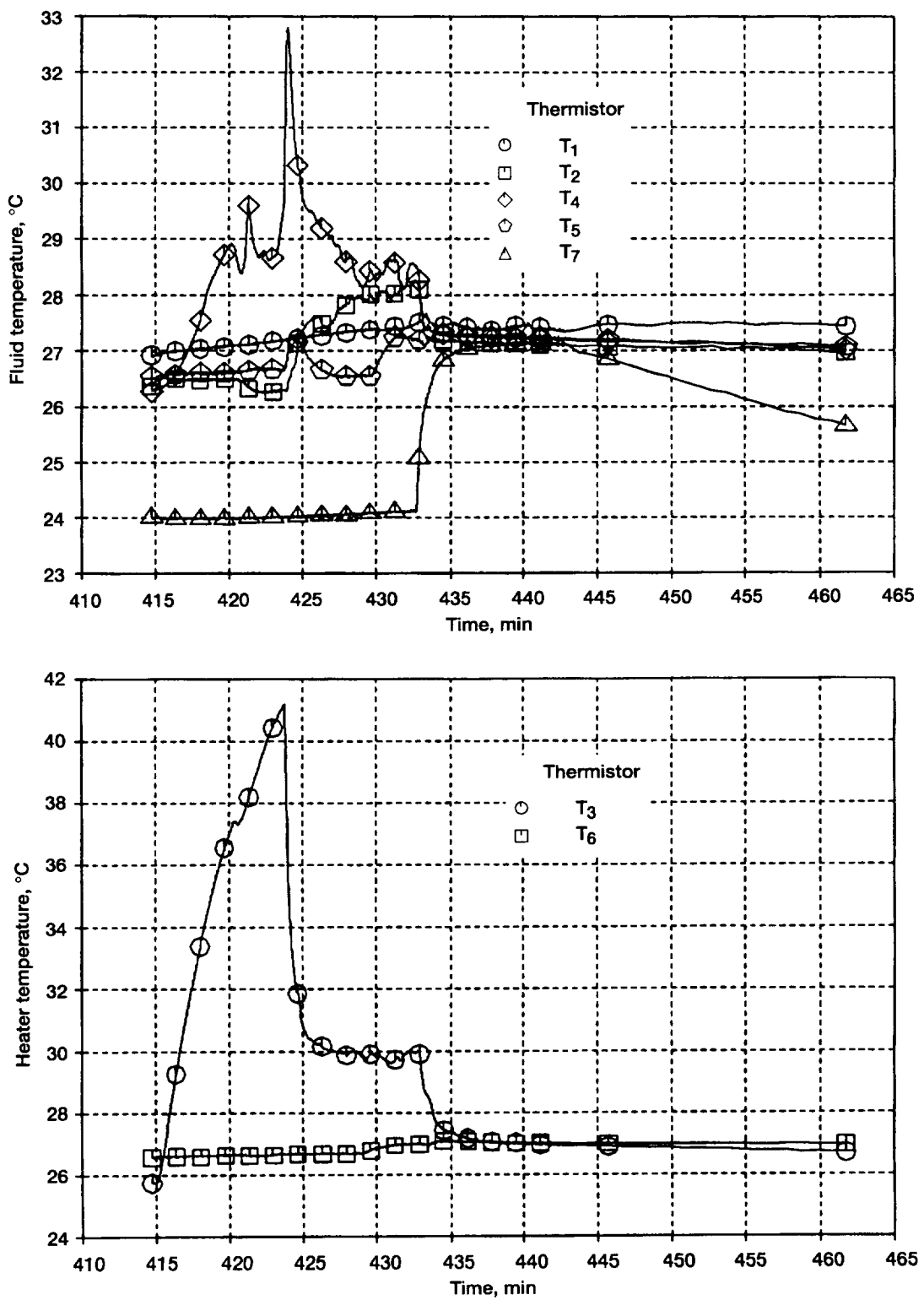


Figure A12.—Run 12. (a) Pressure, heater power, and flow rate. (b) Fluid and heater temperatures.
 (c) Accelerations.



(b)

Figure A12.—Continued. (b) Fluid and heater temperatures.

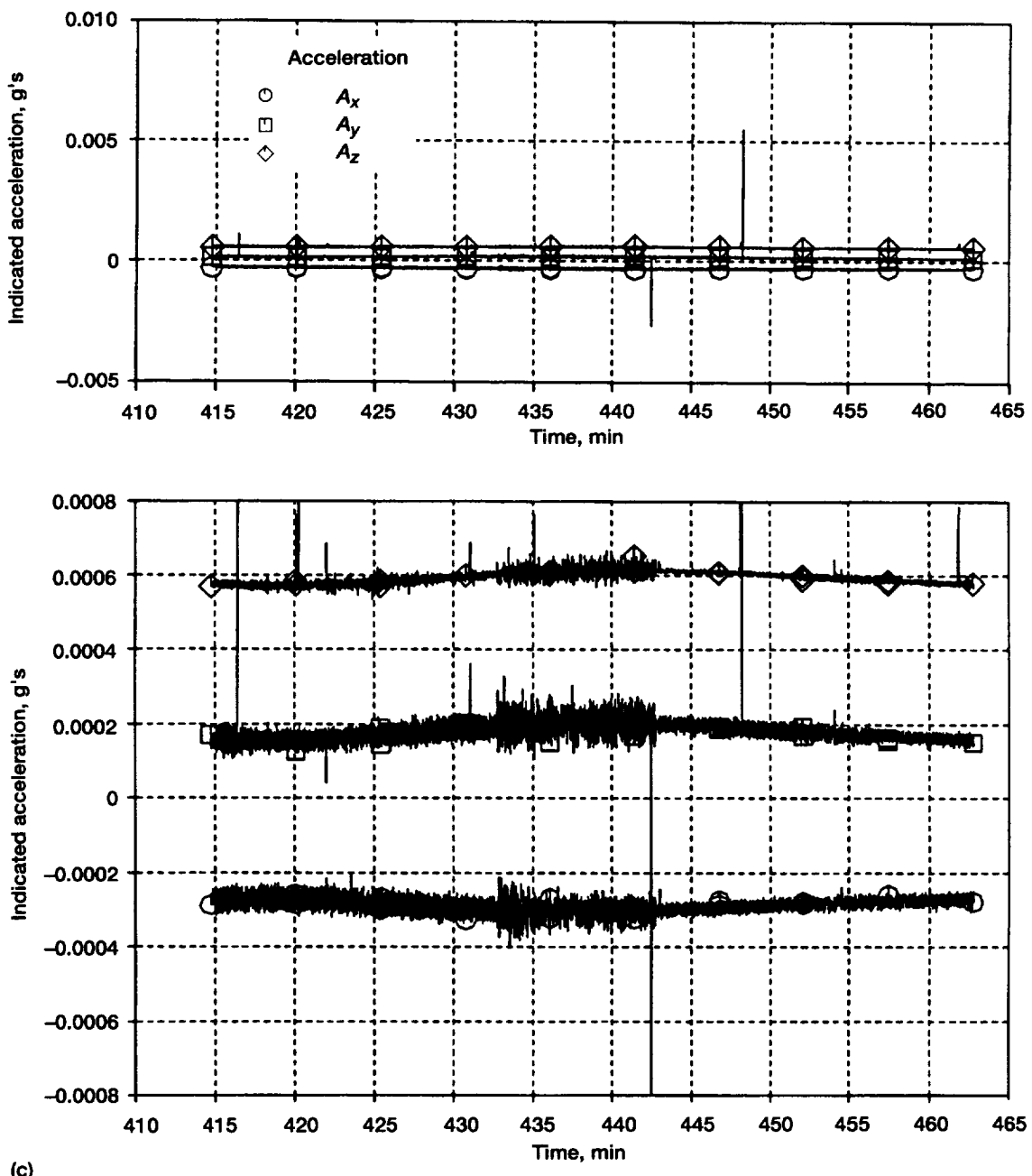
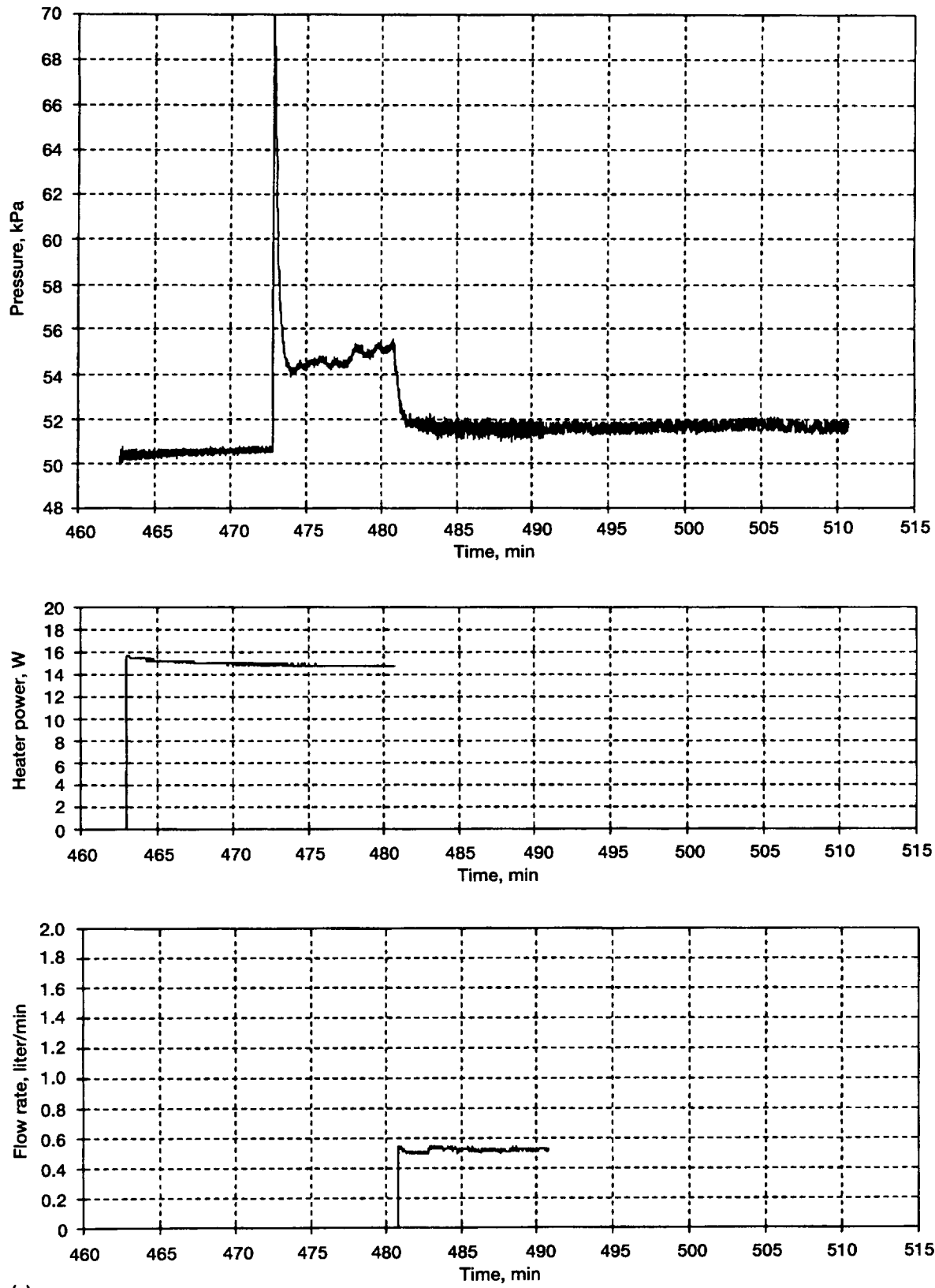


Figure A12.—Concluded. (c) Accelerations. (Bottom graph shows expanded scale.)



(a)

Figure A13.—Run 13. (a) Pressure, heater power, and flow rate. (b) Fluid and heater temperatures.
(c) Accelerations.

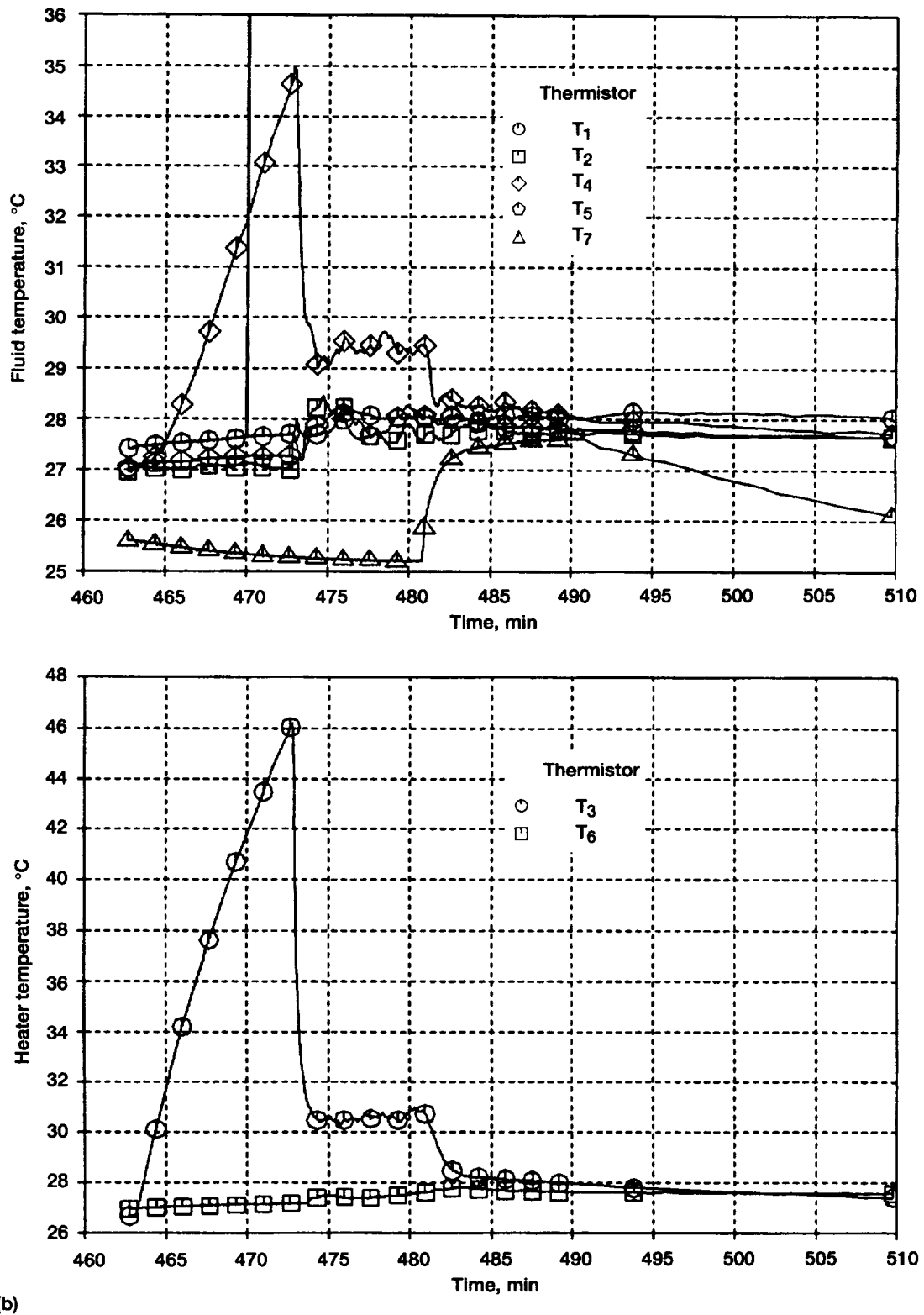
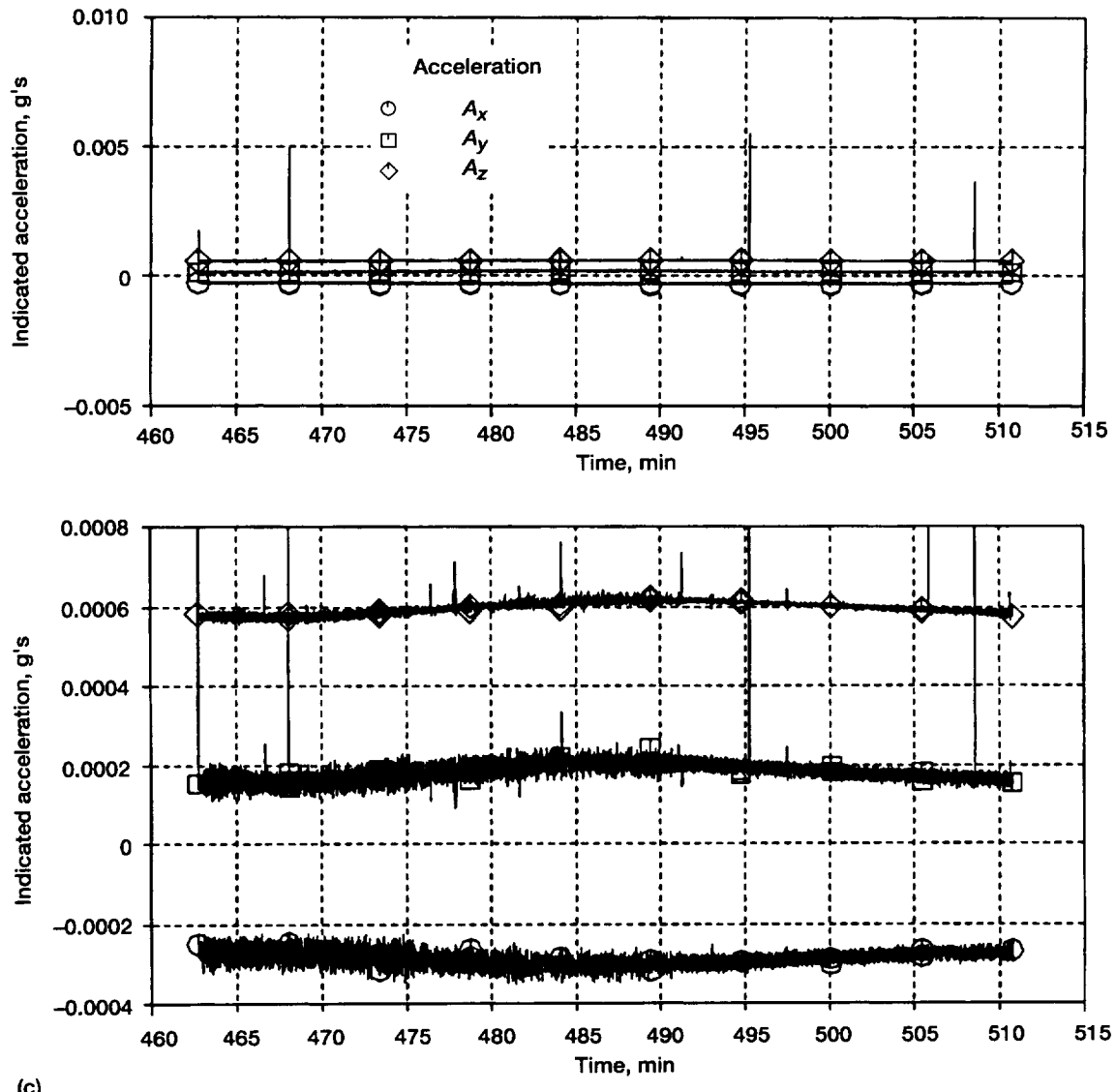
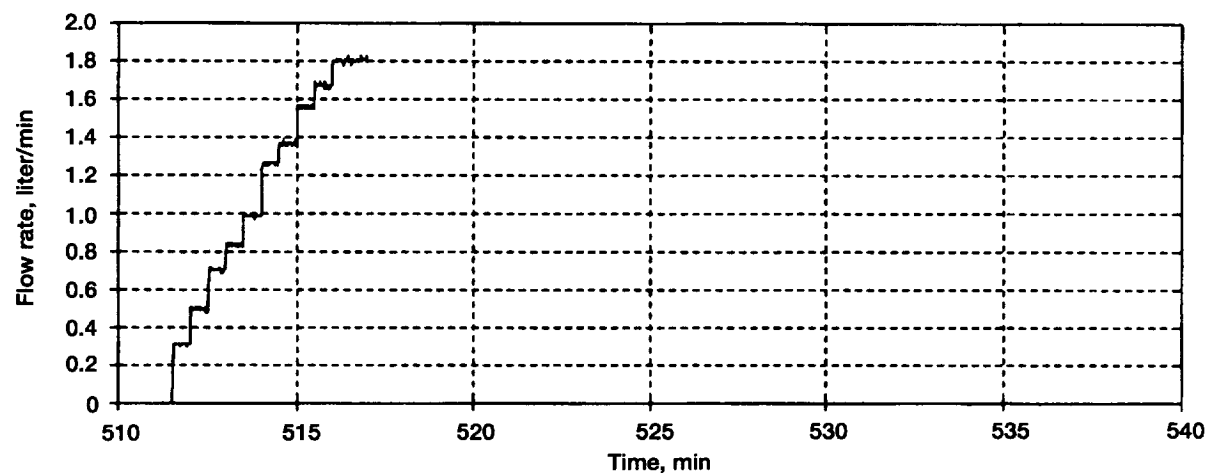
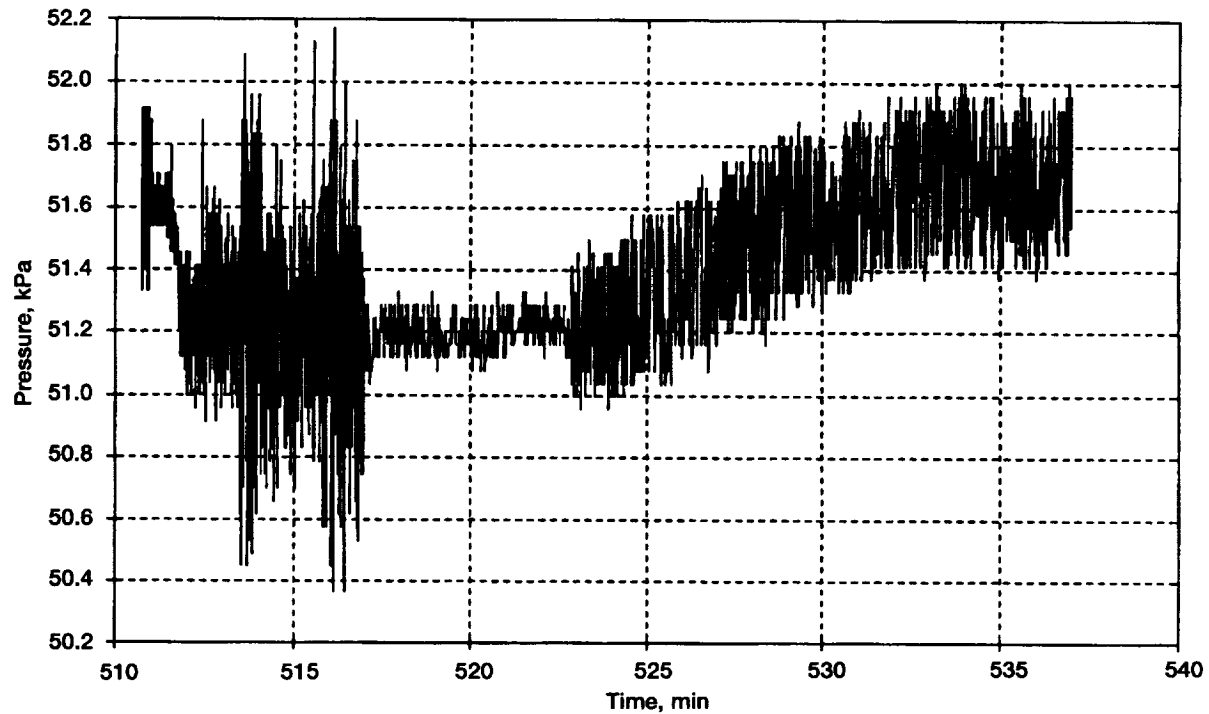


Figure A13.—Continued. (b) Fluid and heater temperatures.



(c)

Figure A13.—Concluded. (c) Accelerations. (Bottom graph shows expanded scale.)



(a)

Figure A14.—Run 14. (a) Pressure and flow rate. (b) Fluid and heater temperatures. (c) Accelerations.

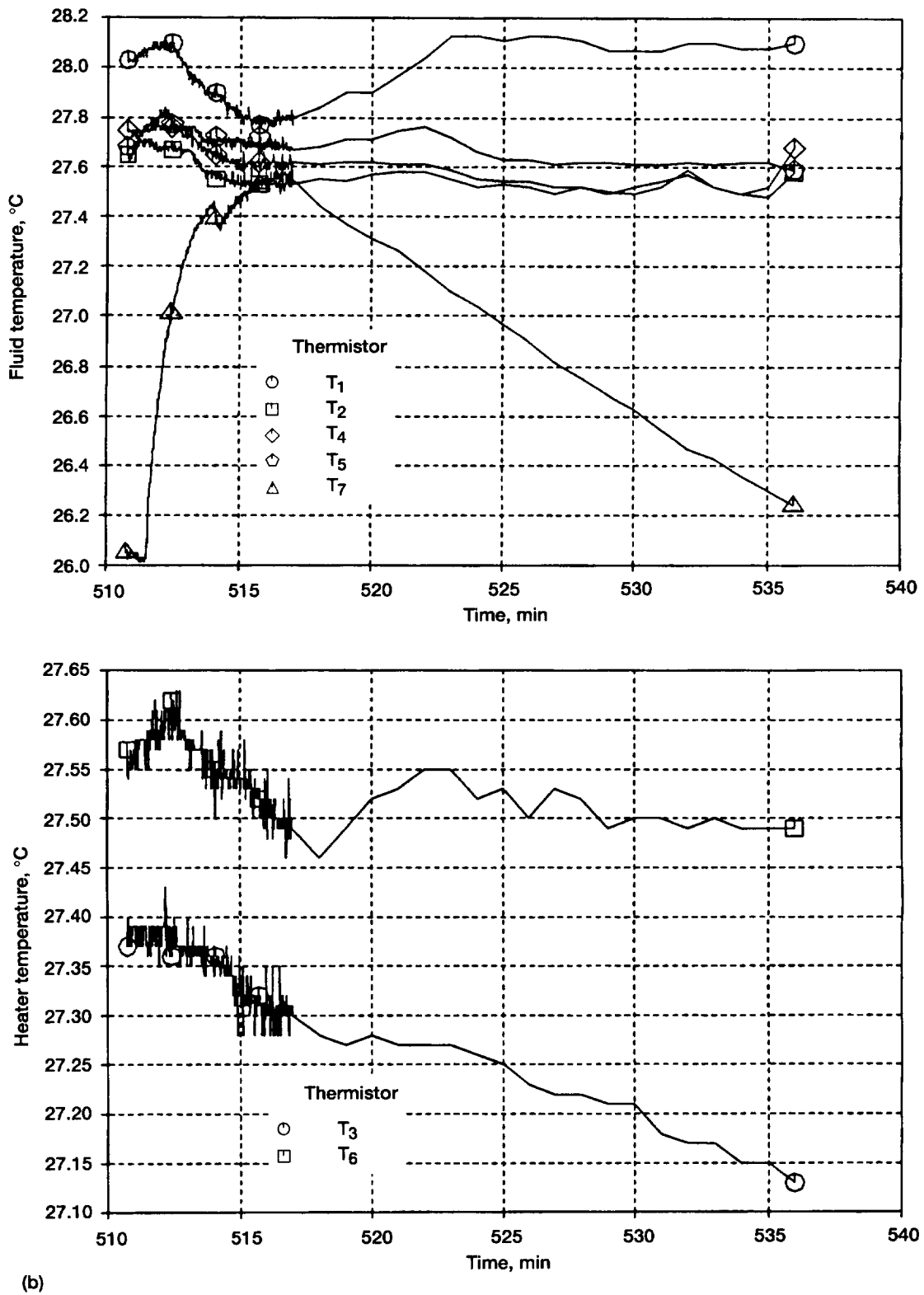


Figure A14.—Continued. (b) Fluid and heater temperatures.

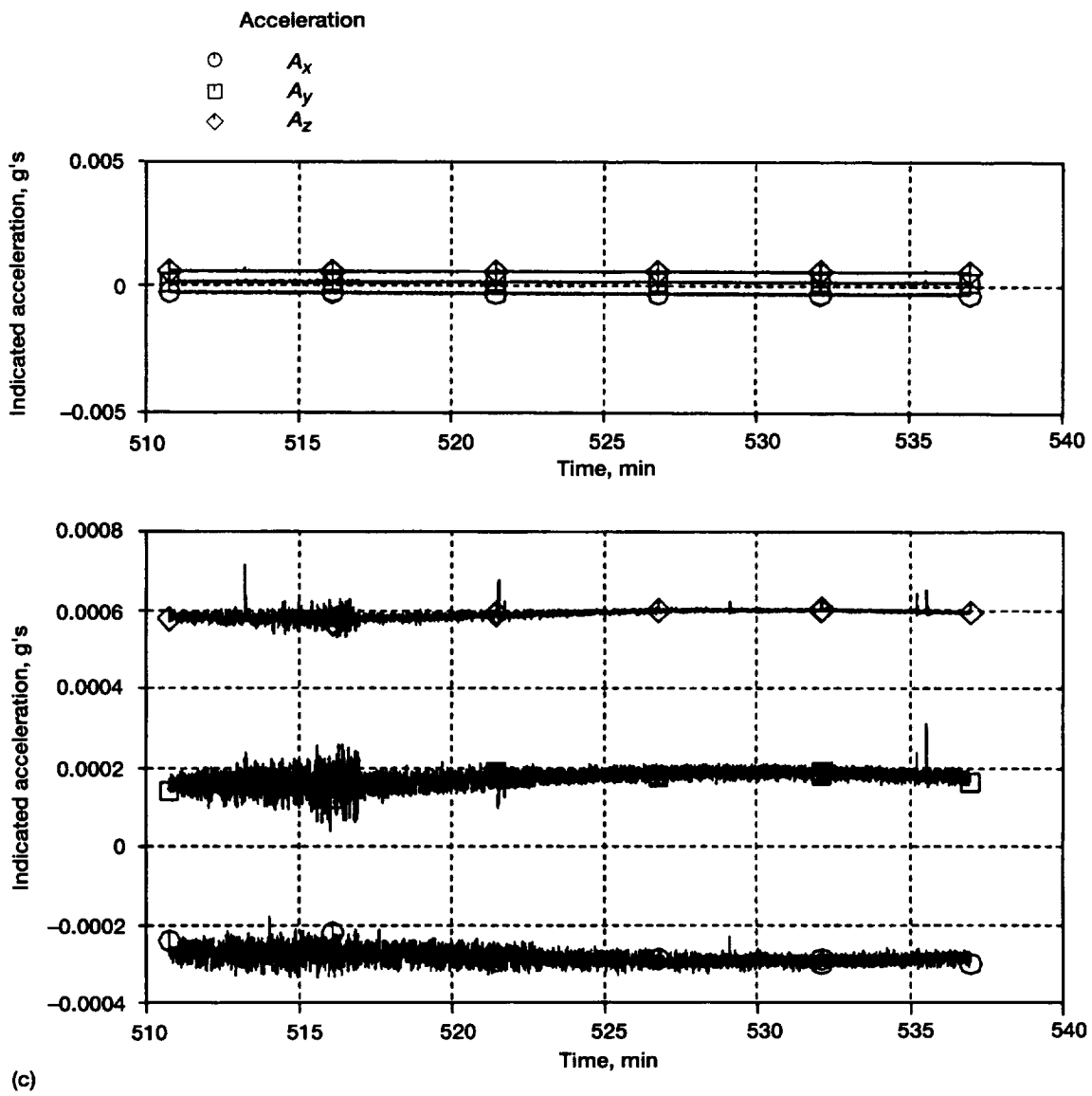
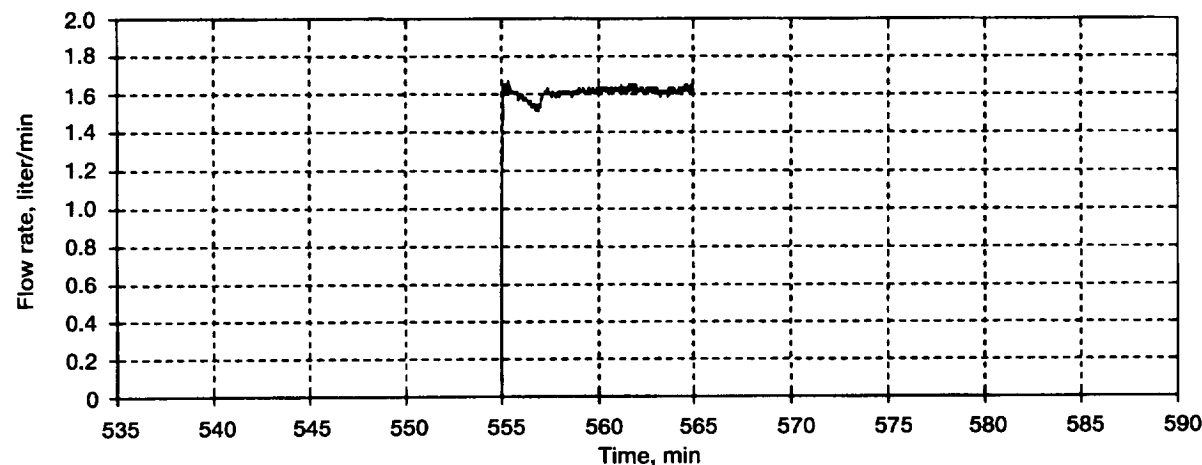
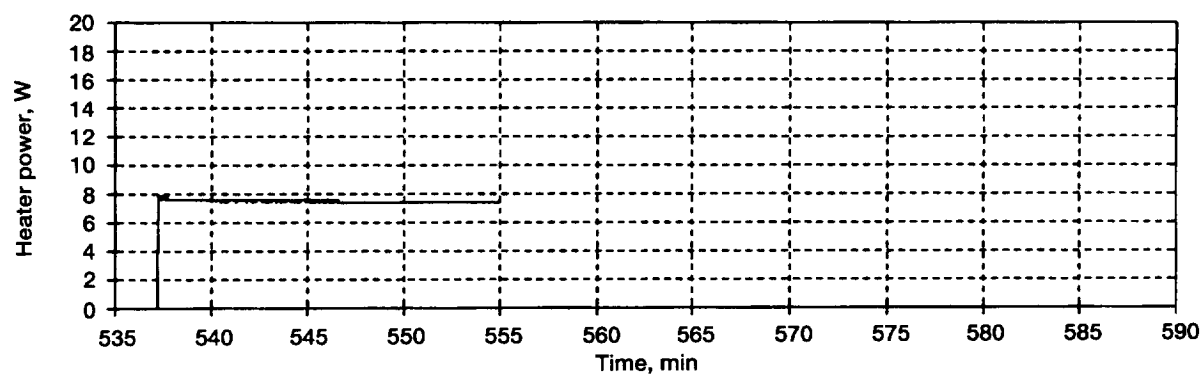
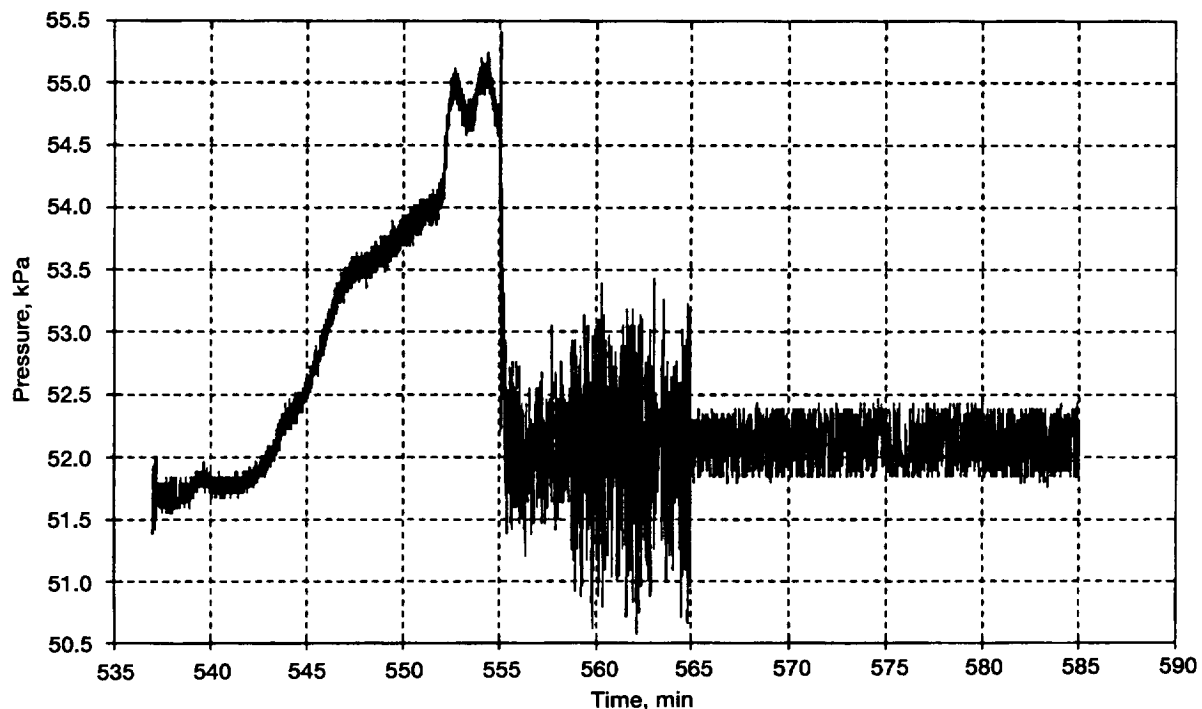


Figure A14.—Concluded. (c) Accelerations. (Bottom graph shows expanded scale.)



(a)

Figure A15.—Run 15. (a) Pressure, heater power, and flow rate. (b) Fluid and heater temperatures. (c) Accelerations.

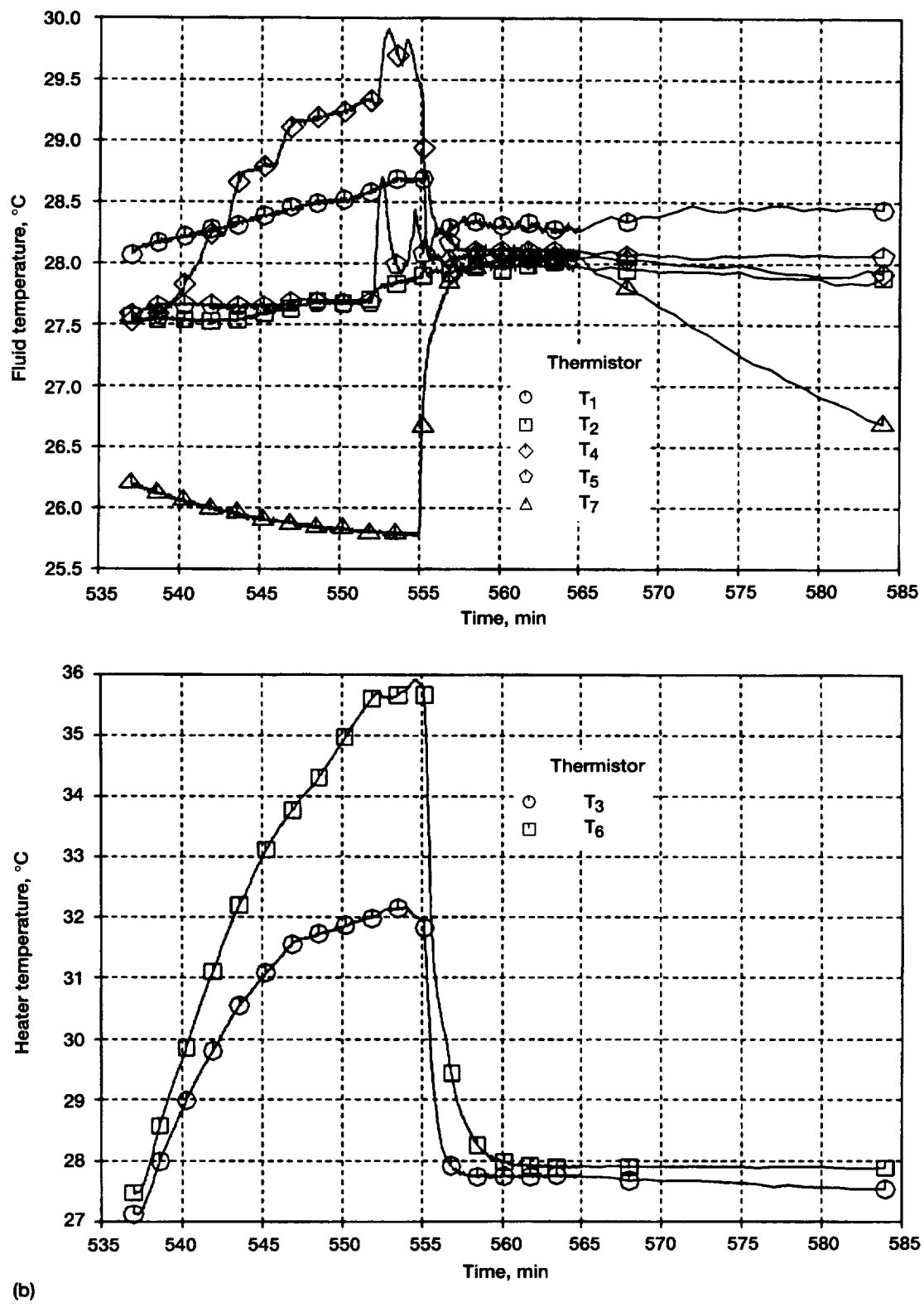
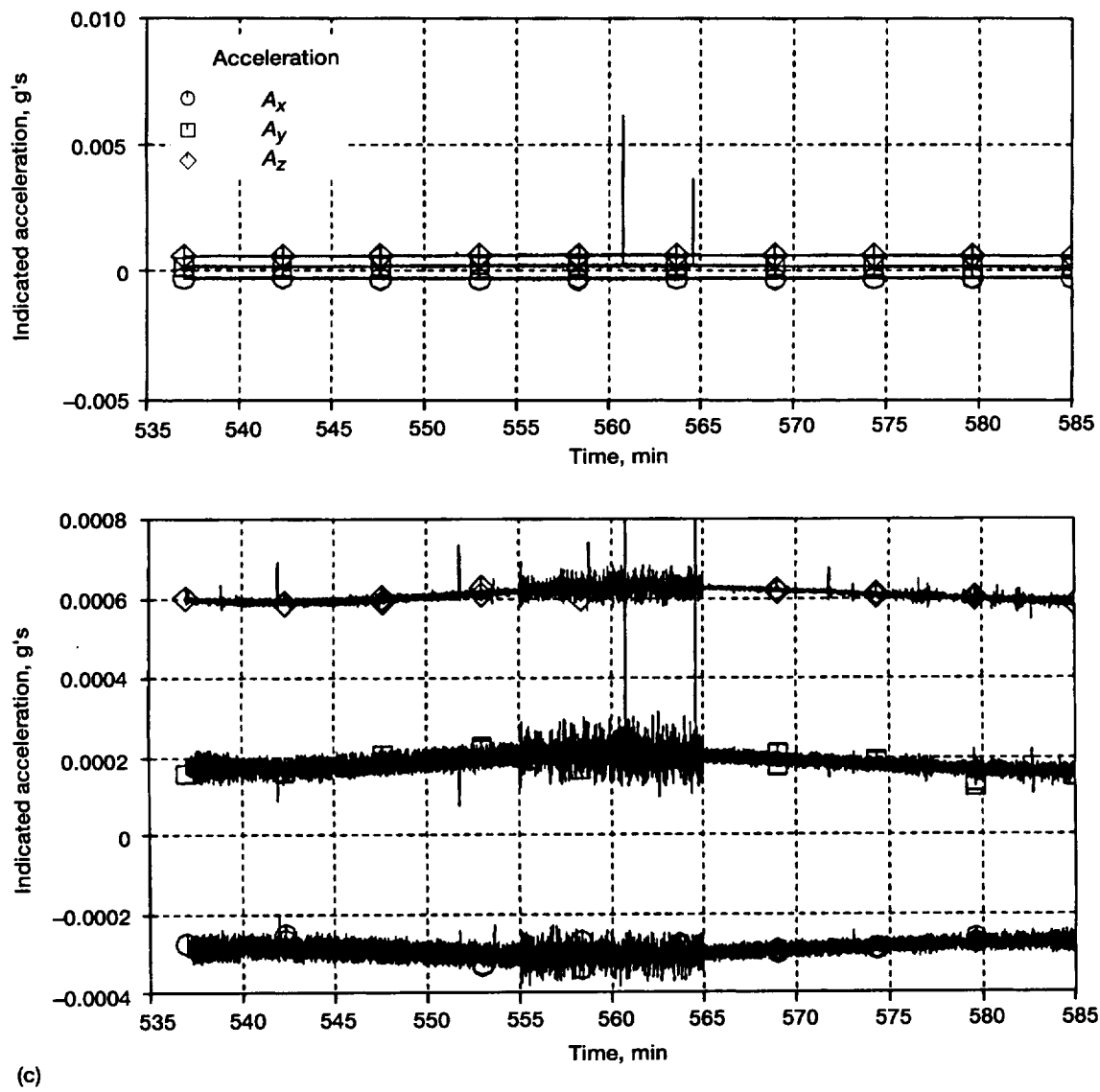


Figure A15.—Continued. (b) Fluid and heater temperatures.



(c)

Figure A15.—Concluded. (c) Accelerations. (Bottom graph shows expanded scale.)

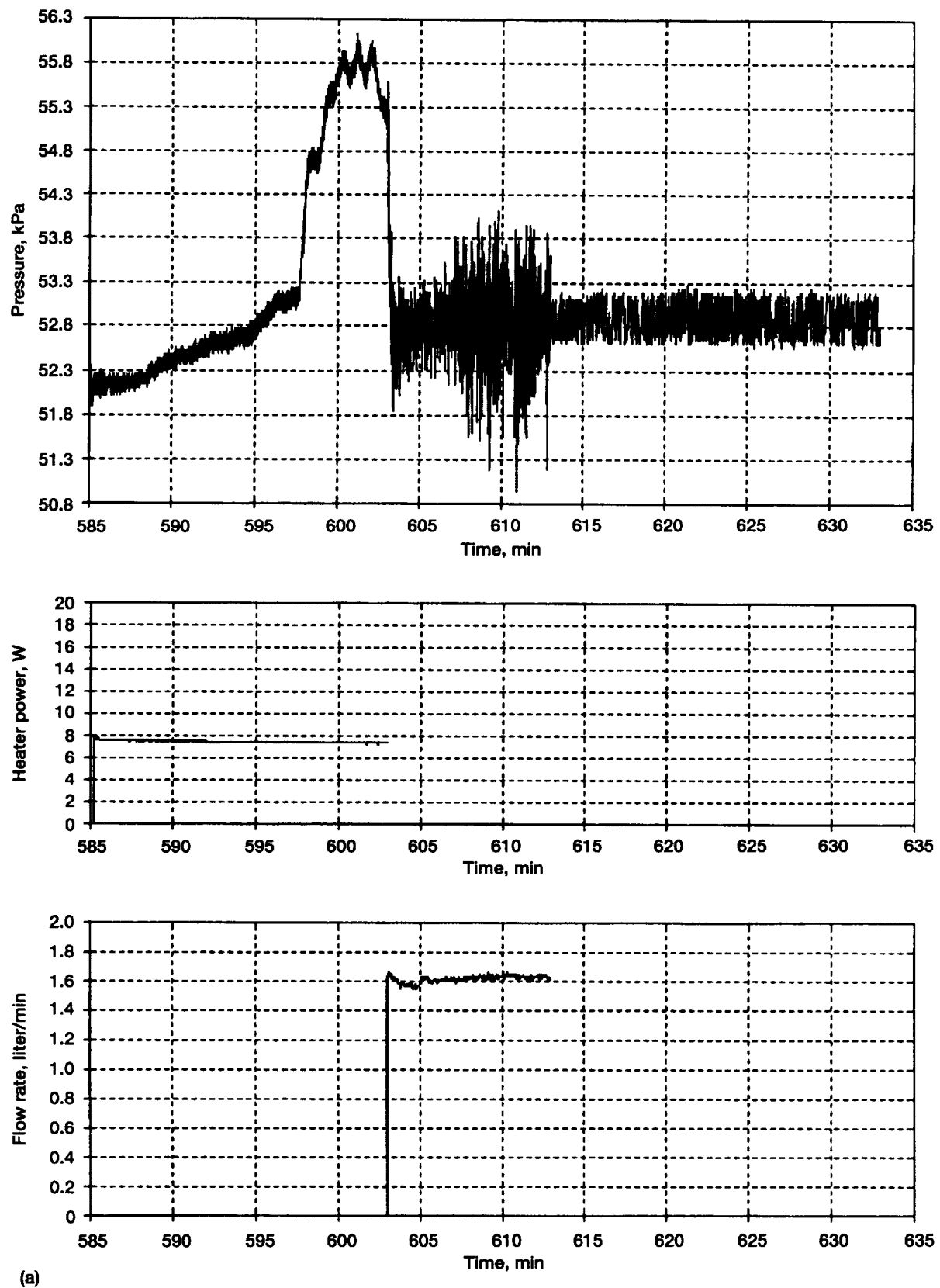
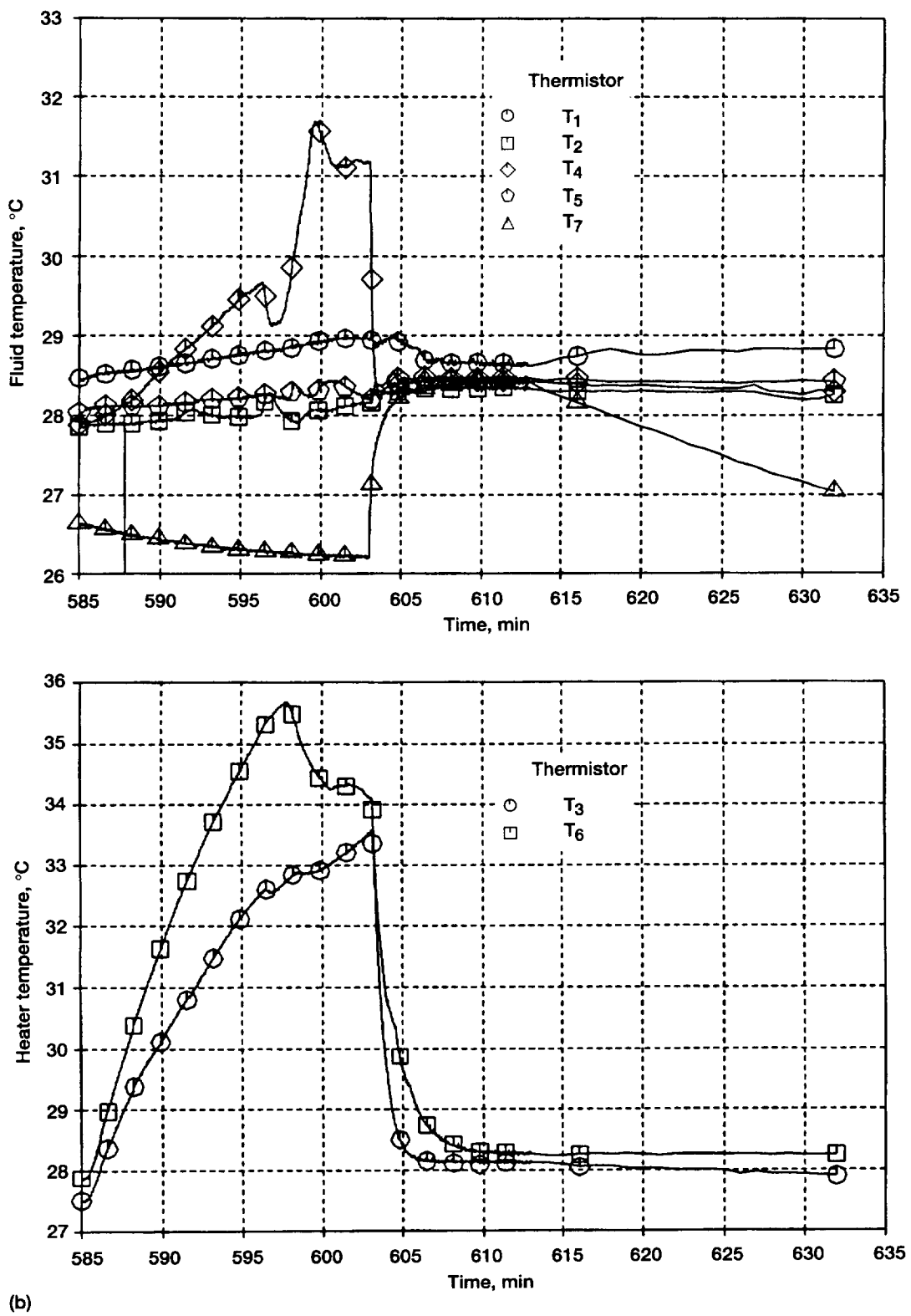


Figure A16.—Run 16. (a) Pressure, heater power, and flow rate. (b) Fluid and heater temperatures. (c) Accelerations.



(b)

Figure A16.—Continued. (b) Fluid and heater temperatures.

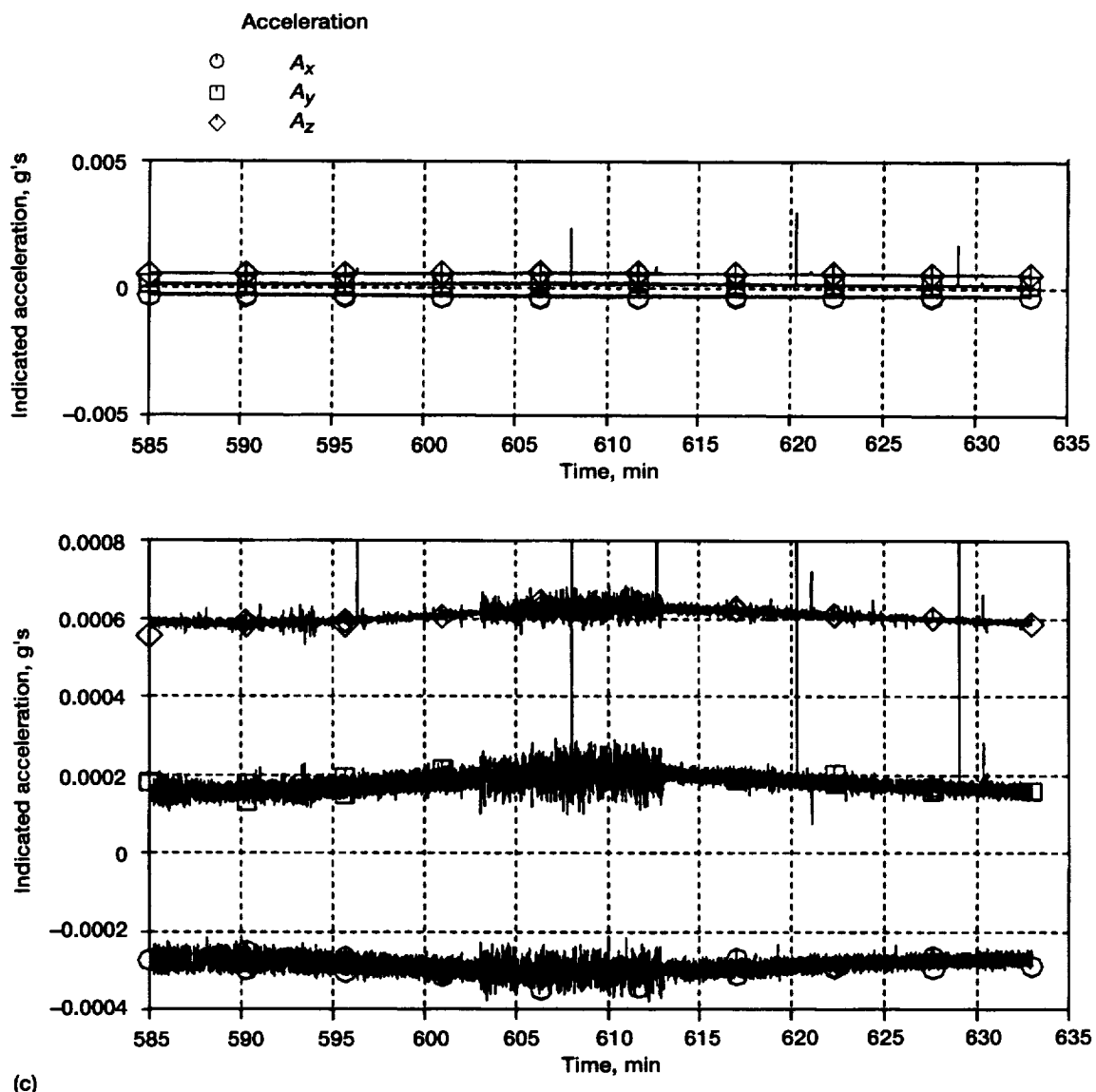


Figure A16.—Concluded. (c) Accelerations. (Bottom graph shows expanded scale.)

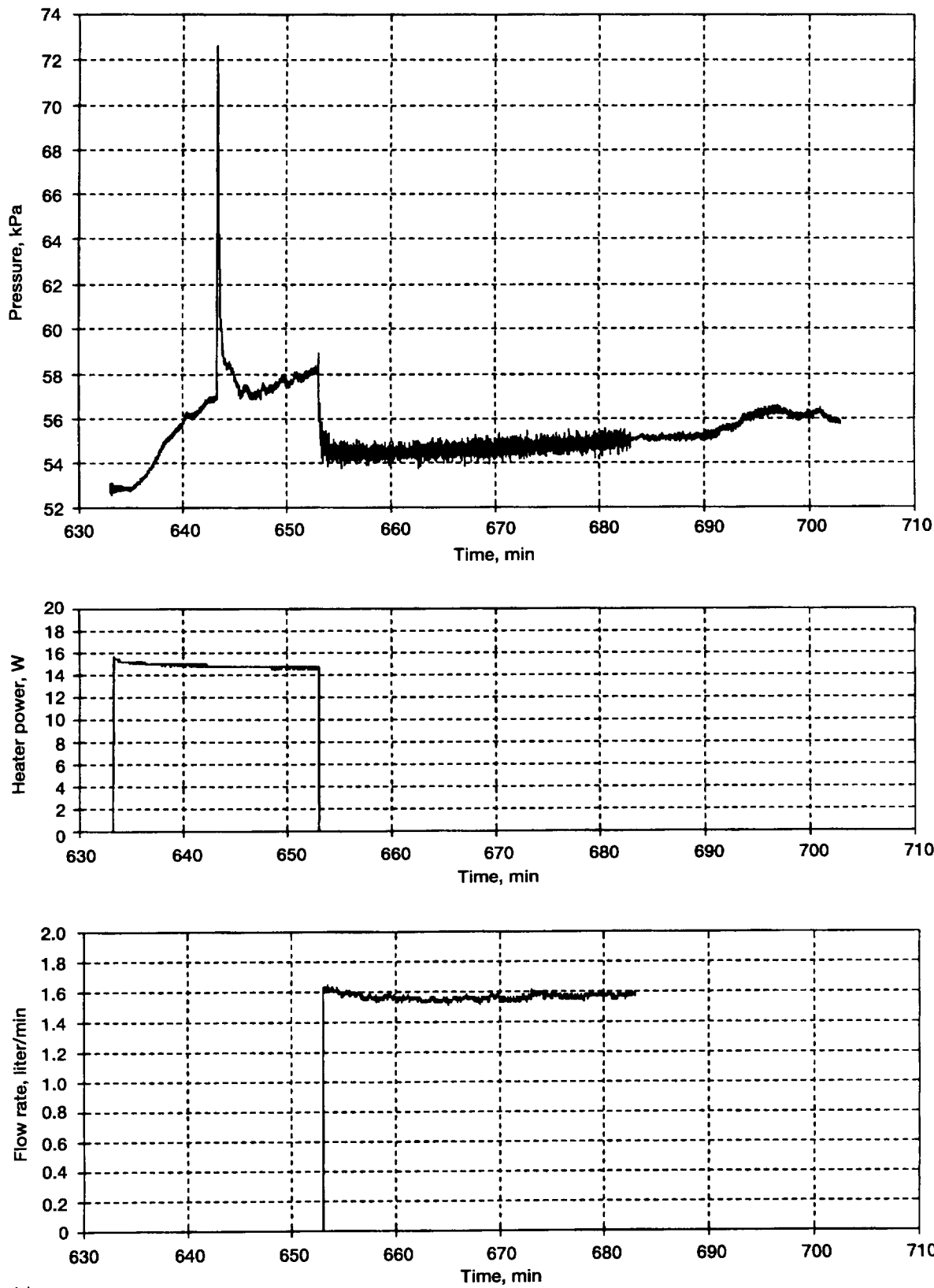


Figure A17.—Run 17. (a) Pressure, heater power, and flow rate. (b) Fluid and heater temperatures. (c) Accelerations.

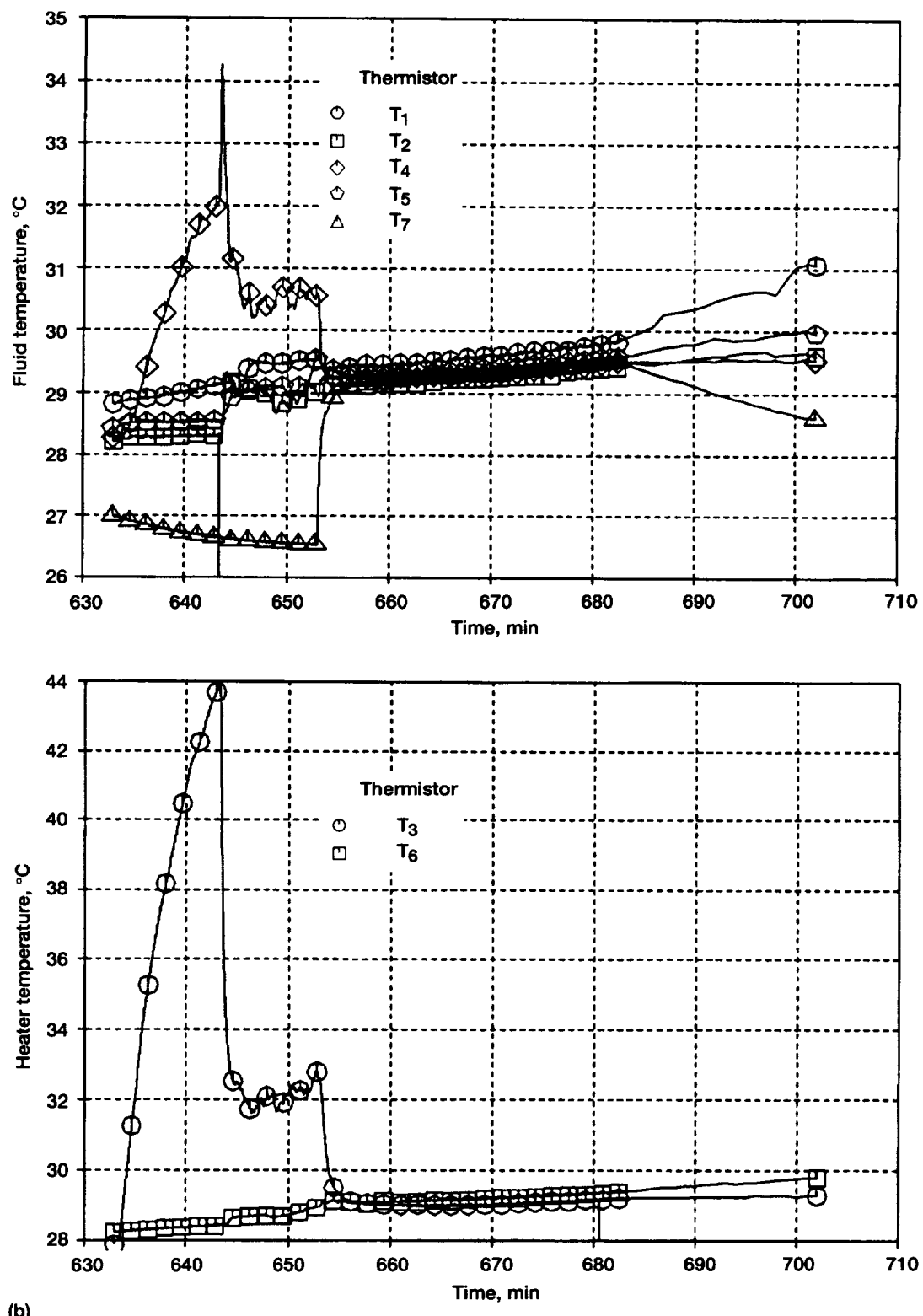


Figure A17.—Continued. (b) Fluid and heater temperatures.

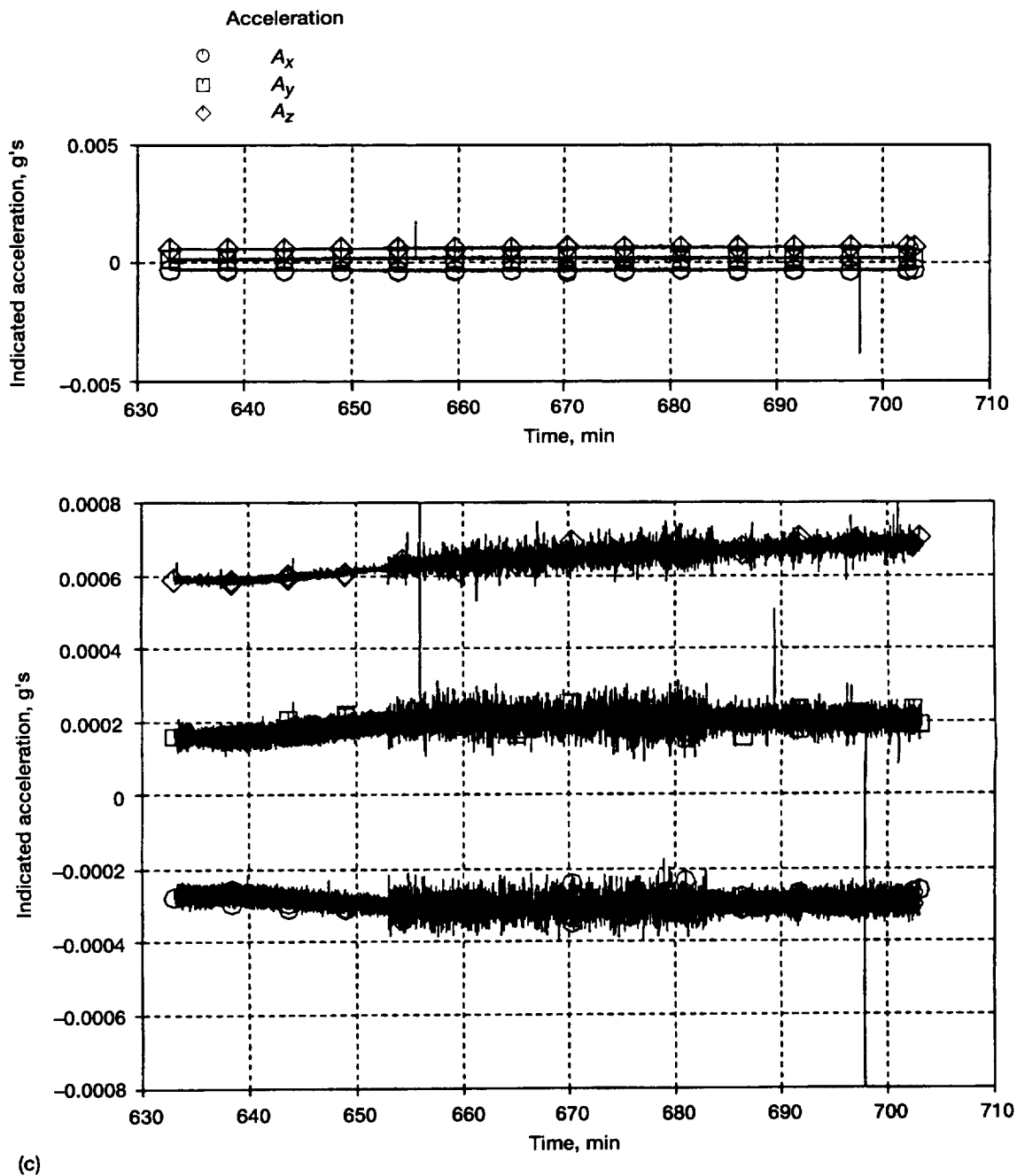


Figure A17.—Concluded. (c) Accelerations. (Bottom graph shows expanded scale.)

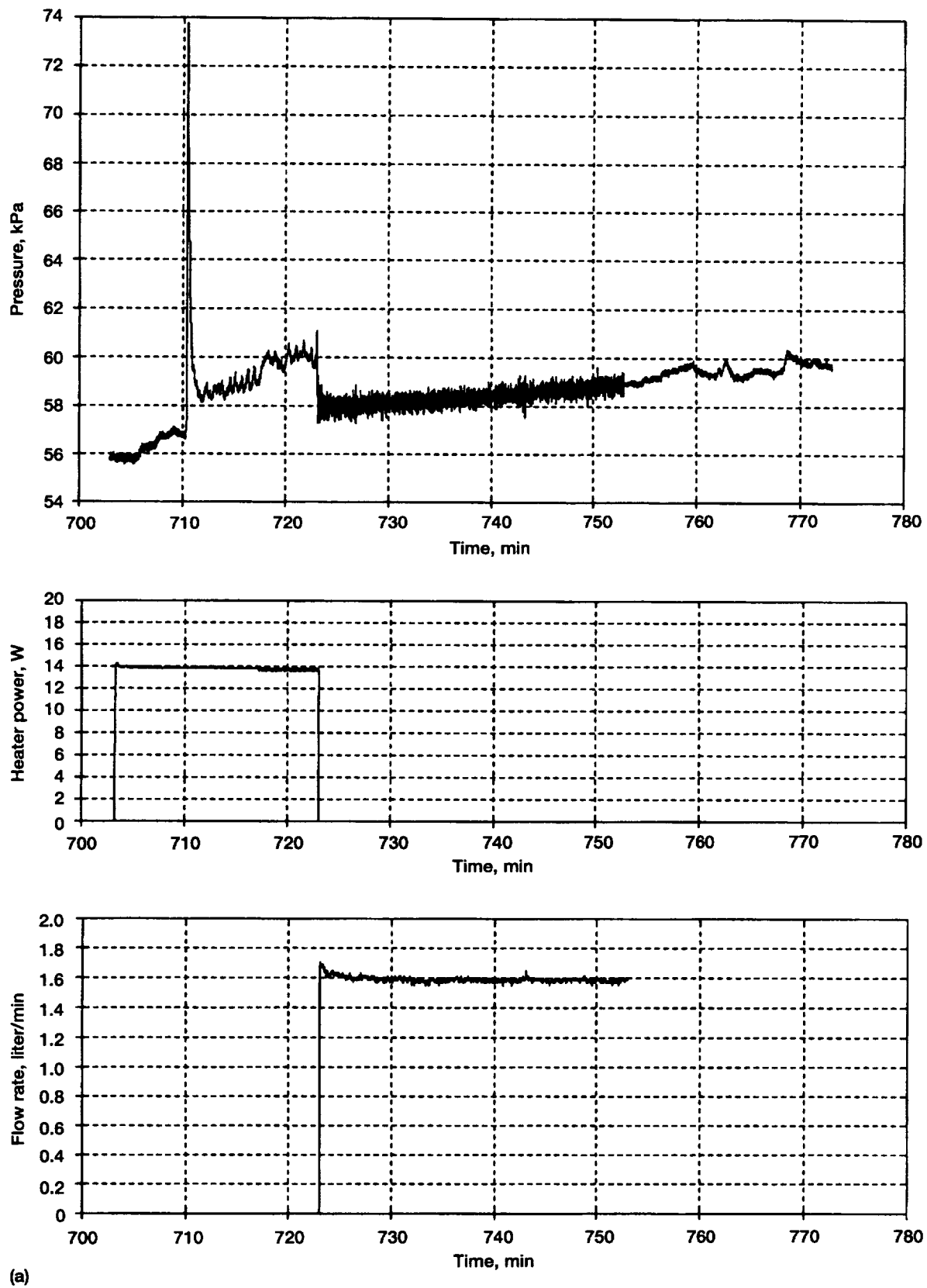


Figure A18.—Run 18. (a) Pressure, heater power, and flow rate. (b) Fluid and heater temperatures. (c) Accelerations.

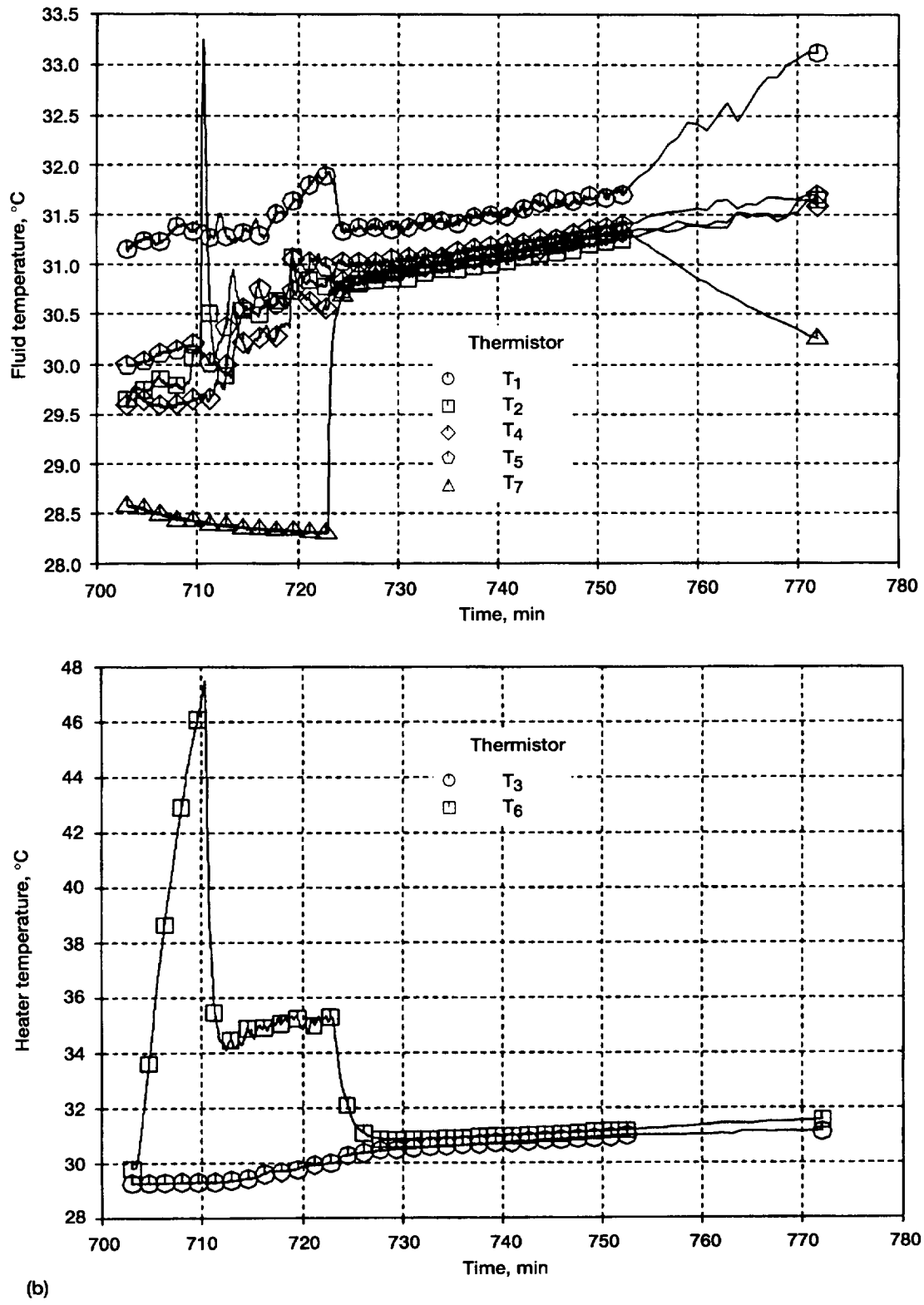
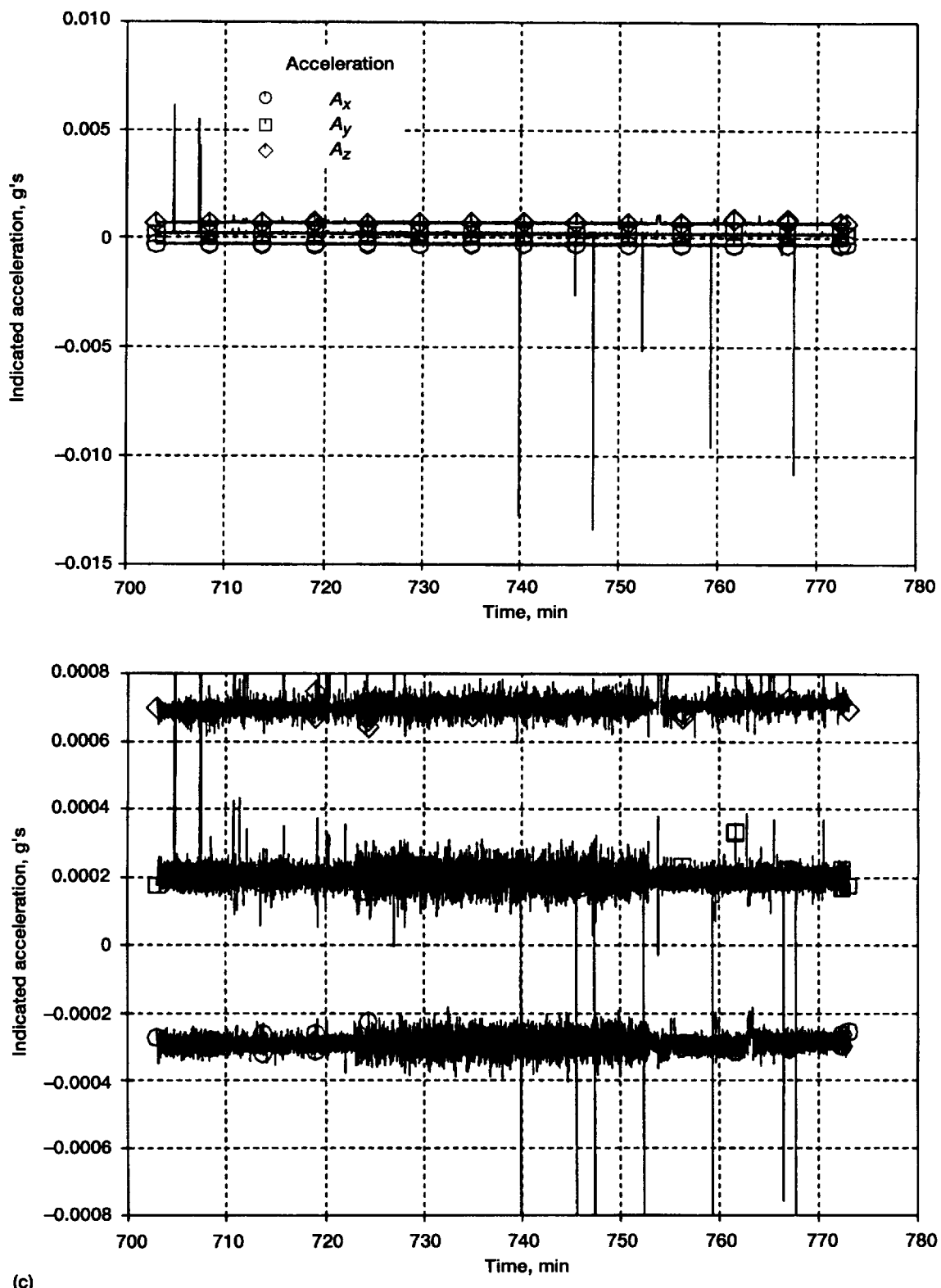
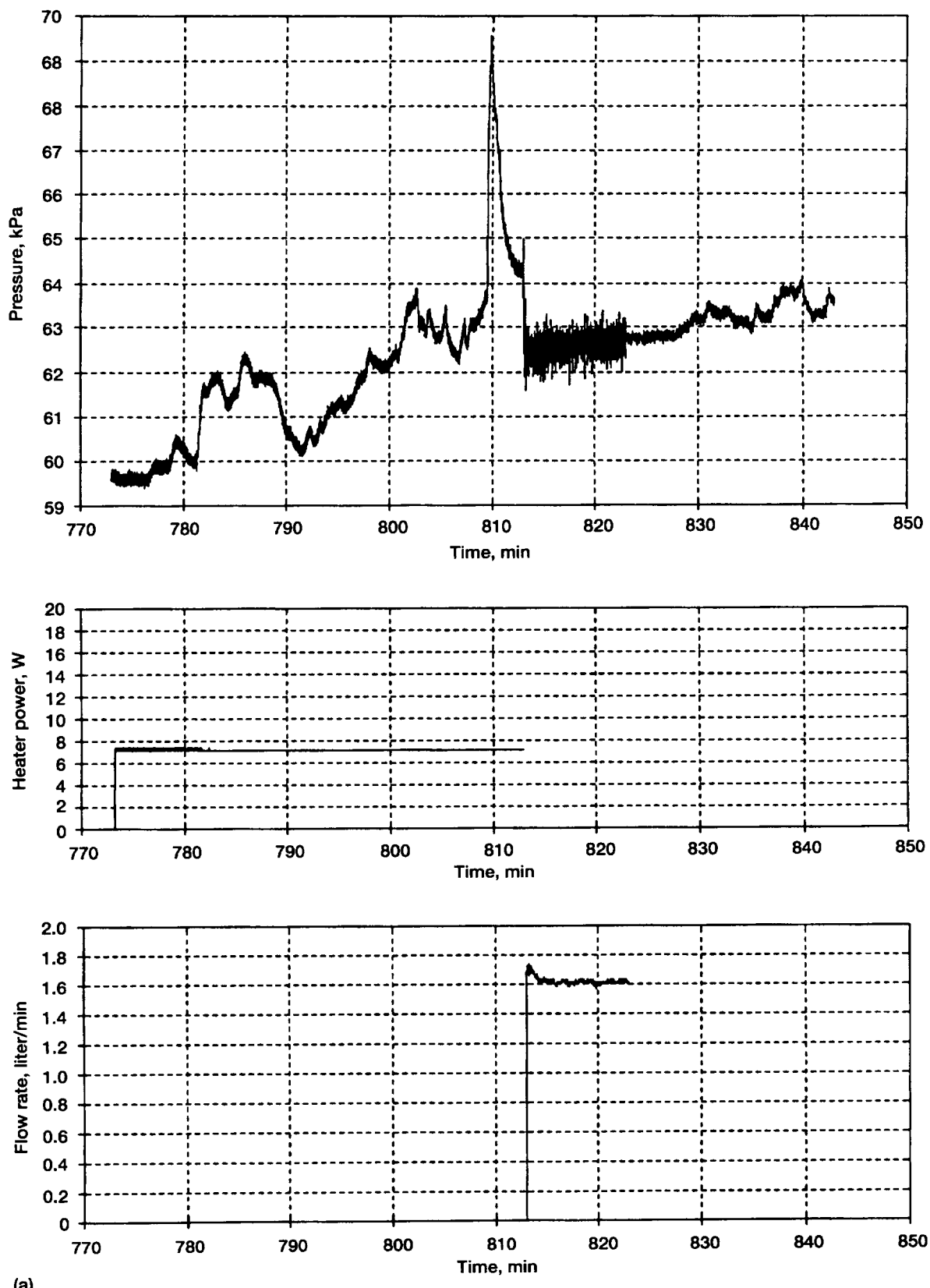


Figure A18.—Continued. (b) Fluid and heater temperatures.



(c)

Figure A18.—Concluded. (c) Accelerations. (Bottom graph shows expanded scale.)



(a)

Figure A19.—Run 19. (a) Pressure, heater power, and flow rate. (b) Fluid and heater temperatures. (c) Accelerations.

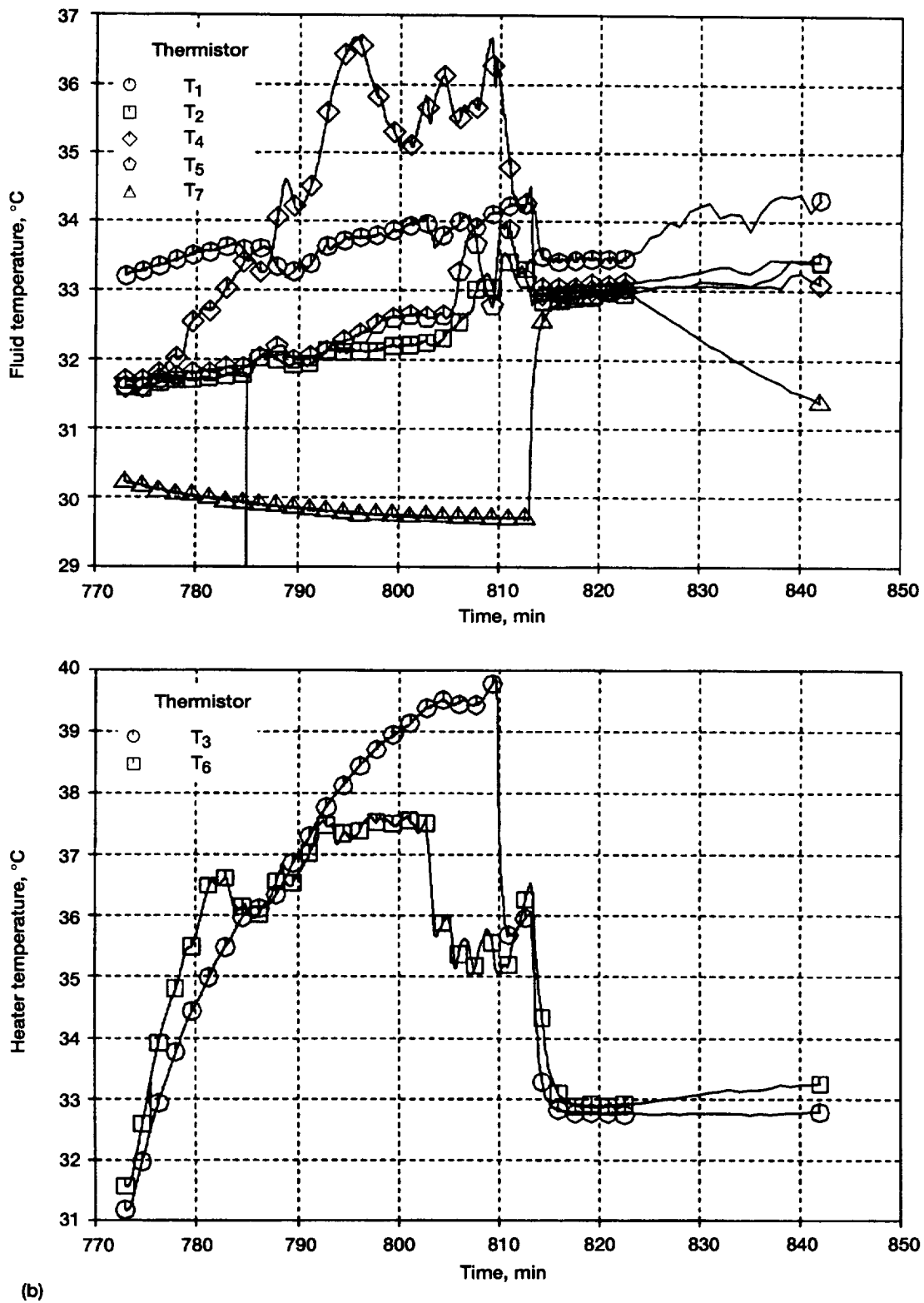
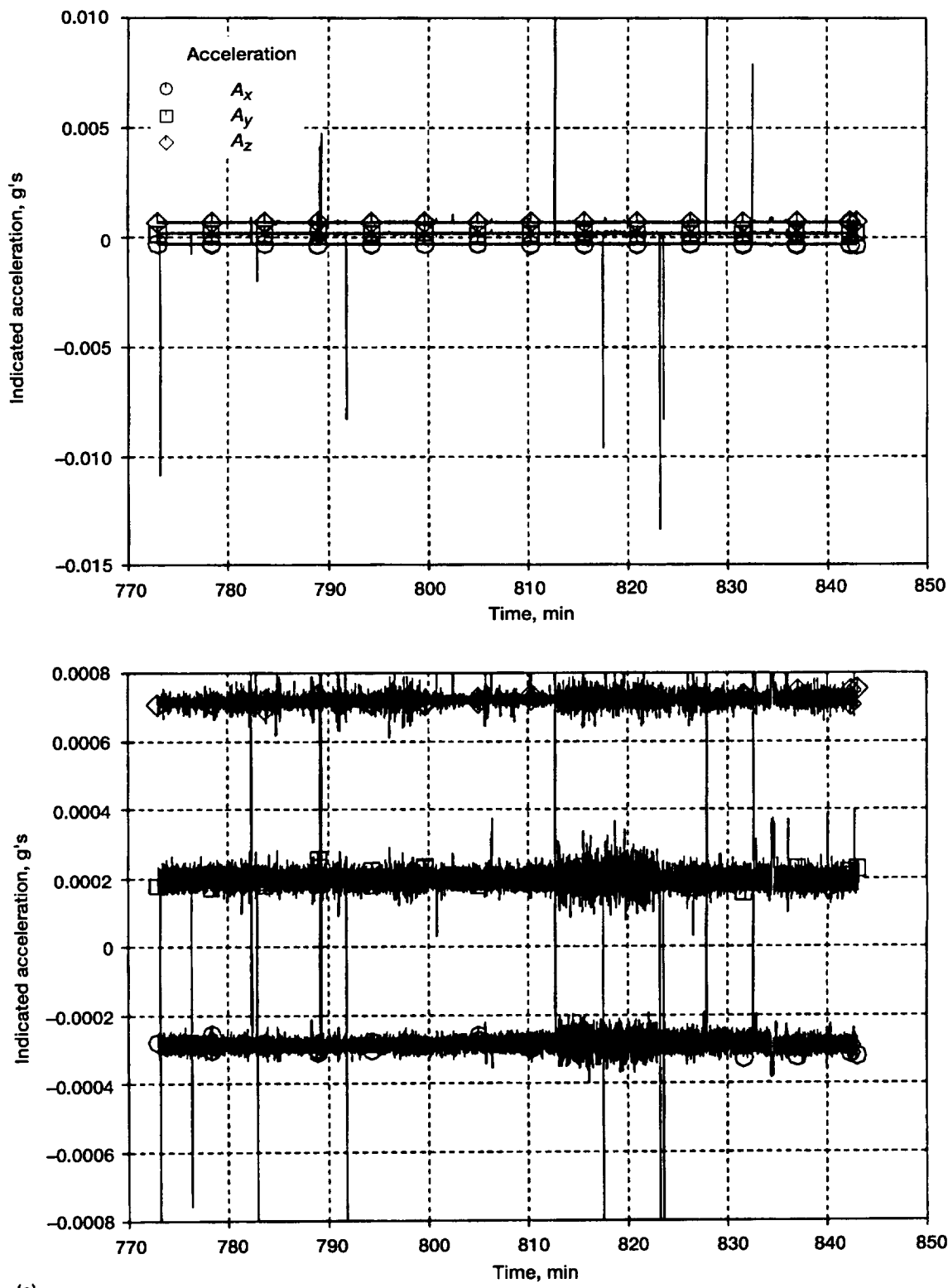


Figure A19.—Continued. (b) Fluid and heater temperatures.



(c)

Figure A19.—Concluded. (c) Accelerations. (Bottom graph shows expanded scale.)

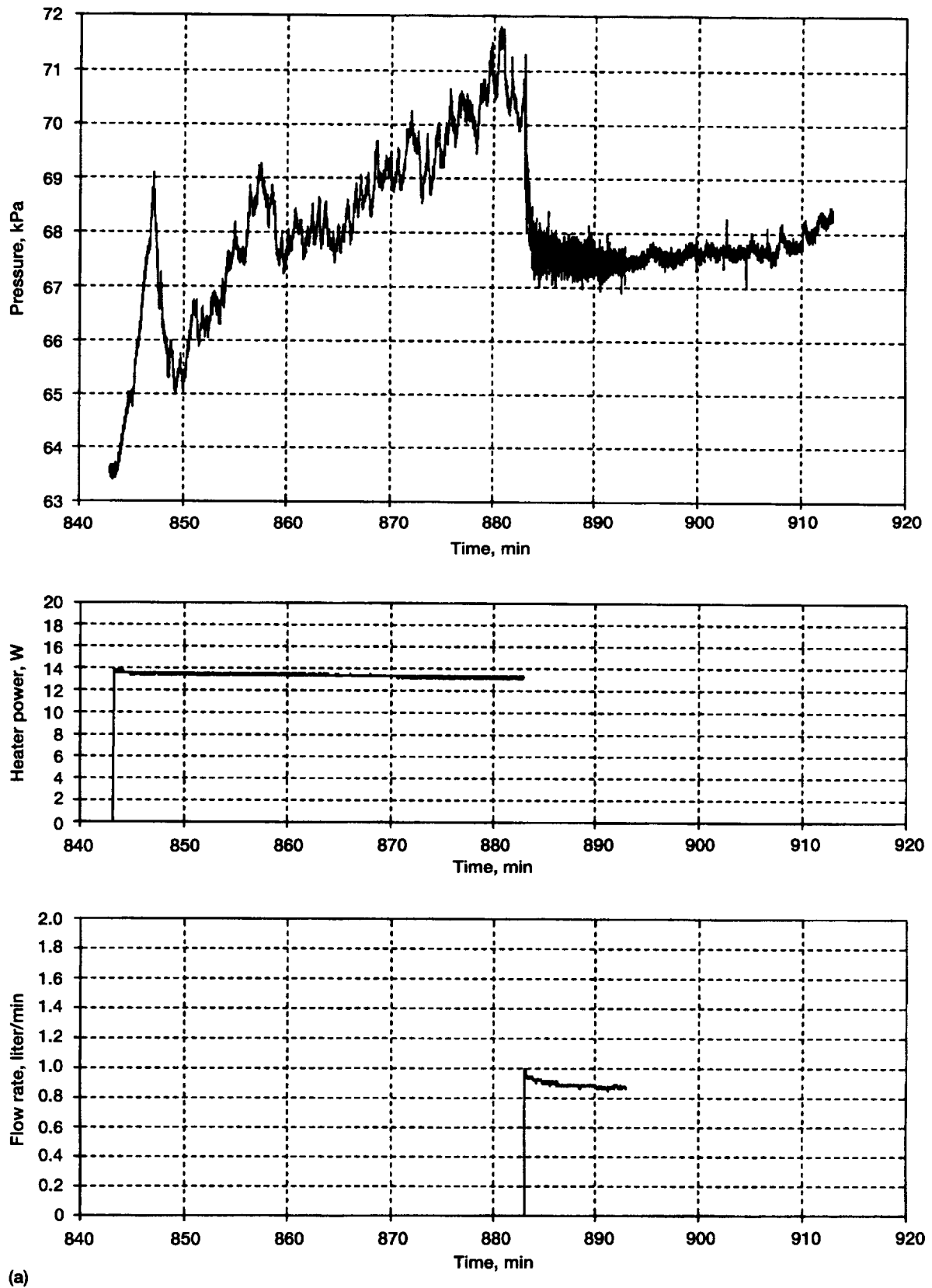


Figure A20.—Run 20. (a) Pressure, heater power, and flow rate. (b) Fluid and heater temperatures. (c) Accelerations.

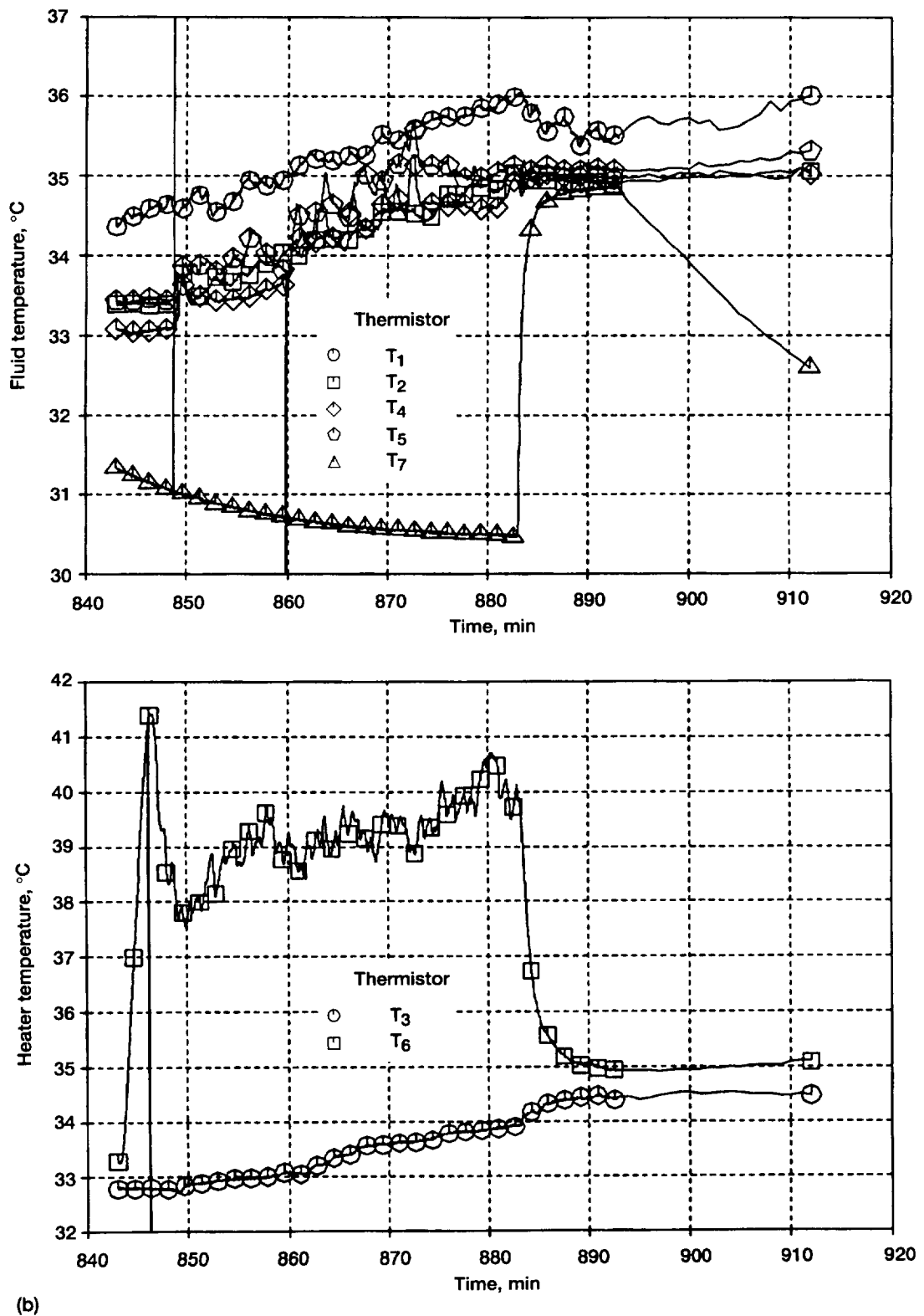
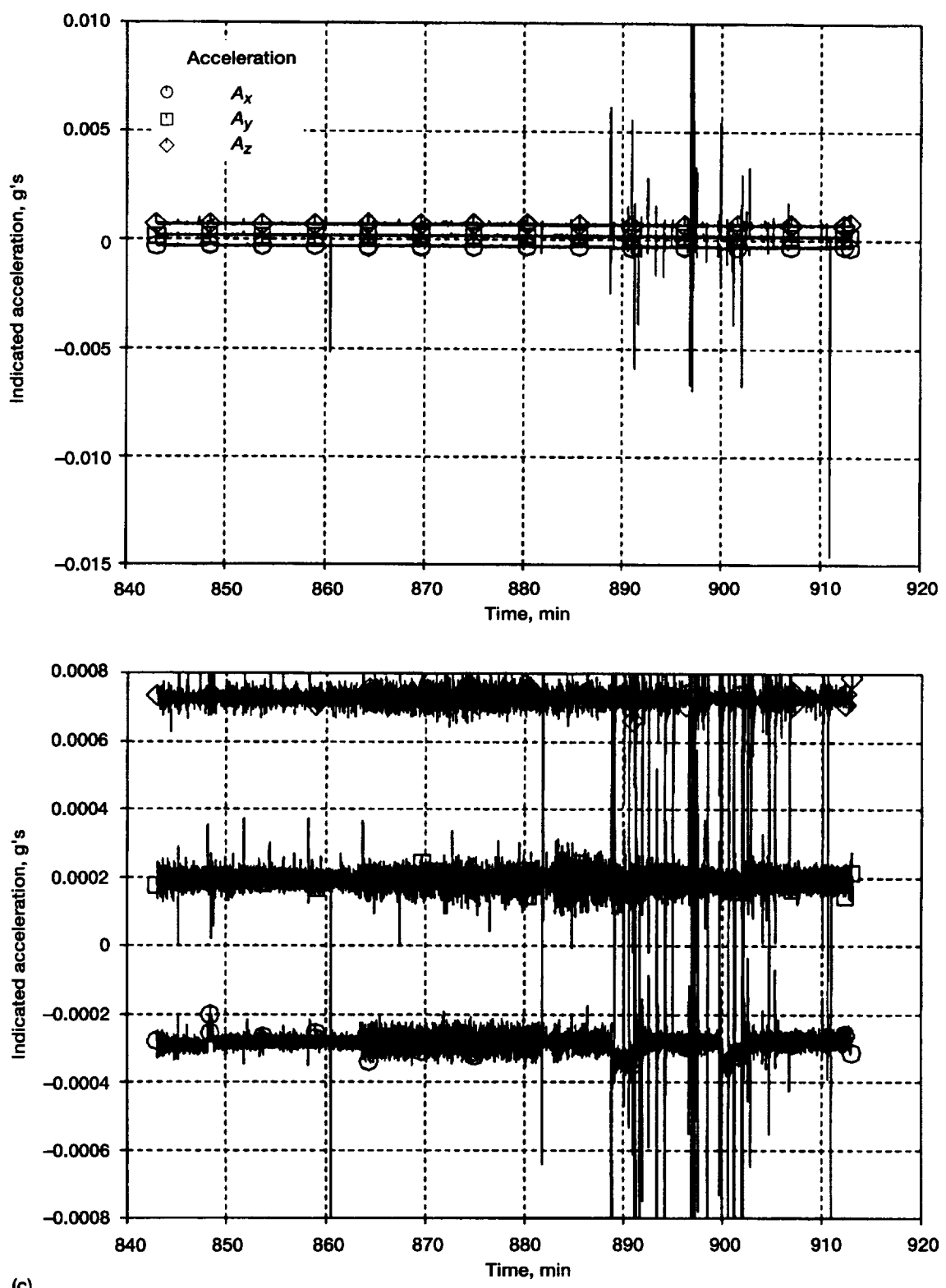


Figure A20.—Continued. (b) Fluid and heater temperatures.



(c)

Figure A20.—Concluded. (c) Accelerations. (Bottom graph shows expanded scale.)

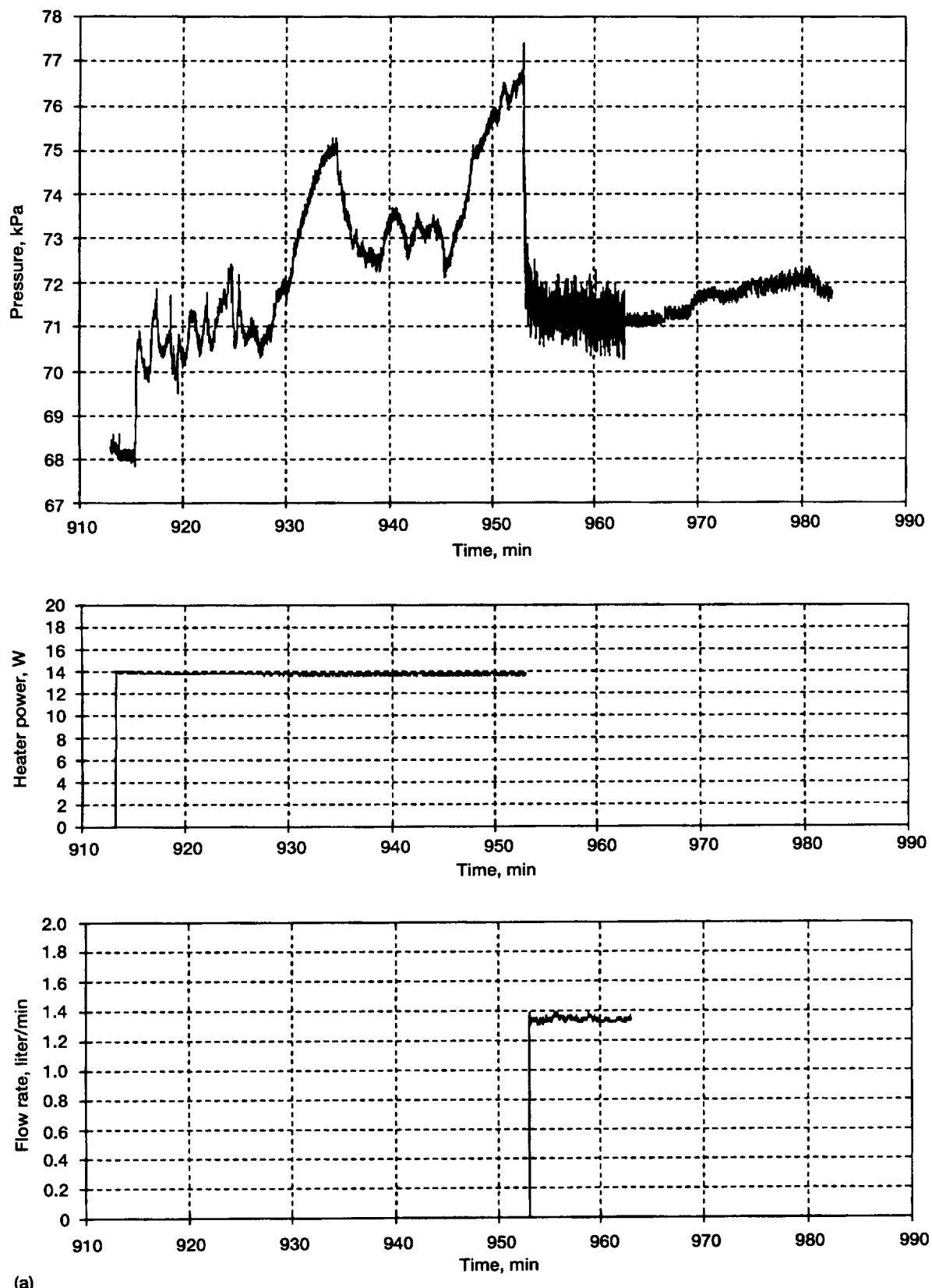


Figure A21.—Run 21. (a) Pressure, heater power, and flow rate. (b) Fluid and heater temperatures. (c) Accelerations.

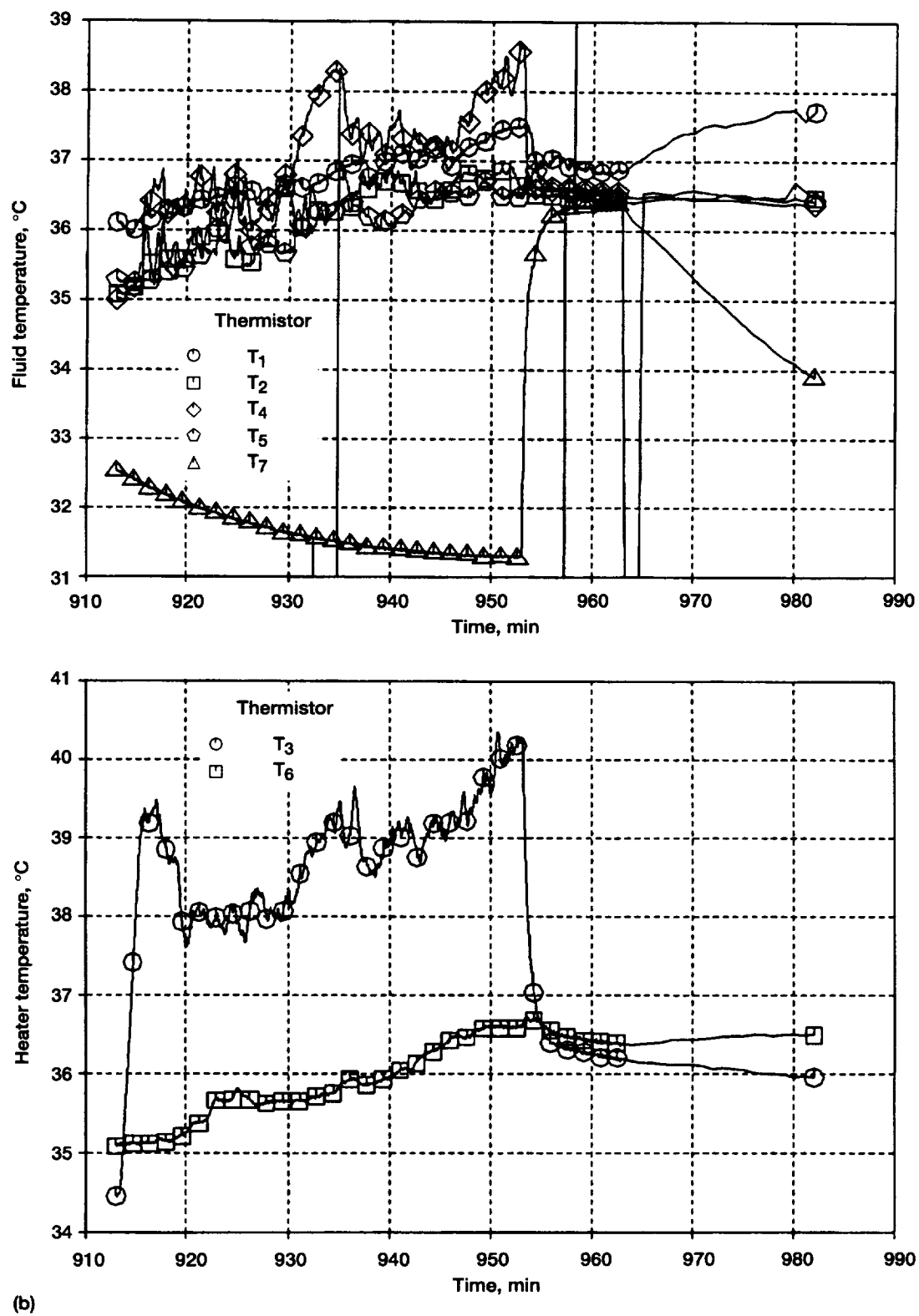
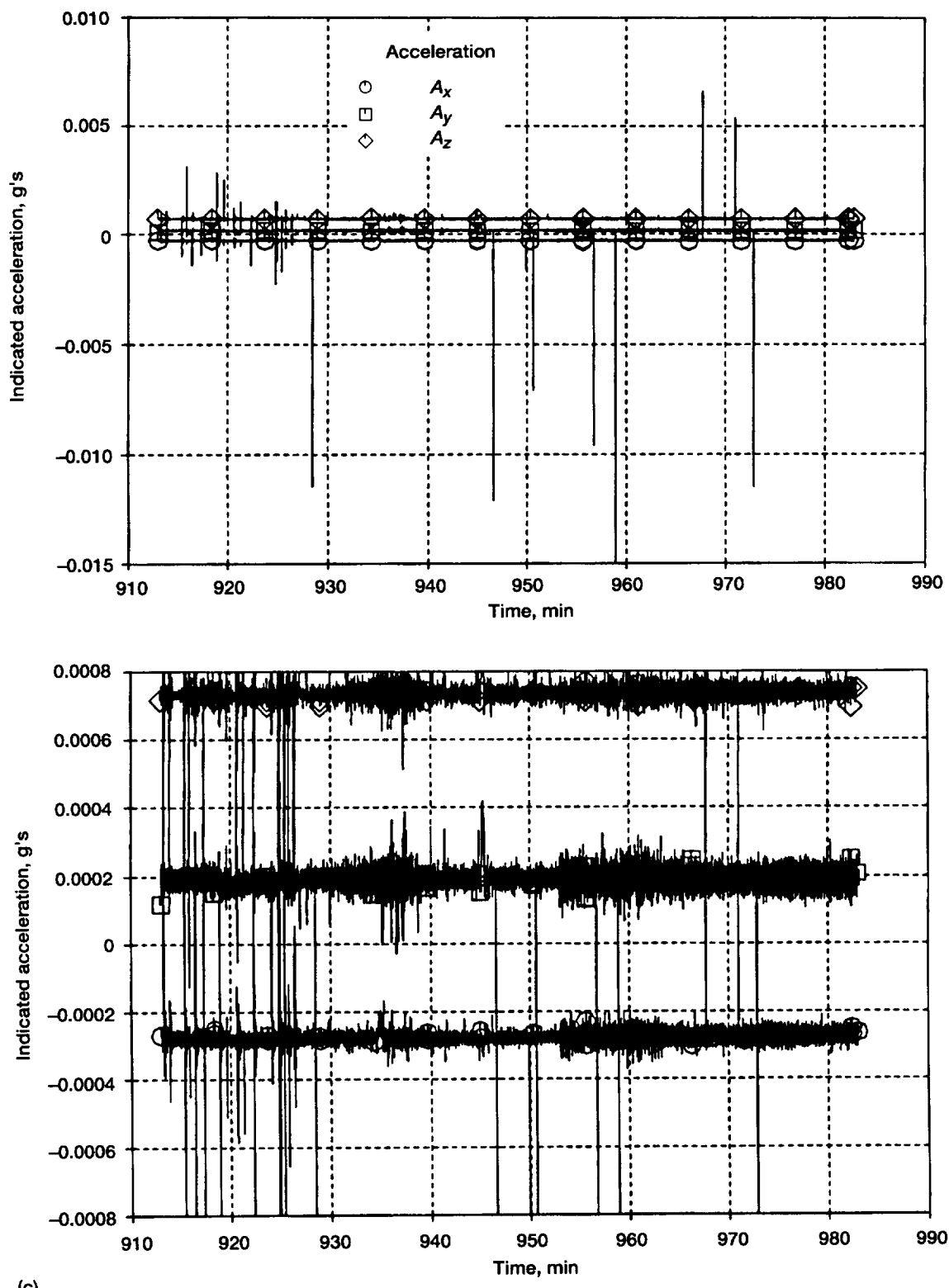


Figure A21.—Continued. (b) Fluid and heater temperatures.



(c)

Figure A21.—Concluded. (c) Accelerations. (Bottom graph shows expanded scale.)

References

1. Labus, T.L.; Aydelott, J.C.; and Amling, G.E.: Zero-Gravity Venting of Three Refrigerants. NASA TN D-7480, 1974.
2. Bullard, B.R.: Liquid Propellant Thermal Conditioning System Test Program. (LMSC-D159262, Lockheed Missiles and Space Co.; NASA Contract NAS3-12033.) NASA CR-72971, July 1972.
3. Aydelott, J.C.; Carney, M.J.; and Hochstein, J.I.: NASA Lewis Research Center Low-Gravity Fluid Management Technology Program. AIAA/GNOS Paper 85-002 (NASA TM-87145), Nov. 1985.
4. Poth, L.J.; and Van Hook, J.R.: Control of the Thermodynamic State of Space-Stored Cryogens by Jet Mixing. *J. Space Rock.*, vol. 9, no. 5, May 1972.
5. Aydelott, J.C.: Modeling of Space Vehicle Propellant Mixing—Cryogenic Propellants. NASA TP-2107, 1983.
6. Hochstein, J.I.; Ji, H.C.; and Aydelott, J.C.: Prediction of Self-Pressurization Rate of Cryogenic Propellant Tankage. *J. Propul. Power*, vol. 6, no. 1, 1990, pp. 11–17.
7. Meserole, J.S.; et al.: Mixing-Induced Ullage Condensation and Fluid Destratification. AIAA Paper 87-2018, 1987.
8. Brown, J.S.; Helmick, M.R.; and Sonin, A.A.: Vapor Condensation at a Turbulent Liquid Surface in Systems With Possible Spaced-Based Applications. AIAA Paper 89-2846, 1989.
9. Hasan, M.M.; and Lin, C.S.: Buoyancy Effects on the Vapor Condensation Rate on a Horizontal Liquid Surface. AIAA Paper 90-0353, 1990.
10. Lin, C.S.; and Hasan, M.M.: Vapor Condensation on Liquid Surface Due to Laminar Jet-Induced Mixing. *J. Thermophysics Heat Transfer*, vol. 5, 1991, pp. 607–612.
11. Lin, C.S.; and Hasan, M.M.: Self-Pressurization of a Spherical Liquid Hydrogen Storage Tank in a Microgravity Environment. AIAA Paper 92-0363 (NASA TM-105372), Jan. 1992.
12. Bentz, M.D.; Meserole, J.S.; and Knoll, R.H.: Jet Mixing in Low Gravity—Results of the Tank Pressure Control Space Experiment. AIAA Paper 92-3060, July 1992.
13. Bentz, M.D.: Tank Pressure Control in Low Gravity by Jet Mixing. (NASA Contract NAS3-25363.) NASA CR-191012, Mar. 1993.
14. Hasan, M.M.; et al.: Nucleate Pool Boiling in the Long Duration Low Gravity Environment of the Space Shuttle. AIAA Paper 93-0465 (NASA TM-105973), Jan. 1993.
15. Bentz, M.D.; et al.: Low-g Fluid Mixing—Further Results From the Tank Pressure Control Experiment: AIAA Paper 93-2423, June 1993.
16. Hasan, M.M.; et al.: Explosive Boiling at Very Low Heat Fluxes: A Microgravity Phenomenon. NASA TM-106325, 1993.
17. Siegel, R.; and Keshock, E.G.: Effects of Reduced Gravity on Nucleate Boiling Bubble Dynamics in Saturated Water. *A.I.Ch.E. Journal*, vol. 10, no. 4, July 1964, pp. 509–518. (On microfilm.)
18. Pavlov, P.A.; and Skripov, V.P.: Explosive Boiling of Liquids and Fluctuation Nucleus Formation. *Teplofiz. Vys. Temp.*, vol. 8, 1970, pp. 833–839.
19. Skripov, V.P.: *Metastable Liquids*, John Wiley & Sons, Inc., New York, 1974.
20. Ervin, J.S.; et al.: Transient Pool Boiling in Microgravity. *Int. J. Heat Mass Transfer*, vol. 35, 1992, pp. 659–674.
21. Ervin, J.S.; and Merte, H., Jr.: A Fundamental Study of Nucleate Pool Boiling Under Microgravity. (UM-MEAM-91-08, The University of Michigan, Ann Arbor; NASA Contract NAG3-663.) NASA CR-188732, 1991.
22. Lin, C.S.; Hasan, M.M.; and Nyland, T.W.: Mixing and Transient Interface Condensation of a Liquid Hydrogen Tank. AIAA Paper 93-1968, June 1993.

REPORT DOCUMENTATION PAGE

*Form Approved
OMB No. 0704-0188*

Public reporting burden for this collection of information is estimated to average 1 hour per response, including the time for reviewing instructions, searching existing data sources, gathering and maintaining the data needed, and completing and reviewing the collection of information. Send comments regarding this burden estimate or any other aspect of this collection of information, including suggestions for reducing this burden, to Washington Headquarters Services, Directorate for Information Operations and Reports, 1215 Jefferson Davis Highway, Suite 1204, Arlington, VA 22202-4302, and to the Office of Management and Budget, Paperwork Reduction Project (0704-0188), Washington, DC 20503.

1. AGENCY USE ONLY (Leave blank)			2. REPORT DATE March 1996		3. REPORT TYPE AND DATES COVERED Technical Paper	
4. TITLE AND SUBTITLE Tank Pressure Control Experiment: Thermal Phenomena in Microgravity			5. FUNDING NUMBERS WU-237-02-01			
6. AUTHOR(S) Mohammad M. Hasan, Chin S. Lin, Richard H. Knoll, and Michael D. Bentz						
7. PERFORMING ORGANIZATION NAME(S) AND ADDRESS(ES) National Aeronautics and Space Administration Lewis Research Center Cleveland, Ohio 44135-3191			8. PERFORMING ORGANIZATION REPORT NUMBER E-9724			
9. SPONSORING/MONITORING AGENCY NAME(S) AND ADDRESS(ES) National Aeronautics and Space Administration Washington, D.C. 20546-0001			10. SPONSORING/MONITORING AGENCY REPORT NUMBER NASA TP-3564			
11. SUPPLEMENTARY NOTES Mohammad M. Hasan and Richard H. Knoll, NASA Lewis Research Center; Chin S. Lin, Analex Corporation, 3001 Aerospace Parkway, Brook Park, Ohio 44142 (work funded by NASA Contract NAS3-25776); Michael D. Bentz, Boeing Defense & Space Group, Seattle, Washington. A 4-hour video tape supplement to this document is available from the NASA Center for Aerospace Information, (301) 621-0390. Responsible person, Mohammad M. Hasan, organization code 5340, (216) 977-7494.						
12a. DISTRIBUTION/AVAILABILITY STATEMENT Unclassified - Unlimited Subject Category 34			12b. DISTRIBUTION CODE			
This publication is available from the NASA Center for Aerospace Information, (301) 621-0390.						
13. ABSTRACT (Maximum 200 words) The report presents the results of the flight experiment Tank Pressure Control Experiment/Thermal Phenomena (TPCE/TP) performed in the microgravity environment of the space shuttle. TPCE/TP, flown on the Space Transportation System STS-52, was a second flight of the Tank Pressure Control Experiment (TPCE). The experiment used Freon 113 at near saturation conditions. The test tank was filled with liquid to about 83 percent by volume. The experiment consisted of 21 tests. Each test generally started with a heating phase to increase the tank pressure and to develop temperature stratification in the fluid, followed by a fluid mixing phase for the tank pressure reduction and fluid temperature equilibration. The heating phase provided pool boiling data from large (relative to bubble sizes) heating surfaces (0.1046 m by 0.0742 m) at low heat fluxes (0.23 to 1.16 kW/m ²). The system pressure and the bulk liquid subcooling varied from 39 to 78 kPa and 1 to 3 deg C, respectively. The boiling process during the entire heating period, as well as the jet-induced mixing process for the first 2 min of the mixing period, was also recorded on video. The unique features of the experimental results are the sustainability of high liquid superheats for long periods and the occurrence of explosive boiling at low heat fluxes (0.86 to 1.1 kW/m ²). For a heat flux of 0.97 kW/m ² , a wall superheat of 17.9 deg C was attained in 10 min of heating. This superheat was followed by an explosive boiling accompanied by a pressure spike of about 38 percent of the tank pressure at the inception of boiling. However, at this heat flux the vapor blanketing the heating surface could not be sustained. Steady nucleate boiling continued after the explosive boiling. The jet-induced fluid mixing results were obtained for jet Reynolds numbers of 1900 to 8000 and Weber numbers of 0.2 to 6.5. Analyses of data from the two flight experiments (TPCE and TPCE/TP) and their comparison with the results obtained in drop tower experiments suggest that as Bond number approaches zero the flow pattern produced by an axial jet and the mixing time can be predicted by the Weber number.						
14. SUBJECT TERMS Microgravity; Cryogenics; Propellant; Fluid mixing; Boiling; Evaporation						15. NUMBER OF PAGES 100
						16. PRICE CODE A05
17. SECURITY CLASSIFICATION OF REPORT Unclassified	18. SECURITY CLASSIFICATION OF THIS PAGE Unclassified	19. SECURITY CLASSIFICATION OF ABSTRACT Unclassified	20. LIMITATION OF ABSTRACT			

Videotape Supplement

The Tank Pressure Control Experiment/Thermal Phenomena (TPCE/TP) was performed in the microgravity environment of the space shuttle. The experiment consisted of 21 tests comprising a heating phase and a fluid mixing phase. The test tank was filled to about 83 percent by volume with liquid Freon 113. The unique features of the experimental results are the sustainability of high liquid superheats for long periods and the occurrence of explosive boiling at low heat fluxes.

A videocassette supplement to this document is available through the NASA Center for Aerospace Information. Much of the data returned by this experiment are best seen in this format as the still photographs reproduced in this report cannot convey the information that a motion picture can. The video supplement consists of two 2-hr tapes containing the complete data set. Each test run is identified in a preceding title slate by its run number, and a timer display is superimposed that corresponds with the time values in the digital data.

The videotape supplement is available for purchase from NASA by sending the request shown below to

NASA Center for Aerospace Information
Attn: User Services
P. O. Box 8757
Baltimore, MD 21240-0757

Date _____

Please send one (1/2-in. VHS, two 2-hour cassettes) copy of the video supplement to report NASA TP-3564 (E-9724-V).

Name of organization _____

Street number _____

City and State _____ Zip code _____

Attn: Mr./Mrs. _____

Title _____ Telephone (_____) _____

National Aeronautics and
Space Administration
Lewis Research Center
21000 Brookpark Rd.
Cleveland, OH 44135-3191

Official Business
Penalty for Private Use \$300

POSTMASTER: If Undeliverable — Do Not Return